Design and fabrication of an aerosol collector for infrared spectroscopy analysis

Nikunj DUDANI

What I cannot create, I do not understand.

— Richard Feynman

To my parents, Babita and Ram Dudani…

Acknowledgements

Abstract

Particulate matter (PM) pollution causes adverse health effects and millions of deaths each year. PM or aerosol, is difficult to characterize because of its wide range of particle sizes, constituents (various organic and inorganic compounds), concentration, morphology, state (liquid or solid), and time-dependent modification. Infrared (IR) spectroscopy is a non-destructive method which provides useful chemical information about the constituents of PM. Current methods for collecting samples use filters made of materials which interfere with the IR spectra and thus have lower detection capabilities. In order to improve the chemical resolution, collection on an IR-transparent substrate is desirable. However, as most current collector types modify or preferentially sample certain size ranges, chemical composition, morphology or state, a new collector design is required. Electrostatic precipitation (ESP), impaction and filtration are common methods for aerosol collection. Impactors preferentially sample certain size range and liquids and suffer from particle bounce-off effects. Filtration onto filters uses a high pressure-drop that can modify the aerosol chemical composition and has inherent size-dependence. ESP is a versatile method of aerosol collection and does not suffer from high pressure-drop, or from bounce-off effects and is highly tunable, allowing its use in various applications. However, most ESP designs in the public domain have been designed for different purposes and face limitations in direct application in quantitative chemical composition measurement using IR spectroscopy. In order to rapidly develop prototypes and test the feasibility of such a device we used numerical simulations along with 3D-printing. A device was fabricated and tested for mass loading response and surface deposition profile with image analysis and variable aperture IR-spectroscopy. After observing near-quantitative response of the collector, we developed an analytical model to evaluate the particle collection response over a wider range of geometries and operating variables, with a goal to achieve specific objectives with the collector. Low size dependence, low chemical interference, and high collection efficiency are required to obtain an aerosol sample identical to the aerosol in air. High spatial uniformity in the deposition pattern is important for reducing the optical artefacts or the spectrometer dependence, and a high collection mass flux reduces the sample collection time needed for making a confident claim. The analytical model embodies the physics of particle migration trajectories due to fluid dynamics and electrostatics in a two-stage ESP device. We evaluated it against numerical simulations, which can only be run for a limited number of configurations. The scalable model allowed translating the objectives into quantifiable variables and to relate the ESP design to the collection performance, and evaluate the trade-offs to arrive at a design that is optimized across multiple length scales.

Abstract

The proposed collector should provide high chemical- and time-resolution information of PM in laboratory or ambient sampling settings. It has applications in laboratory studies into volatile and labile aerosol species that have low life-time, some of which are linked to harmful oxidative-stress in the human body.

Keywords: Design, fabrication, collector, quantitative, IR, FT-IR, ESP.

Résumé

Les particules suspendues dans l'air (aérosol) sont parmi les causes principales de nombreuses maladies et sont responsable de millions de décès chaque année. La caractérisation détaillée de cette classe de particules est extrêmement compliquée due à different aspects, comme leur taille, leur composition chimique (organique, inorganique), ainsi que leur concentration, l'état de phase, la morphologie, et les variations dépendantes au temps. Une des méthodes prometteuse dans le domaine est la spectroscopie infra rouge (IR) qui est une méthode non destructive et utile pour étudier la composition chimique des particules. Les méthodes actuelles sont basées sur l'échantillonnage des aérosols mais sur des filtres qui sont souvent non-transparent à l'IR et ainsi diminuent la capacité de détection de l'instrument. Afin d'augmenter la résolution chimique et supprimer l'interférence, l'échantillonnage sur un matériel transparent à l'IR est désirable. Cependant, parce que la majorité des collecteurs actuel modifient la distribution de taille, la composition chimique, la morphologie, et l'état de phase des aérosols, une nouvelle conception de collecteur est nécessaire. La précipitation électrostatique (ESP), l'impaction, et la filtration sont des méthodes communes pour collecter des aérosols. L'impaction est applicable dans certaine distribution de taille, spécialement pour des particules liquides et subis par l'effets bounce-off. La filtration utilise une chute de pression suffisamment large pour provoquer d'éventuelles altérations de la composition chimique de l'échantillon. ESP ne comporte aucun de ces inconvénients et émerge comme une des solution versatile et très utilisée. Pourtant, les modèles commerciaux actuellement disponible sont conçus pour des objectifs différents, donc ils sont limités pour les applications quantitative de spectroscopie IR. Afin de développer rapidement les prototypes et tester leur faisabilité nous avons utilisé la modélisation numérique et l'impression en 3D. Un collecteur a été fabriqué et testé pour la réponse de charge de masse et le profil de dépôt de surface avec analyse d'image et spectroscopie IR à ouverture variable. Après avoir observé la réponse quasi quantitative du collecteur, nous avons développé un modèle analytique pour capturer la réponse de la collection de particules sur une gamme beaucoup plus large de géométries et de variables. Il s'agit d'un modèle mathématique sans dimension qui explique la physique des trajectoires de migration des particules dues à la dynamique des fluides et à l'électrostatique dans un dispositif ESP à deux étages. Notre modèle mathématique était comparé à des simulations numériques bien établies, pourtant limite en nombre de configurations due à leur considérable coût lié aux calculs. Le modèle nous a permis de tester différents designs et optimiser tous les paramètres à l'échelle de longueurs variables afin d'identifier celle qui offre le meilleur compromis entre l'ensemble des objectifs de conception. Le collecteur final fournit

des résultats hautes résolutions dans les dimensions chimiques ainsi que temporelles. Il est utilisable non seulement dans le laboratoire mais également à l'extérieur, qui le rende comme une méthode idéale pour les études de terrain. Il peut être utilisé dans des études qui visent la caractérisation des espèces chimiques réactives ou doté d'une durée de vie relativement courte, souvent liée au stress oxydatif connu nocif pour la santé humaine.

Contents

Contents

List of Figures

List of Tables

Chapters Part I

1 Introduction

1.1 Atmospheric Aerosol

Aerosol is defined as a dispersion of a solid, a liquid or both in air (Miloslav N. and K., 2014). Atmospheric aerosol can be classified as primary (when directly emitted as particles) or secondary (when formed by transformation of generally low volatile precursor gases to particles). Atmospheric aerosol can originate from natural or anthropogenic sources. It is mainly the anthropogenic fraction that has been associated with adverse health effects. Furthermore, atmospheric aerosol influences the climate by acting as cloud condensation nuclei (CCN) and the Earth's radiation balance (Hobbs, 1993). Aerosol's physical and chemical transformation results in the formation of particles with different size, composition and structure. For example, those through chemical reaction, coagulation and phase transition (Monks et al., 2009). Atmospheric aerosol is commonly used in reference to the dispersed phase, called particulate matter (PM). PM has been identified to increase the risk of mortality and acute morbidity and with decline in respiratory and cardiovascular health (Pandis et al., 2013). PM air pollution causes around 4.1 million premature deaths per year around the world, according to the World Health Organization (WHO) (Organization, 2016), and it has been linked to numerous adverse health effects, heart and lung disease. PM is hard to characterize because it is a complex mixture of many different chemical constituents that have different sizes, state and morphology. The particles can vary in size from few nanometers to few tens of micrometers, 10^2 - 10^5 cm^{-3} and over several orders-of-magnitude of concentrations 1-100 μg m^{-3} (Monks et al., 2009). The composition, sources and residence times of aerosol is size-dependent (Pérez et al., 2010). Associated with high health risks, PM less than 10 and 2.5 micrometers (PM$_{10}$ and PM$_{2.5}$, respectively), is monitored and regulated (limited by mass concentration) in most developed countries. Monitoring atmospheric aerosol at various locations and a detailed chemical analysis on them can help identify the sources and thus form meaningful regulations and control strategies. Atmospheric aerosol have both organic and inorganic fractions.The organic fraction has a high level of heterogeneity and uncertainty limits understanding its mechanism overall effects.

1.2 Aerosol chemical characterization methods

Aerosol can be characterized using numerous analytical methods, each varying in the mass concentration and chemical specificity it can quantify (Hallquist et al., 2009). The analyzing methods can be classified as on-line or offline. Some techniques help characterize number, composition, or morphology and can focus on a specific fraction of particles (like cluster chemical ionization mass spectrometry, cluster-CMS), or single particle (aerosol time-of flight mass spectrometry, ATOFMS).

For analyzing the offline collected samples, the usual first step is mostly liquid extraction of the sample from the filter substrate that is then used for further analysis. Many systems are available that help in extraction assisted by application of high temperature, pressure, microwave, or sonication (Parshintsev and Hyötyläinen, 2015). Solvent extraction, however, has been found to contribute for the highest uncertainty in quantifying the aerosol species, especially high molecular weight unsaturated alcohols and acids (Jiménez, Pastor, and S. G. Alonso, 2010). Moreover, there is generally a concentrating step involved after extraction, that may lead to further uncertainties. Thermal desorption (TD) is another commonly used method which can work with lesser sample mass and with higher sensitivity when connected to Gas Chromatograph (GC)-Mass Spectrometer(MS). However, the high temperatures used can lead to degradation of certain reactive species and the system generally underestimates PAHs with five or more rings. Liquid chromatography (LC) is also commonly used in tandem with an MS after a TD. LC systems, particularly useful for water-soluble organics, are generally better at analysing the high molecular weight compounds that are difficult to analyze with a GC.Numerous other devices are used to provide complementary information. High resolution mass spectrometry (HRMS) with MS, for example, provides information on the structural identification. Time-of-flight MS (TOFMS) and hybrid quadrupole-time-of-flight (QTOFMS) are some of the HRMS devices commonly used. Other methods such as Capillary Electrophoresis (CE) are good at analyzing highly oxidized and polar organic compounds. The method of characterization can be either non-destructive (for example optical methods or gravimetric analysis) or destructive (requiring extraction, desorption, or other modifications). Each method focuses on a specific set of species that it can analyze and can targets either multi-particles or single particle analysis. Some devices when connected to size segregated sampler can result in size resoled analysis, while some act on a larger size range. Optical and electron beams also provide information down to single particles and using Scanning Electron Microscopy - Energy dispersive X-ray spectroscopy (SEM-EDX) can provide highly resolved structural, morphological and composition information. Some of the commonly used online measurement devices are Aerosol mass spectrometer (AMS), Aerosol chemical speciation monitor (ACSM), or the TD-GC/MS method. Table 1.1 summarizes some of the analysis methods classified according to the species it analyses, mode of operation(continuous or non-continuous) and the method of analysis(destructive or non-destructive). Other methods of analysis include light microscopy, electron beam methods (related to Scanning Electron Microscopy or Transmission Microscopy), laser microprobe mass spectrometry, Ion mass

spectrometry, Raman microprobe or infrared microprobe (Fletcher et al., 2011). In general, a rapid, sensitive and multi-element (or multi-component for organics) method is desirable (Adams, 1994).

1.2.1 IR analysis

Infrared (IR) spectroscopy has been used for studies of gases and PM in the atmosphere and is extensively used in other fields of food industry and quality control. Fourier Transform -IR (FT-IR) has been used to measure the presence of ammonium, water, ice, mineral dust and organics in laboratory and ambient samples (Takahama, Ruggeri, and Dillner, 2016). For analyzing PM, FT-IR has the advantage of being non-destructive and measuring unique chemical information in terms of reactive units (Function Groups- FGs) in the chemical molecules (Dron et al., 2010) (Ranney and Ziemann, 2016). The chemical composition is otherwise obtained through extraction of collected samples on filters, which as previously discussed use many strong chemicals or high temperature and can induce the maximum uncertainty while solution preparation. It must be noted that the spectra obtained for ambient samples differs from isolated molecules in that the peaks are broadened due to many similar bonds vibrating in minutely differing environments and considerable band overlaps due to the hundreds of molecules present (Kelley, 2012). This presents a challenge as the resulting rich and complex spectrum is hard to interpret. Recently, substantial advancement has been made the analysis and the functional groups have been used to reconstruct the PM mass and OM measurements, with lower uncertainty than current carbon monitoring methods (Russell, 2003). Moreover, the data when properly characterized for the functional groups, helps identify the emission sources (Russell, Bahadur, and Ziemann, 2011; Takahama, Schwartz, et al., 2011). Furthermore, some functional groups are identified as precursors of oxidative stress and is thus of importance to health(A. M. Arangio et al., 2016). A major step towards overcoming the limitation of analyzing the spectra has been through the development of new algorithms that can analyze the spectrum and predict the PM composition with high accuracy (tested on a large collection of data in United Stated ambient air quality monitoring networks)(Takahama and Dillner, 2015). Furthermore, new methods are able to quantify other important chemicals of PM (like, organic and elemental carbon) through calibration models (Dillner and Takahama, 2015b; Dillner and Takahama, 2015a). (Takahama, Ruggeri, and Dillner, 2016) used sophisticated statistical methods that selective remove the Teflon signal from the obtained IR spectra, thus enabling as a next step, quantitative analysis of the chemical spectra from the atmospheric sample only. This enables performing IR analysis on the samples collected on Teflon filters for gravimetric analysis.

The infrared spectra of collected aerosol can be acquired using different configurations as summarized below.

1. Transmission: The infrared radiation transmitted through the sample is measured; the aerosol sample will decrement the original radiation intensity due to absorption and

Table 1.1: Various characterization methods for analyzing different special in atmospheric aerosol (Table adapted from (Agency et al., 2011))

24emSpecies Analysed	Method	
	With pre analysis step (destructive)	Direct (non-destructive)
54emAnions and cation species	Ion chromatography - With extraction	XRF
	Ion-selective electrode - with extraction	FTIR
	Colorimetry - With extraction	
	IC-based methods (PILS-IC, MARGA, GP-IC, AIM) (SCM) - Growth by condensation	
	Thermal Reduction with Detection by Gas Analyzers (SCM) - Heated over catalyst	
44emParticulate Carbon: OC, EC, CC, TC, BC, WSOC	Thermal optical reflectance (TOR) - Baking off from filters	Sunset Laboratory continuous carbon analyzer (SCM)
	Ion-selective electrode - with extraction	FTIR
	TOT - Baking off from filters	Aethalometer (SCM)
	TPV - Baking off from filters	PAS (SCM)
		MAAP (SCM)
24emOrganic Aerosol Speciations	GC-MS - Baked off filters	
	HPLC coupled to detector systems (e.g., mass spectrometer, UV, fluorescence) - With extraction	FT-IR
34emElements—Nondestructive		XRF
		PIXE; PESA
		INAA-Filter folding
44emElements-Destructive	ICP-MS - With extraction	
	TV-AAS - With extraction	
	ICP-AES - With extraction	
	EAS - Collected by steam condensation	
44emParticle Bound Water(PBW)		DAASS (SCM)

*SCM - semi continuous measurement

scattering out of the beam. The scattering contributions are corrected through spectral preprocessing techniques.

2. Internal reflection: The infrared radiation is measured after (possibly multiple) reflections from a surface; the aerosol sample which lies on the opposing side of the reflecting surface will absorb radiation intensity of the generated standing wave. The standing wave decays with a length scale on the same order as typical atmospheric aerosol, leading to infrared spectra that is dependent on particle-size. Attenuated total reflection (ATR) is a commonly used method.

3. External reflection: The infrared radiation is measured after reflection from surface; the aerosol sample will decrement the original radiation intensity due to absorption and scattering. The scattering component includes both specular and diffuse contributions (diffuse reflectance, DRIFTS), and resulting spectrum will depend on both. This technique is generally difficult to use for quantitative analysis of particles.

Transmission mode IR is established and the mode of operation is straightforward with the transmitting beam carrying the chemical bond information. ATR-FT-IR another commonly used method. (Shaka' and Saliba, 2004) used a commercially available ATR-FTIR crystal and analyzed aerosol samples on Teflon filters by pressing them against the ATR crystal and obtained qualitative data of organic and inorganic species. Later, ATR-FTIR was used to analyze demonstrate that the spectra could be used to derive quantitative information (Ghauch et al., 2006). Other methods of ATR analysis have been through spiking the crystal with an extracted solution (Coury and Dillner, 2008), direct collection (Ofner, Krüger, et al., 2009) or electrospray deposition (A. Arangio et al., 2019). However, because of the exponentially decaying evanescent wave the ATR (Figure 1.1)system has inherent size dependence for poly-dispersed particles. While reflection techniques can be useful for detection or identification of substances in aerosol form (by examining spectral absorption peaks), capability for quantitative analysis of atmospheric aerosol particles across a large number of samples has only been demonstrated using the transmission method. The transmission method also permits direct comparisons to spectra collected in current monitoring networks.

Currently IR analysis is done by using samples collected on Teflon filters mostly. The interference of Teflon absorbance peak in the IR spectra limits its detection capabilities. In order to remove the interference and improve the quantitative chemical composition measurements with IR spectroscopy, collection on an IR-transparent material is desirable. Many groups have previously worked on making an offline PM analysis with FTIR (W.J.O.-T., 1969; Cunningham, n.d.; Ofner, Krüger, et al., 2009). Different methods have been employed for obtaining the FTIR spectra. One of the first such method was using polished Zinc selenide (ZnSe) crystals (that are transparent to IR) as some impaction stages in a Low Pressure impactor. The crystals were then analysed in transmission FTIR to obtain size-segregated chemical information of atmospheric aerosol (D. T. Allen et al., 1994; Blando et al., 1998). Another method was to extract the sample from a quartz fiber filter and analyze the sample by spiking the extract on

$$d_p = \frac{\lambda}{2\pi n_2} \left[\sin^2 \theta - (n_1/n_2)^2 \right]^{-1/2}$$

$d_p \rightarrow$ *penetration depth*
$\theta \rightarrow$ *Angle of incidence*
$\lambda \rightarrow$ *wavelength*
$n_1, n_2 \rightarrow$ *refractive index of substrate and sample respectively*
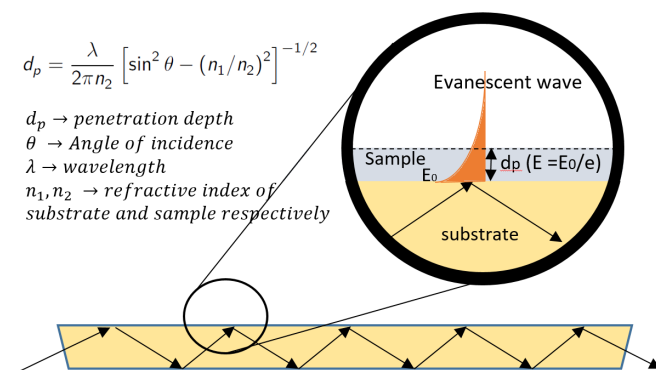
Figure 1.1: ATR evanescent wave.

a ZnSe crystal and obtaining the FTIR spectra of the solution and and the solvent separately which were then subtracted to obtain the representative spectra of the aerosol (Polidori et al., 2008). This method, however, is not free from the uncertainty of the extraction step. There have been many experiments to scan the aerosol while still on the Teflon filters, and subtract the blank Teflon spectra in order to obtain a relatively representative atmospheric sample's chemical spectra (Maria et al., 2002). As Teflon absorbs in some of the IR region, removing the interference accurately is then important for quantitative analysis and is predicated on collecting aerosol on an IR-transparent substrate.

1.3 Aerosol sampling methods

Some methods are online (or in-situ) but most methods operate offline where sampling and analysis is done separately. Filtration, impaction and electrostatic precipitation are some of the commonly used sampling method. Thermophoresis is applicable to very small particles and is hence not considered for the application here. Table (1.2) summarizes the collection methods.

From the various sampling methods, the most commonly used is filters, which are then transported for subsequent analysis, with or without sample pre-treatment. It can be noted that depending on the sampling method, the analytical method and the aerosol concentrations, samples collection can last for hours to days (Parshintsev and Hyötyläinen, 2015). Quartz fiber filters offers the advantage of high thermal chemical stability, useful during sample preparation which sometimes achieves extraction of the sample with strong chemicals. However, the filter can absorb organic gases, which may lead to positive artifacts, and with high flow rate sampling the negative artifacts induced by volatilization also effect the sample. Teflon, on the other hand, shows negligible positive artifacts but needs to be kept clean before sampling, to minimize contributions from organic impurities. Sampling artifacts can affect the final measurement. For example, around 16% of the $PM_{2.5}$ mass was reported to be lost during the sampling time (Anderson et al., 2002) and some semi volatile organic compounds (SVOCs),

which form a sizable portion of Organic Mass (OM), volatalized during the sampling time (Modey, 2001). Artifacts due to chemical reaction (oxidation, water uptake) needs to be kept in mind while setting up the sampling system, such that the effects can be minimized.

Impactors have been previously used previously (D. T. Allen et al., 1994) to collect on ZnSe (Ir transparent) crystals, but it has been established that not all particles adhere to the substrate and many bounce off (V. A. Marple, 2004). This is undesirable. Various impactors are designed to collect size-resolved samples, sometimes, with thin film of foam/ adhesive that prevent bouncing of particles at the high collection flow rates. However, with dependence on the state of aerosol collected and inherent size-segregation, use of impaction is limited for the current application.

Electrostatic precipitation has also been used as a sampling method and allows for choosing a size range according to electrical mobility. Moreover, modifying electrostatic field for controlling the particle trajectory (against the drag and viscous forces), though not trivial, is possible. It, however, needs further analysis as the corona used in commonly used corona type chargers, can lead to formation of ozone (Awad and Castle, 1975) which can possibly react with the incoming particles. There are many ways to reduce (or prevent) the generated ozone, with the possibility of using chargers that do not generate ozone (Section 1.4.1). Hence, ESP is a versatile tool that can be used to design a collector for collecting particles on an IR transparent substrate.

Table 1.2: Sampling method analysis for the portable on-line FTIR ambient aerosol analyzer.

Method	Filtration	Impaction	Electrostatic Precipitation
Substrate	Membranes	Solid surface	conductors
Principle of Operation	Brownian and other diffusion	Particle momentum, strong adherence force	Electrostatics.
Challenges	Replacing the membrane, Material interference	Composition dependant bounce off, size induced variation	Charging (possible ozone generation), effect is size and flow dependant

1.4 Electrostatic precipitation (ESP) devices

ESPs for particle deposition commonly operate in two-stages (particle charging and particle collection) for higher control on deposition, and generally fall into two broad categories, a translationally symmetric design (linear system) or a radially symmetric design (radial system). In both systems the electric field is perpendicular to the fluid flow that is parallel to the collection surface. Additionally, in most radial design the fluid enters the collection region through a tube perpendicular to the collection surface, before moving radially outwards. A

parallel plate linear ESP was proposed in 1974 for collecting aerosol particles on a substrate for subsequent analysis with IR spectroscopy (Harrick and Beckmann, 1974), and a point-to-plate linear ESP for similar application has been fabricated in 2009 (Ofner, Krüger, et al., 2009). (Ofner, Krüger, et al., 2009; Ofner, Kruger, et al., 2011) have demonstrated a few ESP devices that are used for aerosol sample collection and for ATR FTIR analysis thereof. Their analysis also highlights the use of Zinc Selenide (ZnSe) as a favorable substrate. An offline radial ESP for TXRF goes back to 1991 (Dixkens and Fissan, 1991) and was characterized further in 1999 (Dixkens and Fissan, 1999). Other radial ESPs have been used for TEM analysis (Fierz, 2007) and for functional film formation (Kala et al., 2012). Hence, many independent ESP collection devices have been developed. However, with preliminary analysis the design either use very high electric field strength that can cause chemical modification of the aerosol, or have high size-segregation in deposition. Hence, we proceed to design a collector for the said objective. As many particle charger design are available, and a two-stage ESP will provide higher tunability in deposition, we further explore the charger designs to use with the planned collector design.

1.4.1   Charging devices

A charger is chosen to be used with the ESP collector. In this work, the application is to charge incoming ambient aerosol particles controllably and uniformly on a substrate. Based on this we can say that a charger will be desirable if it can charge particles independent of particle size, aerosol concentration and aerosol particle material. Moreover, the operation should be steady, should not chemically modify the sample particles, or alter the sample population in any manner. Lastly, the charger should not hinder (or incapacitate) the ability of the device to have a high time resolution.

In order to compare and analyze the charger that is suitable for the current application, it might be useful to consider the most common or most relevant factors and compare the various design types discussed in the Section A. Some important factors to be considered for a charger were mentioned by (Domat, Kruis, and Fernandez-Diaz, 2014).

Some factors that are considered for charger selection in the current application are discussed here:

1. Ozone production: With enough energy (provided by the corona discharge), the molecular oxygen present in air sampled with the aerosol particles, can sometimes split and recombine to form ozone, a strong oxidizer that is unstable and toxic. This can modify the existing particles, form some nitrates with the molecular nitrogen and deposit as particles, or result in degradation of the charger components. This can be avoided by using a neutral gas free of oxygen, but this is not feasible while sampling the atmospheric aerosol directly. Negative corona discharge has a higher production of ozone as the oxygen radicals can be formed easily with the presence of large amounts of electrons

migrating in the charger. Thus, positive corona discharge is preferred as it has lower ozone production, however, does not completely eliminate it. Moreover ,as discussed, using different materials (carbon fiber) for the corona discharge were shown to reduce the ozone production, which can prove to be a possible option in case long term stability (low electrode wear) of such chargers are demonstrated. Ozone production is very low for the UV type chargers, however, it presents its own challenges in charging dependence on the aerosol particle material. In the selection process, ozone production minimization is a major factor, as the project will employ the use of the final device in study of reactive oxygen species and modification of aerosol particles at the charger is not desired. Hence, the design of (T. T. Han, Thomas, and Mainelis, 2017) A.8 is suitable as it has demonstrated lower ozone production.

2. Nanoparticle generation: This is a important factor to consider while evaluating the use of corona chargers. The wear of electrode material, not only changes the performance characteristics of the charger but also produces new particles, either through sputtering or errosion of the electrode or from gaseous contaminants (with presence of moisture) (M. Alonso, M. Martin, and Alguacil, 2006). This also results in lowering the life span of a corona and wears the chaeger in time. Using platinum (Medved et al., 2000) , tungsten or other high melting point and low oxidizing metals is a good option to minimize this undesirable effect in particle charging. For this application, tungsten is chosen as a starting material for the corona electrode, to minimize particle generation.

3. Presence of additional AC field: One feature of all Hewitt type chargers is that it uses an additional AC field to facilitate the transfer of ions to the charging zone. When comparing this to other DC type chargers where no such field was applied, Marquard et al. concluded that the AC field does not reduce the loss of the particles (Marquard, Meyer, and Kasper, 2006) rather a design with higher ions transmission (penetration) had higher intrinsic efficiency but the electrostatic losses were not lower. For the current application the design is being 3D printed for rapid prototyping and hence, a simple design is preferred and most Hewitt type chargers have relatively more components and setup parameters (AC field, precise sheath flows). The higher intrinsic efficiency might be useful for using with a collector right after the charger but the spatial distribution (with annular sheath) might be another hindrance to uniformity objective on the final device.

4. Particle losses: Comparing particle losses for all the types of charger is difficult as the values reported are for different sizes and in different percentage (intrinsic or extrinsic or penetration). Furthermore, with different flow rates upstream and downstream (with sheath), it can be discussed if using particle concentration or particle flux is a better basis for comparison. Furthermore, every design is characterized with different flow setups and parts and hence, a strict comparison is difficult. Marqard et al. in 2006 did try and compare five published charger studies for comparing performance in 10-30 nm size region and came up with some factors for comparison and highlights the careful

nature for comparison. Ideally, lowest particle loss (highest penetration) should be preferred, however, as the application used the charged fraction of the transmitted particles, extrinsic (or intrinsic) efficiency is a better parameter for consideration here. Moreover, overcoming diffusion losses for the sub 20-30 nm particles is not of highest importance as the final device can accordingly be labelled to the size range that it can detect. However, percentage of total particle loss is a higher concern as this will directly affect the sampling time necessary adversely, and hence the time resolution. A systematic loss (as a function of particle size) is also not desirable as this modifies the sample to a different size distribution. Taking the above factors into consideration, it is decided that losses (especially in >80 nm region) are not very different in most chargers and hence, is not considered a deciding factor for initial selection, however, may later be considered and the device modified accordingly.

This explorations helps in identifying an initial charger design based on simplicity, low sample modification (through ozone or new particle generation), demonstrated operation and not very high particle loss. The wire-to-wire charger (T. T. Han, Thomas, and Mainelis, 2017) is a good starting point mainly because of its low ozone production and simplicity. The indirect corona charger with two sonic-ject ionizers developed by (Qi, D. R. Chen, and Pui, 2007) is another promising setup, mainly due to its low losses and flow rate independence, which can hopefully allow for low residence time and hence lower ozone production. Finally, indirect UV charging (Grob, Burtscher, and Niessner, 2013; Shimada et al., 1999) is also a promising method for particle charging owing to its minimum ozone production and low losses. It must be understood that the choice of the charger serves as a satisfactory starting point thus allowing building the device around, while encapsulating the charger as a charge particle provider that is potentially replaceable. Hence, a charger design that can realize such factors to a considerable extent can be potentially used to replace the current charger in the device, in order to obtain better operating range and efficiency.

2 Design and fabrication of an electrostatic precipitator for Infrared spectroscopy

Manuscript in preparation

Authors: DUDANI Nikunj and TAKAHAMA Satoshi

2.1   Abstract

Infrared (IR) spectroscopy is useful in measuring unique chemical information of aerosol in terms of functional groups. It is a non-invasive method that has been used to calculate important ratios and concentrations that are relevant for ambient monitoring. At the same time it can used for source apportionment and can provide unique information about peroxide concentrations, which have been linked to oxidative stress and higher health impacts. Currently, most of the IR analysis is performed on Teflon filters on which the particles are collected. Teflon interferes with the IR spectra and imposes a strong absorption band that not only makes extracting the chemical information of aerosol harder but also limits the lower extent of detection. An alternative IR measurement method that does not inherit such limitations aerosol would be to collect the particles on an IR transparent material. We present an electrostatic precipitator design that enables such measurements by collection on a Zinc Selenide (ZnSe) disc. Through numerical simulations and rapid prototyping with 3D-printing, we design and fabricate a device which is tested with poly-dispersed ammonium sulfate particles to evaluate the quantitative chemical composition estimates against particle count reference. Furthermore, with an image analysis procedure and using variable aperture on the IR spectrometer, we analyze the surface mass distribution. The device has high collection efficiency and fairly linear response to mass loading, all with a semi-uniform deposition. The method of design and fabrication is transferable to other design applications and the ESP collector can further be used to identify other design variables that can improve its performance.

Keywords: Design, fabrication, collector, quantitative, IR, FT-IR, ESP.

2.2   Introduction

Infrared (IR) spectroscopy is a non-destructive and is useful in measuring unique chemical information in terms of reactive units (Function Groups- FGs) in the chemical molecules (Dron et al., 2010) (Ranney and Ziemann, 2016). The chemical composition is otherwise obtained through liquid extraction of collected samples on filters, which uses many strong chemicals or high temperature and can modify the sample. IR spectra of atmospheric samples is very complex as it has vast range of sizes and composition. New algorithms allows the analysis and predict the PM composition with high accuracy (tested on a large collection of data in United Stated ambient air quality monitoring networks)(Takahama and Dillner, 2015). Furthermore, some methods are able to quantify other important chemicals of PM (like, organic and elemental carbon) through calibration models (Dillner and Takahama, 2015b; Dillner and Takahama, 2015a).

One of the main challenges in IR spectroscopy is that the filter material, Teflon has a large prominent absorption near 1200 cm^{-1} region, which overlaps with some other important functional groups. (Takahama, Ruggeri, and Dillner, 2016) used sophisticated statistical methods that selective remove the Teflon signal from the obtained IR spectra but as the scale

of the Teflon absorbance is orders of magnitude higher than the collected samples, this limits the detection capabilities of the spectra.

In order to overcome the challenge, we develop a new collector that collects particles directly onto an IR transparent surface. Filtration, impaction and electrostatic precipitation (ESP) are commonly used methods of sample collection. Filtration has sampling artifacts and size-dependence in collection (Anderson et al., 2002; Modey, 2001) and impactors have material dependent bounce off effects and size stratification (V. A. Marple, 2004). ESP is a versatile method and has low pressure drop unlike both the other methods. Hence, we design an ESP for collecting on an IR transparent crystal.

A two-stage ESP charges and collects particle in two separate stages. Numerous chargers have been developed and use either direct corona discharge to charge the particles (Hewitt, 1957; B. Y. H. Liu and Pui, 1975; Biskos, Reavell, and Collings, 2005; Whitby, 1961; C.-j. Tsai et al., 2010), indirect corona discharge where charged ions in gas flow are generally mixed with the particle flow separately (Medved et al., 2000; Marquard, Meyer, and Kasper, 2006; Kimoto et al., 2010). The indirect chargers have higher charge levels but require a diluted flow. Some chargers also use direct or indirect photoelectric discharge to charge the particles (Burtscher et al., 1982; Grob, Wolf, et al., 2014; Nishida, Boies, and Hochgreb, 2018; Shimada et al., 1999), especially with UV photoionization (Hontañón and Kruis, 2008; Grob, Burtscher, and Niessner, 2013), but generally have strong dependence on the conductivity of the particle material. The strong ionization in the chargers result in reactive molecule formation such as $O_2{}^+$, O^+, $N_2{}^+$, N^+, NO^+, H_3O^+ (Volckens and Leith, 2002; Arnold, Viggiano, and Morris, 1997) and should be avoided in material characterization applications as particle composition is transformed mainly through ozone reactions and through gas to particle conversion (Volckens and Leith, 2002). The wire-wire direct corona charger (T. T. Han, Thomas, and Mainelis, 2017) is designed to lower the ozone concentrations in the charger.

In this work, we approaching the challenge of designing an electrostatic precipitators (ESP) for IR spectroscopy requires exploring the numerous variables involved in the design. Currently, IR spectroscopy is performed on Teflon filters (Russell, 2003; Takahama, A. Johnson, and Russell, 2013) but the interference from Teflon absorbance limits the lower detection limits. The interference can reduced by employing an IR transparent crystal on which the particles can be collected for subsequent analysis. Ofner, Krüger, et al. reported Zinc Slenide (ZnSe) as having better performance than other IR-transparent materials which encourages our decision to use ZnSe discs for transmission-IR measurements (Ofner, Krüger, et al., 2009). We design and fabricate a device and test it for its quantification capabilities.

2.3   Method

In this section, we describe the design objectives (Section 2.3.1), fabrication method using numerical simulations (Section 2.3.2.1) and 3D printing (Section 2.3.2.2) with acrylonitrile butadiene styrene (ABS). The fabricated device and the experimental procedure (Section

2.3.3) was used to collect the particles on a ZnSe crystal which is used to obtain the IR spectra (Section 2.3.4) of the loaded particles. The collection was also characterized for the surface deposition using optical microscopy, electron microscopy and IR analysis (Section 2.3.5). All the measurements were used in conjunction to evaluate the quantitative response of the IR measurement with particle loading (Section 2.3.6).

2.3.1 Radial ESP

A two-stage radially symmetric (radial) ESP was selected for geometry and flow design over the parallel plate (linear) ESP. The radial symmetry in deposition for a radial ESP is consistent with the transmission IR beam profile. It does not have flow and collection directionality that is inherent in the linear system, which could theoretically result in some directional dependence in the particle deposition based on particle size and flow rate. The physical processes of charging and that of collection were divided into two individual instruments (a two-stage ESP) to execute better control on the particle collection. The resulting design blueprint has a particle charger connected to an ESP where the flow enters perpendicular to the collection surface and moves.

One of the critical requirements in the design is to limit the high- electric field strength and voltage in the vicinity of the particles, mainly because regions of high electric field facilitate ion production that modifies the chemical composition of the particles (Ofner, Krüger, et al., 2009). For the first stage, another application where ozone production is an undeniable consideration is personal bio-aerosol sampling and the PEBS sampler's wire-to-wire electrode arrangement in the charger (T. T. Han, Thomas, and Mainelis, 2017) was specifically designed to maintain a low ozone concentration (< 10 ppb). In this work, we employ a similar wire-to-wire charger and design the collector stage with the following desired features (1) Low electric field strength (lower than 1 kV/mm, with a factor of safety 3 over the theoretical breakdown field of air at 3 kV/mm); (2) Low electrode voltage (lower than 10 kV); (3) High collection efficiency (greater than 70%); (4) High flow rate (for example, a 1.7 LPM (2.8×10^{-5}) flow rate would result in a 1 µg total mass collection in 1 hour for an ambient concentration of 10 µg/m^3).

2.3.2 Fabrication and testing

The combination of an electric field limit to 1 kV/mm and a voltage limit of 5 kV imposed a minimum electrode separation distance of 5 mm. For conditions where inertial effects and diffusion effects can be neglected, the collection in the radial ESP is a result of the trade-off between the drag force on the particle parallel to the collection surface (r-direction) and the electrostatic force into the surface ($-z$-direction). For a given flow conditions, a stronger electric field will result in a more efficient particle collection making closest 5 mm separation the most desirable as any larger separation distance would either require that the voltage be higher or E_0 be lower than 1 kV/mm.

2.3.2.1 Numerical simulations

COMSOL Multiphysics was used for numerical simulation of the particle trajectories in a electrostatic and flow field. 2D-axisymmetric simulations allow much faster simulations and the fluid flow was simulated using laminar flow physics. A radial ESP collector (made of ABS) was simulated with a tubular inlet facing the collector surface (ZnSe) resting on the ground electrode, while the high voltage electrodes were places near the outlet of the tube and at a fixed distance above the collection surface (Figure 2.1a) using an extremely fine physics-controlled mesh. The electrostatic field (Figure 2.1b) and the fluid flow field (Figure 2.1c) were simulated using a stationary solver with 10^{-3} relative tolerance for convergence. Despite large scale eddies in the laminar flow simulations no turbulent simulation was required mainly because mesh-refinement analysis yielded identical laminar flow results (for example, changing the mesh to a finer grid resulted in similar flow fields). The in-variance to mesh refinement suggests that the obtained calculations were indeed resolved with laminar physics alone and did not represent a scrupulous flow field.

The two stationary fields were utilized in simulating a time-dependent particle trajectory simulation (Figure 2.1d) with convergence at 10^{-5} relative tolerance. No coupling of the perturbations of the particles on the stationary fields is employed as the particles are very small to cause substantial change. 1000 charged particles were released uniformly spaced at the top of the inlet tube at $t = 0$ till it collected on the surface, collided with a surface or ran-off. The charge levels on the particle was assumed to be proportional to particle diameter (as assumed for diffusion charging) with around 1 elementary charge for every 20 nm diameter (Biskos, Reavell, and Collings, 2005). A couple of additional charges values around the linear value were also simulated for each particle size as the charge can be expected to be higher on larger particles if particle charge is a combined effect of field and diffusion charging (Marquard, 2007). The particle diameter D_p was manually adjusted for the slip corrected factor (M. D. Allen and Raabe, 1985) (eq. 3.3) in the drag force calculations for the particle simulation.

$$C_c = 1 + \text{Kn}\left[1.142 + 0.558\exp\left(-0.999/\text{Kn}\right)\right] \tag{2.1}$$

Collection efficiency was calculated for the particle collection using the number of particles out of 1000 that were collected on the surface – measured through a graph of the cumulative histogram of the particle count against radial position of deposition (calculated from Figure 2.1e). The iterative simulation process was targeted at lowering the fluid velocity while keeping the high voltage electrode 5 mm from the collection surface to maintain the electric field strength. Very large inlet radius had lower velocities but also reduced the residence time over the crystal, also hampering the collection efficiency. The flow rate had a similar trade-off and an acceptable value of collection efficiency for different D_p (100, 200, 400, 600, and 800 nm) was found for an inlet radius of 10mm and a flow rate of 2.1 LPM ($3.5 \times 10^{-5}\text{m}^3/\text{s}$), at the design $E = 1$ kV/mm. An additional nudge on the collection efficiency (from 75% to 80% for 200nm particles with 8 elementary charges) was obtained by incorporating a protrusion that

extended the inlet tube closer to the collection surface while keeping the electrodes at a farther distance (Figure 2.1a). In the end, we satisfice with the design as the possible combinations of the numerical simulations in various design spaces are large.

This work was completed prior to the publication of an analytical radial electrostatic collector model by (Preger et al., 2020). Their model estimates collection spot size as a function of flowrate and electric field strength in a radial collector with parallel plates and small inlet radii. Their model could now be used in selection of collector plate or operating parameters for devices which follow these geometric constraints. An extended dimensionless analytical model which generalizes the model to larger radii and further describes the mapping between particle position in the inlet to substrate has also been developed to facilitate rapid exploration of the design space (Dudani and Takahama, in preparation, 2021).
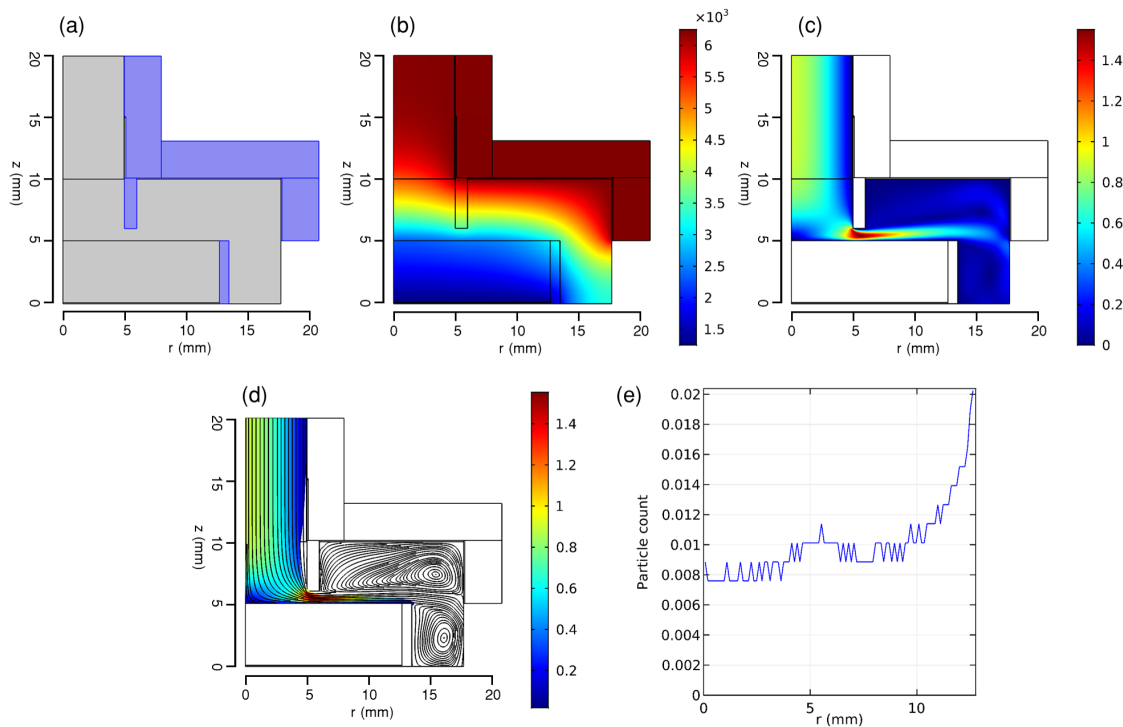
Figure 2.1: Numerical simulations of the ESP device for (a) the device schematic with the outer and inner body (ABS) highlighted (b) Steady state Voltage field (voltage (V) on colorbar), (c) steady state velocity field (velocity (m/s) on colorbar), (d) particle tracing simulation in the steady state field at the last time step, (e) Normalized spatial distribution of the simulated particles (1000) on the collection surface which is also used ot calculate the cumulative count to measure collection efficiency (equal to the fraction of the 1000 particles collected of the crystal).

2.3.2.2 3D printing and prototyping

For rapid-protyping there are limited materials that can be 3D-printed reliably amongst which nylon, ABS and polylactic acid (PLA) are most commonly used. PLA is not stable to heat, is less durable and has known outgassing issues, limiting its application for aerosol chemical analysis. Between ABS and nylon, ABS is more reliable to print but is not as strong as nylon. However, for electrostatic applications, nylon is much higher in the triboelectric series making it prone to more electrostatic losses. Moreover, in our observations the main source of leaks in the initial prototypes was through the in-layer-space between each print layer. The spacing was much higher in nylon as it can absorb moisture during and after printing and results in larger printing defects and layer-separation. The additional strength of nylon is at the cost of it being more brittle and harder to seal, making ABS useful for the application. The strength of ABS is plentiful for inherently low pressure drop ESP applications as it has a yield strength of 25 MPa which is much higher than the expected hoop stress of 1.7 MPa acting on a 50 mm internal diameter cylinder design with a thin 2 mm ABS body operated with an extreme 1 atm pressure.

All the fabrication was done using 3D Systems CubePro 3D printer. Warping, cracking, curling and stringing was reduced with proper printing speed, temperature and layer spacing adjustment. Leveling the print bed regularly led to smoother printed objects as the levels were better adjusted to the filament feed rate. The feed-rate and temperature is self-controlled by the CubePro 3D printer and the print chamber was kept heated generally up to 50 °C. Failure in the chamber heating resulted in poor print quality and is a known problem when printing ABS as lower surrounding temperature results in faster cooling in certain regions. Another common difficulty in printing ABS is poor bed-adhesion over longer 3D-prints. In our observations, using a pre-heated print chamber (to 55 °C) along with a water soluble glue that was applied on the print surface and dried completely before starting each print job, substantially improved bed-adhesion. Finally, the ESP was printed with as few parts as possible to have higher structural stability and avoid forced turbulence because of material discontinuity at the joints. With fewer parts to print, it becomes increasingly important to print parts with complex overhangs. Though using filler materials with dual head printers is a possible solution, it has limited application for larger parts, as the printing volume and time scales cubically to the size on top of which printing the entire hollow part with a filler substantially increases the chances of print failure. An alternative approach that we utilized was printing the parts tilted at 45 °. In this manner the parts which have an angle of 90 °or lower ranged within ±45°with respect to the bed and hence were all inter-supported, and further strengthened by utilizing simple line or point supports on the surfaces. In combination with making the base on the print bed larger promoted bed-adhesion and using side supports even the surfaces supported at the largest theoretical angle (45 °) still printed reliably.

Gas leak through the areas where two parts join and the layer spacing in the print surface was reduced through several means. The junctions where two parts assemble were sealed by extending the joining surfaces outward to act as larger flanges, and were sealed using an o-ring

placed in a groove designed for the static axial (face) assembly where the pressure is lower on the interior. The flanges and the greased o-ring was assembled together using multiple screws along the circumference, using latches, magnets, or clips. The inter-layer spacing in the 3D prints was sealed along with smoothening the rough 3D-printed surface by manually rubbing the outside surface with acetone while pressing down on the surface. Similar to painting, the method worked well when no spots were left while press-sealing the outside surface. It is known that ABS dissolves in acetone and conventionally acetone vapor baths have been used to smoothen the surface where the part is hung in a container/ chamber with acetone vapor, but in our observation the method resulted in overly softened parts/ unsealed portions numerous times due to the sensitivity to the bath time and the acetone amount. The surface and joint sealing procedure was repeated until the assembled device could hold vacuum at levels of -10 kPa for over 5 minutes. To find holes/ leaks in a negative gauge pressure system is challenging, hence, a positive internal gauge pressure was used instead and the leaks were detected using soap-solution which bubbles when applied over holes. The positive pressure was created using a compressed air flow through the assembly, rather than a static pressure in closed system to avoid a pressure buildup inside 3D printed parts, which is a safety concern. Applying the soap solution over the entire printed surface and joint areas would highlight specific points of leaks which were then sealed. Use of acetone to press-seal was less useful for nylon, where the larger gaps were sealed with a coat of epoxy solution instead which was thinned using acetone for easier application, but this process required longer time for part preparation and had higher chances of smaller holes remaining after treatment because of higher surface tension of the epoxy solution, further adding to the complexity of working with nylon. Apart from ABS, which was used consistently for fabricating of the two stages of the ESP, the high voltage electrode inside the charger was insulated in thin glass tubes.

2.3.3   Experimental Setup

Based on the design analysis and prototyping, the final device is designed design (Figure 2.2b) using a 3D-CAD software (Figures 2.2a and 2.2c) and assembled after 3D-printing and post-treating (2.2d). The particle size-distribution, at different ESP stages, was measured using a Scanning mobility particle sizer (SMPS) setup (Figure 2.3a). Another setup was used for mass loading experiments with CPC raw counts (Figure 2.3b), as a higher resolution on the collection start and end time along with lower latency was desired in the response to reduce bias in mass measurements. Ammonium sulphate $(NH_4)_2SO_4$ particles were nebulized from a 5 g/L concentration solution in milli-Q water and dried using silica gel denuder. The particles were size selected using a $1\mu m$ cut-off cyclone impactor and the concentration was adjusted with a dilution system before introducing the particles into the ESP. Different bypass lines (red-dotted flow lines) were setup to measure the size-distribution/ particle count at different flow-line points. A mass flow controller (MFC) with a vacuum pump was used to maintain the desired ESP flow (2.1 LPM). Two identical ZnSe collection crystals (WG71050 from Thorlabs Inc.) were used for all the mass loading experiments. The crystal was cleaned with iso-propyl-alcohol (IPA, =99.8% (GC), Sigma Aldrich) and a clean wipe (Kimberly Clark

7552) between each loading and IR measurement.

(a)

(b)

(c)

(d)
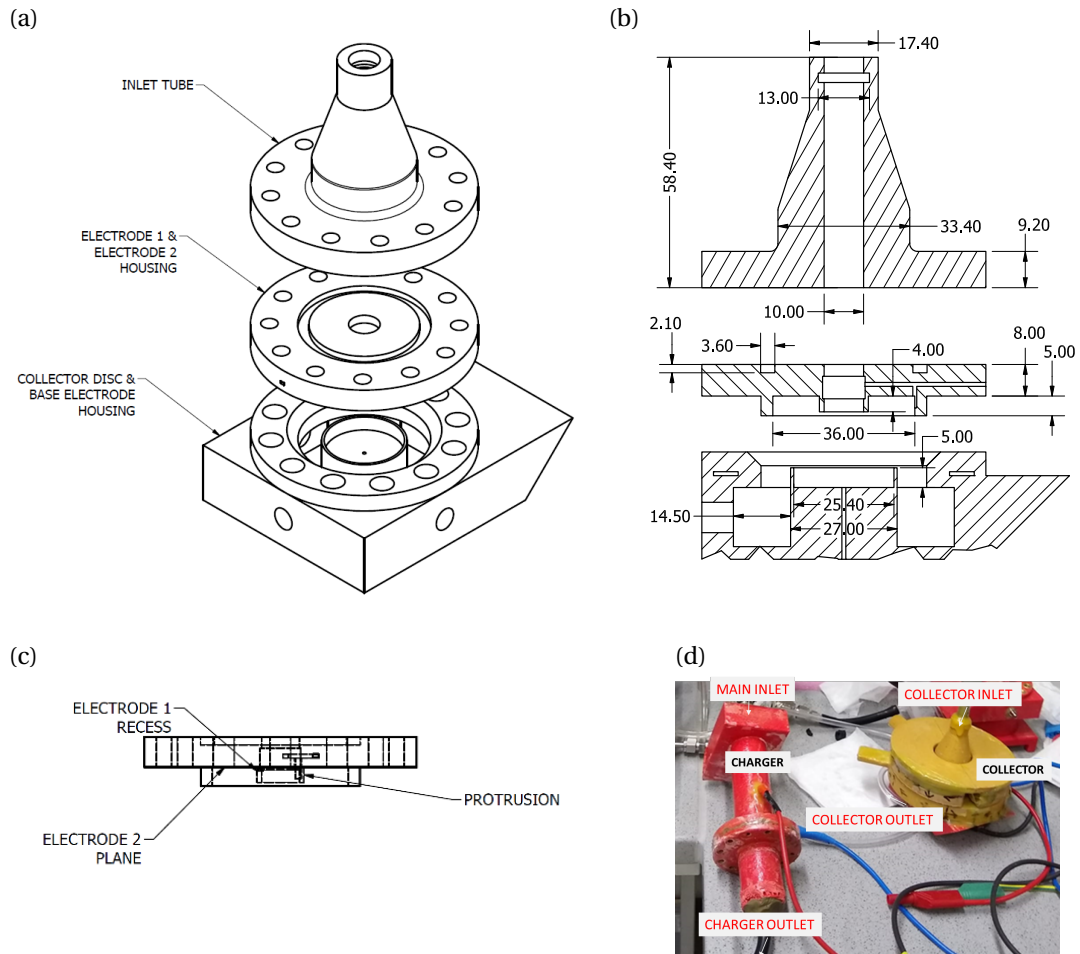
Figure 2.2: (a) Engineering drawing of the device assembly, cross-section view with dimensions (in mm), (c) side view of the electrode housing part with the protrusion visible, and (d) fabricated and assembled device with the different parts labelled.

The size-distribution experiment (Figure 2.3a) resulted in a series of mobility diameter distribution (from 17.5 nm to 982 nm) with a scanning phase of 210 s and a down-sampling time of 30 s, using a combination of the differential mobility analyzer 3081 and CPC 3772 (TSI Inc.). Particles were generated continuously from a freshly prepared $(NH_4)_2SO_4$ solution. Size distributions $s = dN/d \log D_p$ with 6, 20 and 33 scans at three points of interest: at the inlet of the ESP (n^{in}), the outlet of the charger (n_{ch}^{out}) and the outlet of the collector (n_{col}^{out}). Additionally, n_{ch}^{out} and n^{in} were measured again at the end of the experiment, with 6 and 13 scans respectively. The mass mean diameter was computed from the size distribution of $s_{ch}^{out} - s_{col}^{out}$.

The transient raw particle count experiment (Figure 2.3b) was conducted for different collection intervals, Δt (from 5 minutes to 3 hrs) and adjusting the particle concentration n_{ch}^{out} to

21

(a)

(b)
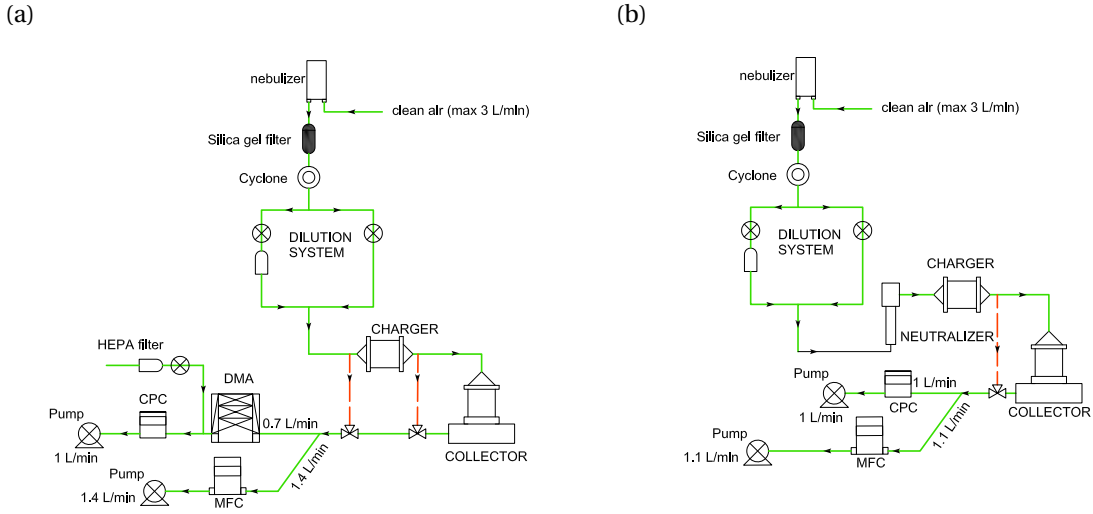
Figure 2.3: Flow diagram of the experiment setup (green line is the main flow line and the red-dotted lines are the alternate bypass lines) for (a) obtaining the particle size distribution, and (b) obtaining the mass loading reference through the CPC particle counts.

around $9000 - 10000$ particles/cm^3 i.e. below the operating limit of the CPC. The flow line is switched from measuring n_{ch}^{out} from the bypass to n_{col}^{out} in the main line at a resolution of 1 measurement per second. The corresponding change in the concentrations (Figure 2.4) is used to estimate the number of particles collected (N^*). $n_{col}^{out}/n_{ch}^{out}$ is not representative of the collection efficiency as some particles could be uncharged and subject to other conditions (temperature and humidity). The measured $N^* = \left(n_{ch,avg}^{out} - n_{col}^{out} \right) Q\Delta t$ is used as the reference for collected mass (Section 2.3.6) The concentration at the outlet of the charger changes during the experiment from which the error is estimated $N_{error}^* = \left(n_{ch,start}^{out} - n_{ch,end}^{out} \right) Q\Delta t$.

2.3.4 Infrared spectroscopy

The IR absorbance spectra of the particle loaded and clean ZnSe crystal were measured with the Vertex 80 with Deuterated Lanthanum Alanine doped TriGlycine Sulphate (DLaTGS) detector. The spectra was measured after purging the measurement chamber for 3 minutes after introducing the sample into it, and was an average of 64 scans over $4000 - 400$ cm^{-1} with 4 cm^{-1} resolution. The spectra was measured with the purged chamber as the background and the default aperture setting of the aperture pre-fitted with the spectrometer was 6 mm diameter corresponding to a 80% higher beam spot diameter (Bruker rep., personal communication, 2018).
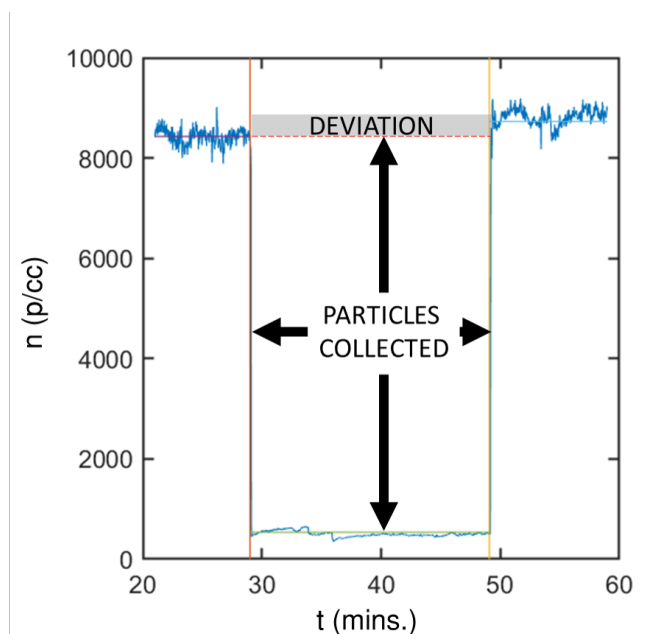
Figure 2.4: Transient particle count from the CPC used to calculate the total number of particles collected for the collector on state, along with the error calculated using the difference between the starting and the ending particle count in collector off state.

2.3.4.1 Baseline correction

The raw IR spectra is processed to correct the baseline which can change over the collection period because of the change in the background spectra of the IR chamber. In this work, $(NH_4)_2SO_4$ was the only test material and a method that automatically corrects the baseline is employed. First, the absorbance spectra of the cleaned collection crystal is subtracted from the particle-loaded absorption spectra, which is then y-shifted to bring the minimum value to 0. The slope of absorbance values is used in combination with the moving mean of absorbance to identify baseline points (example in Appendix B.1 Figure B.1). This was done by setting limits on the moving mean and moving standard deviation on the slope of absorbance spectra. As the change in slope for sharp peaks or even broader peaks is higher than that for the baseline regions, using a combination of the change in the mean value and the deviation in slope allowed separating the baseline form the absorbance regions. For identifying the broad peaks, the moving mean of the absorbance itself is additionally used to separate it from the background. The method has not been evaluated for other material absorption spectra.

2.3.5 Spatial profile

2.3.5.1 Optical image analysis

An analysis of the spatial distribution of particles was made from the top-view image of the ZnSe crystal after deposition. Using a dark background to contrast the bright ammonium

sulfate particles, we took an image of the particle loaded crystal under diffused light using a digital camera (Firefly DE300, focal dept of 35mm with 2048 ×1536 pixel resolution) kept at a fixed height of 30 cm. The image was analyzed by converting to gray scale (0 to 255 pixel intensity), and finding the radial change in pixel intensity from the analyzed center and periphery of the crystal.

2.3.5.2 Electron microscopy analysis

Scanning electron microscopy (SEM) analysis was performed to qualitatively assess the particle distribution at different radial positions using the FEI Teneo microscope. Secondary electrons were detected using the Everhart-Thornley detector (ETD) detector while using a 5 kV voltage and low 50 pA current to prevent charge build up on the particles. The crystal was introduced in the SEM chamber without any conductive coating and images were taken from a working distance of 6 mm.

2.3.5.3 Variable aperture IR-spectroscopy (VAIRS)

IR absorbance intensities for different apertures (0.25 to 8 mm) were used to compute the surface mass distribution. By varying the aperture, and consequently the beam spot size on the surface (which is around 80% larger than the aperture), the observed change in absorbance intensity was representative of the areal mass density of the deposition under the beam. From the difference in intensities among successive beam areas, the mass per unit annulus area was estimated.

2.3.6 Quantitative evaluation

We consider that the the areal number concentration of deposited particles N_a is dependent on size and radial position on the crystal. The spatially-integrated size distribution of deposited particles is determined by the collection efficiency η and number size distribution $N^{\#}$ of particles that entered the collector.

$$\frac{d(\eta(\ln D_{\mathrm{p}})N^{\#}(\ln D_{\mathrm{p}}))}{d\ln D_{\mathrm{p}}} = 2\pi \int_0^R r' \frac{\partial N_a(r,\ln D_{\mathrm{p}})}{\partial \ln D_{\mathrm{p}}} dr' \tag{2.2}$$

Given mass density of substance (ρ), the mass deposited over unit area (m_a) and integrated areal mass density (m_a^*) within radius r are given from the deposited volume size distribution.

$$m_a(r) = \rho \frac{\pi}{6} \int_{D_{\mathrm{p,min}}}^{D_{\mathrm{p,max}}} D_{\mathrm{p}}^3 \frac{\partial N_a(r,\ln D_{\mathrm{p}})}{\partial \ln D_{\mathrm{p}}} d\ln D_{\mathrm{p}} \tag{2.3}$$

$$m_a^*(r) = \frac{2}{r^2} \int_0^r r' m_a(r') dr' \tag{2.4}$$

From eqs. 2.2–2.4, the total mass deposited per unit area of the disc is

$$m_a^*(R) = \frac{m^*}{\pi R^2}, \text{ where } m^* = \rho \frac{\pi}{6} \int_{D_{p,min}}^{D_{p,max}} D_p^3 \frac{d(\eta(\ln D_p) N^{\#}(\ln D_p))}{d \ln D_p} d \ln D_p \tag{2.5}$$

m^* is the total deposited mass, which is calculated from the product of the analyte density ρ, the volume $\bar{V}_p = (\pi/6)\bar{D}_p^3$ corresponding to a particle with mass mean diameter $\bar{D}_p$ obtained from the SMPS, and the the cumulative number of particles collected N^* as determined from the CPC (Section 2.4.1) and flow rate, Q.

$$m^* = \rho \bar{V}_p N^* = \rho \frac{\pi}{6} \bar{D}_p^3 (\bar{n}_{ch}^{\#} - n_{col}^{\#}) Q \Delta t$$

The scattered intensity is interpreted as being proportional to mass loading (Sisler and Malm, 1994). Therefore, the radial beam intensity distribution I can be written in terms of m_a and the integrated beam intensity I^* in terms of m_a^*.

$$I(r) \propto 2\pi \int_r^{r+\Delta r} r' m_a(r') dr' \tag{2.6}$$

$$I^*(r) \propto \pi r^2 m_a^*(r) \tag{2.7}$$

The areal mass density ratio is estimated from the integrated beam intensities at two radii r and r'.

$$\phi_r(r') = \frac{m_a^*(r')}{m_a^*(r)} = \frac{I^*(r')/r'^2}{I^*(r)/r^2} \tag{2.8}$$

The consistency in spatial profile of deposition is embodied by the magnitude of variation in $\phi_R(r_b)$ across samples. As it is the ratio of average intensities ($I^*(r)/r^2 = \bar{I}(r)$), we calculate it using the image analysis of $\bar{I}(R)$ and $\bar{I}(r_b)$ such that $\phi_R(r_b) = \bar{I}(r_b)/\bar{I}(R)$ (Section 2.4.2).

Neglecting scattering interactions between particle and crystal and among particles, the apparent absorbance A is related to the areal mass density of particles $m_a^*(r_b)$ within the radius of the beam r_b and the decadic volume attenuation coefficient $\alpha_{10,v}$ (Adamson, 1979; Bohren and Huffman, 1983; Hapke, 2012).

$$A(\tilde{v}) = -\log_{10} T(\tilde{v}) + \log_{10} T_c(\tilde{v}) = \alpha_{10,v}(\tilde{v}) \frac{m_a^*(r_b)}{\rho} \tag{2.9}$$

$m_a^*(r_b)/\rho = N_a^* \overline{V}_p$ can be interpreted as the areal volume density of particles with N_a^* and $\overline{V}_p$ as the areal number density and mass equivalent volume of deposited particles, respectively; or the hypothetical path length through the same mass of bulk substance (ammonium sulfate). The transmittance T is obtained by ratioing the sample spectrum to single-beam background

of the purged chamber and T_c is the transmittance obtained by ratioing the clean ZnSe crystal to the purged chamber background prior to the experiment. Values of $m_a^*(r_b)$ are calculated experimentally from eqs. 2.5 and 2.8.

$$m_a^*(r_b) = \phi_R(r_b) m_a^*(R) \tag{2.10}$$

For evaluation $\alpha_{10,v}(\tilde{v})$ is estimated from individual experiments by dividing the apparent absorbance $A(\tilde{v})$ by $m_a^*(r_b)/\rho$ or collectively determined by calibration for specific wavenumbers at peak apexes. These values are compared against theoretical values of the volume attenuation coefficient and bulk linear absorption coefficient. Given the size range of particles used in our study, we assume that absorption is the dominant process leading to attenuation of IR radiation by particles (Rayleigh regime). In the electrostatics approximation (Hulst, 1957), the volume attenuation coefficient is related to the vacuum wavenumber $\tilde{v}$ and complex refractive index $\tilde{n}$ of the substance comprising the particles (Bohren and Huffman, 1983).

$$\alpha_{10,v}(\tilde{v}) = \frac{6\pi\tilde{v}}{\ln 10} \operatorname{Im}\left\{\frac{\tilde{n}^2(\tilde{v}) - 1}{\tilde{n}^2(\tilde{v}) + 2}\right\} \tag{2.11}$$

In contrast, the bulk decadic linear absorption coefficient α_{10} for a homogeneous medium that would be used in place of $\alpha_{10,v}$ in eq. 2.9 follows a different relation with the refractive index and is also used as a point of comparison.

$$\alpha_{10}(\tilde{v}) = \frac{4\pi\tilde{v}}{\ln 10} \operatorname{Im}\{\tilde{n}(\tilde{v})\} \tag{2.12}$$

For a collection of tenuous particles (Rayleigh-Gans-Debye approximation), the two are related in the weak absorption limit as $\alpha_{10,v} \approx \alpha_{10}$ (Bohren and Huffman, 1983), but this condition does not strictly applied here due to the sharp contrast in the refractive index of ammonium sulfate and that of the surrounding medium (air). $\alpha_{10,v}$ is evaluated in Section 2.4.3.

2.4 Results and discussion

2.4.1 Evaluation of collection efficiency and size distribution

The measured particle size distribution at the charger inlet (n_{avg}^{in}), charger outlet ($n_{ch,avg}^{out}$) and collector outlet (n_{col}^{out}) according to the described method (Section 2.3.3) shows a charger penetration of 80% and a collection efficiency of 80% on the fraction of particles at the charger outlet (Figure 2.5a). The Figure 2.5b shows the corresponding normalized size distribution, where the charger inlet distribution at both the start and at the end of the experiment are included to provide an estimate of expected change in the distribution over the long sampling experiment. The collector did collect some larger particles preferentially but qualitatively there was no large shift in size distribution because of the charger or the collector. Contrary to the observed

nominally higher collection for larger particles, COMSOL simulations showed a nominally decreasing collection efficiency with increasing particle size (as the electrical mobility was decreasing) for a charge level proportional to the diameter. The discrepancy is mostly because of larger fraction of larger particles getting charged vs. un-charged in the charger. Numerical simulations had a similar 80% collection efficiency for $D_p = 100, 200, 400, 600,$ and 800 nm with 4, 8, 20, 36, and 48 elementary charges respectively. Qualitatively, the particle distribution imaged by the SEM (Figure 2.6) is similar at the three positions and support the idea that there is lower size segregation in collection. It was observed that the particles were not closely connected but spatially separated, as expected below 5-20 µg/cm^2 (Casuccio et al., 2004), but supports Rayleigh scattering.

(a)   (b)
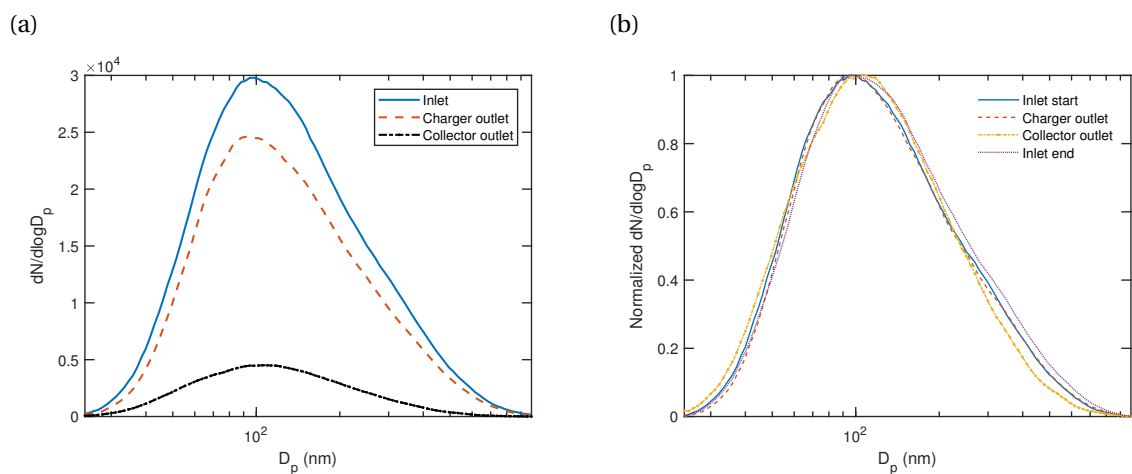
Figure 2.5: (a) Particle size distribution measured at the inlet averaged from that before and after collection, at the charger outlet averaged from that before and after collection and at the outlet of the collector, and (b) normalized particle size distribution measured for the inlet before staring the experiment, at the outlet of the charger, at the outlet of the collector, and the inlet at the end of the experiment (to determine any bias in the inlet).

(a)   (b)   (c)
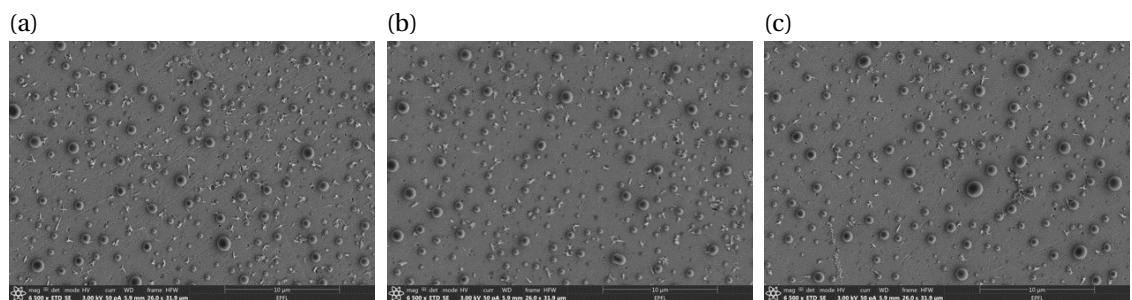
Figure 2.6: Scanning electron microscopy (SEM) images of the particle collection at a radius (a) 1 mm, (b) 6 mm, and (c) 9 mm away from the center. All the scale bars are 10 μm long.

2.4.2 Spatial mass distribution
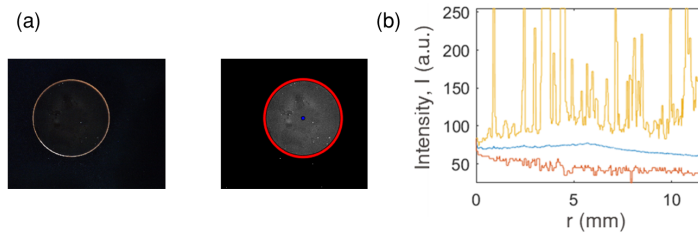
Figure 2.7: (a) (Left) Top view image of particle loaded crystal and (right) the corresponding processed image (gray scale with center and circumference position), (b) Radially changing average (blue), maximum (yellow) and minimum (red) gray scale intensity (0 to 255) calculated from the processed image in part a.

The three methods of evaluating the spatial profile (Section 2.3.5) show that the deposition is semi-uniform. The radial dependent pixel intensity for all experiments (Figure 2.8b) was calculated from the optical image (example Figure 2.7). The spatial profile is semiuniform; and has variable profile among the experiments. Some profiles have a prominent mound near the point where the device inlet tube extrudes towards the surface (r = 5mm). Moreover, there is a difference in whether the deposition is increasing or decreasing with the radial distance. The presence of the mound is supported by qualitative SEM image analysis which has nominally different particle densities for the different images at different radial positions (1, 6 and 9 mm) (Figure 2.6), despite having low qualitative variation in the size distribution. The VAIRS analysis (Section 2.3.5.3) of the IR absorbance spectra with different aperture sizes, also closely follows the image analysis profile (Figure 2.9, Figures B.1 and B.2), though it is much coarser because of limited number of aperture points.

The pixel intensity distribution has merit for analysis as the average intensity over the entire crystal for the experiments do scale with the mass loading (Figure 2.8a). The average intensity ratio $\phi_R(r_b)$ (for a beam radius of 5.4mm corresponding to the aperture of 6mm diameter) estimates for the experiments is the slope of each point on a $\bar{I}(r_b)$ vs. $\bar{I}(R)$ graph (Figure 2.10). Theoretically a perfectly uniform distribution should have $\phi_R(r_b) = 1$ and the observed values are within ±12% i.e. congruent with a semi-uniform deposition. The proximity of $\phi_R(r_b)$ to 1 is mainly because the absolute intensity values are high (Figure 2.8b) and because the beam radius (5.4 mm) is around the middle point of the mounds (near 5 mm). $\phi_R(r_b)$ is much higher than 1 if the intensity profile increases sharply with radius and much lower than 1 for profiles which have decreasing radial intensities (Figure 2.8b). The variation in the relative mound intensity suggests that the differences in the distributions across experiments have most likely been a result of small perturbations in the vertical position of the crystal placed in the collector disc housing (Figure 2.2a). Applying a nonuniformity adjustment ($\phi_R(r_b)$) at the level of each sample does not appear to confer noticeable benefits, resulting in the quantitative evaluation (Section 2.4.3) with $\phi_R(r_b) = 1$. Having a more uniform spatial distribution can eliminate the

requirement of optical microscopy analysis altogether.
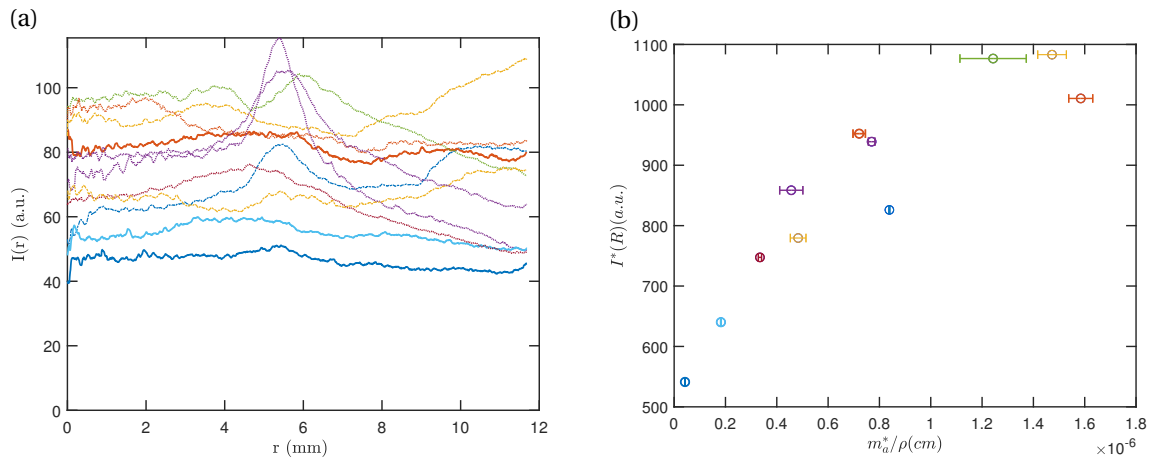
Figure 2.8: (a) Radially changing average intensity (similar to that in Figure 2.7b)for all the experiments labeled by the area under the average intensity curve, (b) the integrated area under the average intensity curve for each experiment against the volume areal density with the same color of the points as (a).
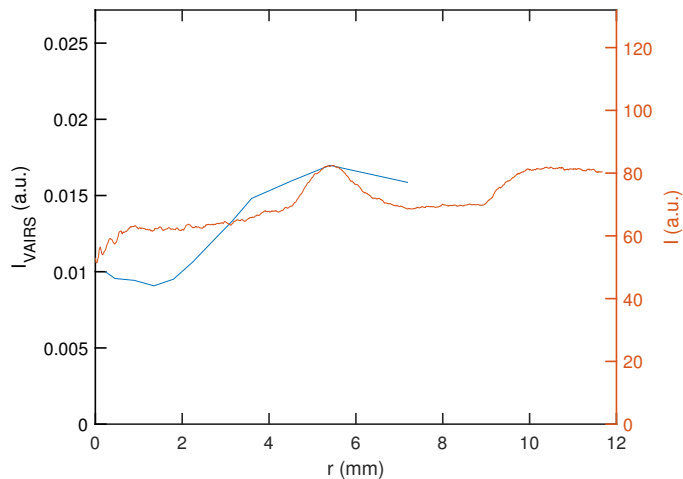
Figure 2.9: Comparison of the m/A profile obtained from variable aperture IR spectroscopy (VAIRS) with the average intensity profile that obtained from the image analysis.

2.4.3   Evaluation of absorbance against reference measurements

We test how the IR absorbance (which is related to deposited mass) scales with higher loading. For a system with low size segregation, we expect the absorbance to scale linearly with the loading (Rayleigh regime approximation).

The experimentally-determined volume attenuation coefficient are shown in Figure 2.11. The absorbance peak locations and their magnitudes are generally in good agreement, indicating
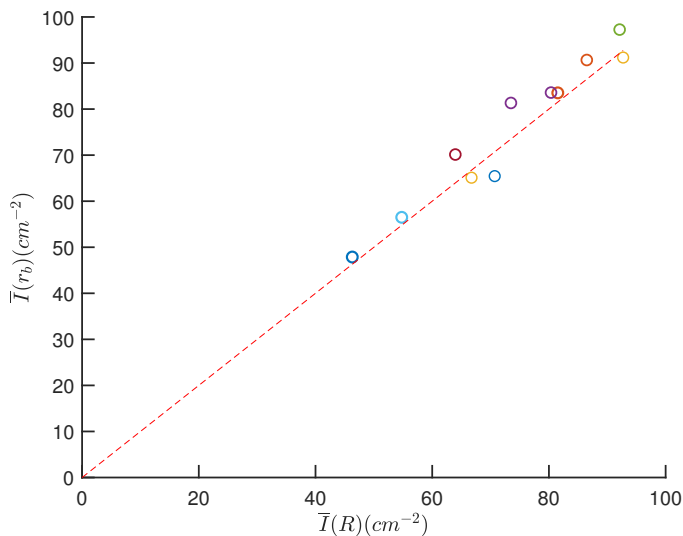
Figure 2.10: Calculated $\bar{I}(r_b)$ and $\bar{I}(R)$ from image analysis for the experiments with different $m_a^*(R)$ (points colored according to Figure 2.8) and a 1:1 reference line (red-dotted line).

that the method of measurement and baseline correction does not introduce major chemical or spectroscopic artifacts. Some absorption peaks for aliphatic CH is visible, likely due to impurities on the crystal originating from the o-ring sealing grease in the crystal housing during manual removal of the sample. The spectra does not appear to contain peaks related to nitrates or other additional artifacts that may be caused by spark discharge and formation of reactive molecules near regions of high electrical potential in the charger or collector. (Such peaks in initial stages of ESP-development were observed where needle electrodes and high voltages were used for charging and collection in a single stage design.) Moreover, no physical heating of the ZnSe crystal was observed after each experiment, which also suggests the absence of sparking and substantial production of reactive gases.

Overlayed on Figure 2.11 are $\alpha_{10,\nu}$ and α_{10} calculated from refractive indices measured by (Earle et al., 2006) using ammonium sulfate particles suspended in nitrogen gas in an aerosol flow tube. In our experiments, we observed a consistent peak positions of $\nu_3(SO_4^{2-}) = 1090$ cm^{-1} ($\pm 0.2\%$) and $\nu_4(NH_4^-) = 1415$ cm^{-1} ($\pm 0.08\%$), which are consistent with reported values for homogeneous samples (Toon et al., 1976) [$\nu_3(SO_4^{2-}) = 1090$ cm^{-1}, $\nu_4(NH_4^-) = 1415$ cm^{-1}] and (Torrie et al., 1972) [$\nu_3(SO_4^{2-}) = 1093$ cm^{-1}, $\nu_4(NH_4^-) = 1417$ cm^{-1}] — though the lack of wavenumber resolution in the older measurements made on dispersive spectrometers prevent a more precise comparison. Blue shifting of peaks on the order of $\sim$10 cm^{-1} can be expected for small particles (Bohren and Huffman, 1983; Maidment et al., 2018), with asphericity and increasing particle size reducing the extent of this shift (Mishchenko, 1990; Segal-Rosenheimer, Dubowski, and Linker, 2009). Blue-shifts have been reported in extinction spectra of ammonium sulfate in aerosol flow tubes (Weis and Ewing, 1996; Earle et al., 2006; Segal-Rosenheimer, Dubowski, and Linker, 2009; Laskina et al., 2014), though observations are often below that predicted by Mie theory. Such shifts are not observed in our experiments,

though the extent of peak shifts, spectral profiles, and the underlying refractive indices vary among various studies (Laskina et al., 2014; T. J. Johnson et al., 2020; Myers et al., 2020) and are attributed to some extent on differences arising from sample morphology. In our experiments the peak height ratio of $v_3(SO_4^{2-})$ to $v_4(NH_4^-)$ was 2.1 ($\pm$10%); consistent with spectra acquired from nebulized and dried polydisperse ammonium sulphate solution (4.8 g/L) with mass mean diameter of 200 nm studied under conditions close to our experiments (Weis and Ewing, 1996).
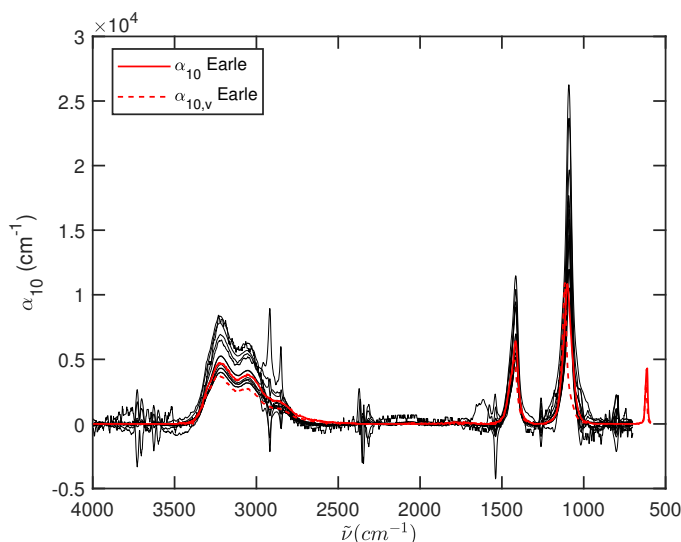
Figure 2.11: Comparison of volume absorption coefficient (α_v) from the experiments for IR measurement with an aperture of 6mm against the reference linear absorption coefficient (α_{ref}) and volume absorption coefficient ($\alpha_{v,ref}$) for ammonium sulfate calculated using n and k (Earle et al., 2006).

Figure 2.12 shows the absorbance against the effective path length for the $v_3(SO_4^{2-})$ peak near 1110 cm^{-1} and $v_4(NH_4^-)$ peak near 1410 cm^{-1}, the slope of which can be compared to $\alpha_{10,v}$ and α_{10} calculated from the refractive indices of (Earle et al., 2006). The reference values are calculated for their respective peaks which vary by a few wavenumbers from our experiments, as mentioned previously. The experimental absorbance and effective path length estimates are strongly correlated (R^2 of 0.96 and 0.94, respectively). The slope values of 1.5×10^4 cm^{-1} (for the peak near 1110 cm^{-1}) and 6.7×10^3 cm^{-1} (for the peak near 1410 cm^{-1}) vary from estimated reference values within 35% and 5% respectively, which is reasonable considering the variation in reported refractive indices (Laskina et al., 2014; T. J. Johnson et al., 2020; Myers et al., 2020). While weak bands are typically recommended for quantification of analytes of inorganic substances (Mayo, F. A. Miller, and Hannah, 2004) due to possibility for signal saturation, for low loadings (low optical depths) for which single scattering approximation applies, this work confirms that even the strongest absorbance band of $v_3(SO_4^{2-})$ at 1110 cm^{-1} exhibits high linearity and can also be for quantification.

In the analysis above, the role of the ZnSe crystal in the analysis was not explicitly considered.
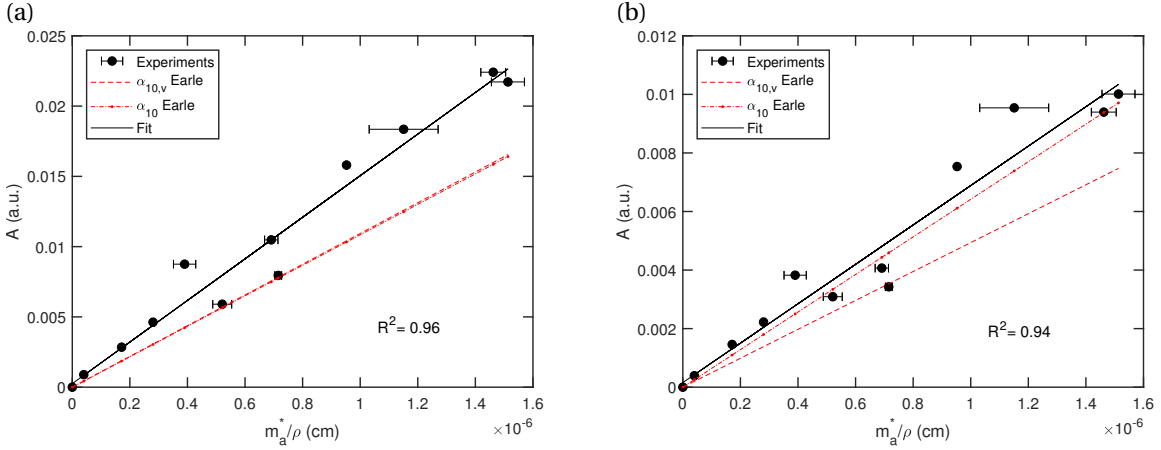
Figure 2.12: Response of IR absorbance (A) against the volume areal density (cm) of the total particle collected reference from CPC transients graphs (Figure 2.4) calculated using no image analysis ($\phi_R(r_b) = 1$), for (a) absorbance at the peak near 1110 cm^{-1} (for $\nu_3(SO_4^{2-})$) and (b) at the peak near 1410 cm^{-1} (for $\nu_4(NH_4^-)$).

Nonmetallic particles collected on the surface of a substrate can behave optically different from suspended particles due to multiple far-field scattering interactions, van der Waals-like interactions, and superposition of incident and reflected electromagnetic fields between particle and surface (Quinten, 2011). For the purposes of the transmission measurement, the reflection by the ZnSe crystal is handled through the single-beam background and scattering power of IR radiation by submicron particles is reasonably small (though increasinly important in the region above 1500 cm^{-1} for larger particles within this range, but to some extent handled by baseline correction) so these far-field interactions are not considered to be substantial. Otherwise, deviations in our measurements were within uncertainty of past reference measurements, and systematic influences of near-field optical effects or physical interactions were not detected within the precision of our technique.

We also consider the value of the optical microscopy experiments in our quantification. Instead of assuming $\phi_R(r_b) = 1$ for all samples, using the $\phi_R(r_b)$ determined from image analysis results in a shift of the points along the abscissa for each experiment compared to Figure 2.12 (Appendix B.3 Figure B.4), but the correlation with absorbance remains essentially the same (R^2 of 0.96 and 0.94 for the 1110 and 1410 cm^{-1}, respectively, Figure B.2b). The estimated slope is within ±15% of the original values and is not systematic, as the variation across individual points is larger than the overall trend between the effective path length estimated from $m_a^*(r_b)/\rho$ and $m_a^*(R)/\rho$.

Finally, we estimate the lower detection limit (LDL) and of the device. The experiment with the lowest volume areal density (Figure 2.12) corresponds to a mass areal density ($m_a^*(R)$) of 75ng/cm^2 which is a total of 415 ng on the crystal. This estimate is the upper bound on the LDL. The lower limit on LDL is calculated at 6 ng (Appendix B.3) using a signal-to-noise analysis

(SNR) (Armbruster and Pry, 2008) and 259 ng using the slope analysis of the calibration curve at low loading (Centre., 2016). The SNR method analyses the lowest concentration (based on experimentally available data) for which the signal is differentiable from the blank (noise). The calibration curve analysis should provide similar values if analyzed over low concentrations (such that the largest loading is 10 times higher than the LDL) and if the data has homoscedasticity. For the experimental calibration, however, as both the assumptions for the LDL analysis using the calibration curve slope and residual are not completely satisfied, we expect a gross overestimation (Centre., 2016). Using a weighted average of both the methods we estimate a lower limit on LDL of 82 ng.

2.5   Conclusions

This work demonstrates the possibility of using a radial ESP for quantitative infrared spectroscopy. Numerical simulations are used together with 3D-printing for prototyping. 3D-printing parts rotated at 45°to allow fabrication of parts with overhangs, and press-sealing with a small amount of acetone was useful in sealing surfaces in devices printed from ABS. Polydisperse ammonium sulfate particles were atomized from solution and studied over 11 experiments with varying particle loading. Since the collection area in the ESP is not fixed as for filter samples commonly used for aerosol spectroscopy, the collection area and spatial distribution of particles on the crystal were analyzed using optical image analysis and IR absorbance measured across variable aperture sizes. The mass distribution was estimated to be semiuniform, likely due to the variation in electrode distances and electric field strengths within the collector. We observed the IR absorbance to scale linearly (R^2 = 0.94 - 0.96) with particle loading over two orders of magnitude, with an estimated detection limit on the order of 100 ng. The peak positions and peak heights of the extinction spectra were within the variability of previous studies, and particle-substrate effects were not discernable. Using such a device can eliminate substrate interferences currently experienced with various filter media on which infrared spectroscopy is conducted, leading to enhanced time resolution (due to lower detection limit) and chemical resolution (due to optical access to regions otherwise limited by scattering or absorption by current filter media). These conclusions encourage further investigation of this analysis approach with other substances, and its use in studies of aerosol composition for a number of applications.

3 Design of an electrostatic aerosol collector part 1: dimensionless analytical model for mapping inlet particle positions to collection surface

Chapter 3. Design of an electrostatic aerosol collector part 1: dimensionless analytical model for mapping inlet particle positions to collection surface

3.1 Abstract

Particle collection on a substrate is important for a wide range of scientific and engineering fields. In atmospheric technology, collecting aerosols has been instrumental for optical or spectroscopy investigations. In some cases, electrostatic precipitators (ESPs) presents unique advantages. The process of development of most ESPs has largely involved iterative prototyping to achieve independent devices, and few studies have investigated analytical tools that could evaluate geometric or operating parameters for a desired collection performance. This paper highlights the development and evaluation of a dimensionless analytical model for modeling particle deposition in a radial ESP. The dimensionless terms independently characterize collection performance, device geometry, operating condition, and particle properties. Deposition and collection of particles onto a dielectric substrate predicted by the model is evaluated against a range of detailed numerical simulations and past experimental designs. A new visualization is proposed to represent the collection performance of the radial ESP system over a large range of possible operating conditions and geometry simultaneously. The analytical model explains even large-scale differences in particle collection between numerous device designs through its dimensionless numbers, and stands as an effective tool and opens a realm of possibilities for new ESP designs with varied objectives and applications and for tuning existing devices to operate at desired performance.

Keywords: Collection, ESP, model, dimensionless.

3.2 Introduction

Particle deposition or collection is used by the semiconductor industry (Montgomery et al., 1992), material development (P. R. Somani, S. P. Somani, and Umeno, 2006), atmospheric particle analysis (D. T. Allen et al., 1994), and numerous other applications. For example, particle deposition is used for thin film creation (D. Lee, Rubner, and Cohen, 2006), membrane seeding process (R. Lai and Gavalas, 1998), coating processes (C. Li et al., 2006), and aerosol sampling. The collection process can create bulk material (Sukhorukov et al., 1998), monolayer (Maoz and Sagiv, 1984; Gun, Iscovici, and Sagiv, 1984) , or a sub-monolayer (Riha et al., 2013) of particles. Various methods are used to sample aerosol particles and are widely used in monitoring stations, off-site samplers and on-site devices. Passive samplers, which mainly rely on gravity for collection are unable to collect smaller micro-particles and thus, numerous active samplers are widely used, such as impactors, cyclones, impingers, filters and electrostatic precipitators. In general, impactors, filters and electrostatic precipitators are more commonly used.

Electrostatic precipitation (ESP) is a versatile method of collection and does not suffer from high pressure drop (which can modify the aerosol chemical composition, for example in filtration), or from bounce-off effects (which preferentially samples a size range and liquids, for example in impaction). ESP is a common device for dust removal (generally wire-to-

plate or point-to-plate devices) but is also used for particle deposition (generally parallel plate devices). Furthermore, ESP has the advantage (Kala et al., 2012) of higher collection efficiency, and deposition tunability. The advantages have led to numerous ESP designs for collecting ambient aerosols (McDonald and Biswas, 2004; Dick et al., 2003) or bio-aerosols (T. T. Han, Thomas, and Mainelis, 2017). Particles collected through ESP have been subsequently analyzed using microscopy or spectroscopy analysis. For example, observation with optical microscopy (Chippett and Gray, 1978), scanning electron microscopy (SEM) (B. Y. H. Liu, Whitby, and Yu, 1967), transmission electron microscopy (TEM) (Fierz, 2007), attenuated total reflection (ATR) infrared (IR) spectroscopy (Ofner, Krüger, et al., 2009), or X-ray fluorescence with total reflecting beam (TXRF) (Dixkens and Fissan, 1991). Hence, ESP can be combined with numerous analytical techniques to observe physical and chemical composition of aerosol particles.

ESPs for particle deposition commonly operate in two-stages (particle charging and particle collection) for higher control on deposition, and generally fall into two broad categories, a translationally symmetric design (linear system) or a radially symmetric design (radial system). In both systems the electric field is perpendicular to the fluid flow that is parallel to the collection surface. Additionally, in most radial design the fluid enters the collection region through a tube perpendicular to the collection surface, before moving radially outwards. A parallel plate linear ESP was proposed in 1974 for collecting aerosol particles on a substrate for subsequent analysis with IR spectroscopy (Harrick and Beckmann, 1974), and a point-to-plate linear ESP for similar application has been fabricated in 2009 (Ofner, Krüger, et al., 2009). An offline radial ESP for TXRF goes back to 1991 (Dixkens and Fissan, 1991) and was characterized further in 1999 (Dixkens and Fissan, 1999). Other radial ESPs have been used for TEM analysis (Fierz, 2007) and for functional film formation (Kala et al., 2012). Hence, many independent ESP collection devices have been developed. However, facile methods to facilitate designing for a certain design objective is rare.

Many mathematical models have been developed for industrially common, single stage point-to-plate ESP (Le, Lin, and C.-J. Tsai, 2013) or wire-to-plate ESP that assume a turbulent flow. The Deutsch equation for electrostatic collection efficiency in this setup and the corresponding Deutsch number (Deutsch, 1922) has been commonly used and numerous other similar models has been developed (Cooperman, 1971; Reynolds, Theodore, and Marino, 1975; Leonard, Mitchner, and Self, 1982; Zhibin and Guoquan, 1994), including some iterative solution models (Schmid, 2003; Podlinski et al., 2008), and some that explore the effect of poly-dispersed particles (Kim, Park, and K. Lee, 2001). These models mainly aim to predict removal efficiency in a turbulent flow with single stage charging and collection, and factor-in limited geometric parameters.

Analytical modeling of ESPs has been used to predict collection efficiencies or deposited area. For radial systems, a stagnation point flow (Peters, Cooper, and R. J. Miller, 1989) is a good approximation for the flow in the vicinity. Hence, stagnation point flow models (Adamcyzk, 1989; Fichman, Pnueli, and Gutfinger, 1990) used in conjunction with electrostatic
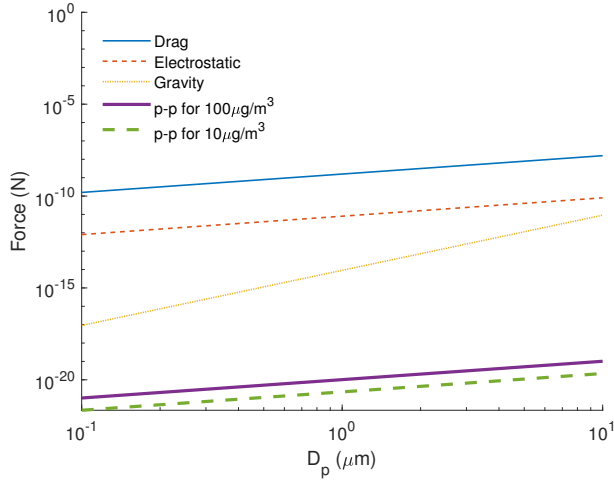
Figure 3.1: Comparison of order-of-magnitude of the relevant external forces acting on the particle at a flow Reynold's number (Re) of 1000. The forces are calculated for Stokes' drag ($F_D = \frac{3\pi\mu D_p(\mathbf{v}-\mathbf{u})}{C_c}$), electrostatic ($F_E = q\mathbf{E}_0$), gravity ($F_g = m_p\mathbf{g}$) and the particle-particle (p-p) electrostatic interaction force ($F_{p-p} = \frac{1}{4\pi\epsilon_0}\frac{q_1 q_2}{s^2}$). Here, v is the particle velocity, u is the fluid flow velocity, C_c is the Cunningham correction factor, q is the charge on the particle of size D_p that is in the presence of an electric filed E_0. For the p-p force, s is the distance between two particles calculated for different mass concentrations of ammonium sulfate, and $q_1 = q_2 = (5 * \frac{D_p}{100nm})e$ (5 elementary charge for every 100nm particle diameter) on the particles of a given size (x-axis).

force calculations can be used to assess particle collection (Peters, Cooper, and R. J. Miller, 1989),(Turner, Liguras, and Fissan, 1989; Cooper, Peters, and R. J. Miller, 1989). Recently, a predictive analytical model was created to predict the "spot size" of the deposition of mono-dispersed aerosol (Preger et al., 2020), assuming an infinitesimal inlet radius (IIR). However, these models do not explain the relationship between inlet particle position and final deposited position, which is necessary for when knowledge of deposition profiles are desired.

In this work, we derive a mechanistic, analytical model that captures the particle migration trajectories due to fluid dynamics and electrostatics of a two-stage ESP. Congruent to previous analysis (Fierz, 2007; Preger et al., 2020), we find the drag force and electrostatic force to be dominant forces (Figure 3.1). Thereafter, we derive a dimensionless form of the equation, where the dimensionless terms includes a wide range of design and operating parameters with respect to the characteristic size (L_c or R_c). We validate the particle collection predictions in this model against 718 numerical simulations using COMSOL Multiphysics software, which is considered to be accurate but can only be run for a limited number of configurations (with respect to geometry and operating parameters) due to its high computational cost. Each simulation is performed with a different combination of design geometry, operating parameters and inlet conditions. The resulting "finite inlet radius" (FIR) model is compared

38

against prior experiments, and analyzed to qualitatively assess device collection performance over a wide range of conditions, and outline ways to design a new device or fine-tune existing devices towards desired particle collection. We propose few new dimensionless numbers that are relevant to ESP system. FIR model opens a range of possibilities for new device design by exploring the interdependence of device geometry, operating conditions, particle property, and inlet conditions.

3.3   Method

In this Section, we describe the analytical model for a radial ESP (Section 3.3.1) and the method for numerically simulating reference solutions for evaluation (Section 3.3.2). The subject of our investigation is the collector (second stage) of a two-stage ESP. We consider actively charged particles arriving through an inlet of arbitrary size ("finite inlet radius" or FIR) which is applicable for examining devices that incorporate sheath flow, or lower inlet velocities to reduce instances of impaction or size dependence in particle collection. Cases for parabolic flow (fully-developed pipe flow; typical case) and plug flow (outlet of contracting nozzle) at the inlet are considered.

3.3.1   Analytical model derivation

3.3.1.1   FIR model for particle trajectory in a radial ESP

We model particle trajectories considering only the balance of drag and electrostatic forces (Hinds, 1999; Fierz, 2007; Preger et al., 2020) for the size and conditions (low Stokes number - St , high Péclet number - Pe, laminar flow) considered in this work. For laminar flow (Re < 1800) and large span of particle-size (1 nm < D_p < 1 μm), Pe ≫ 1 means that diffusion effects can be neglected (Appendix C.1, Figure C.1a) and St < 0.1 suggests that impaction effects can be neglected (Appendix C.1, Figure C.1b).

$$\mathbf{v}(\mathbf{X}) = \mathbf{u}(\mathbf{X}) + \mathbf{v}_{\text{elec}}(\mathbf{X}) \tag{3.1}$$

$$\mathbf{v}_{\text{elec}}(\mathbf{X}) = \frac{q\mathbf{E}_0(\mathbf{X})C_c}{3\pi\mu D_p} = Z_p\mathbf{E}_0(\mathbf{X}) \tag{3.2}$$

$$C_c = 1 + Kn\left[1.142 + 0.558\exp\left(-0.999/Kn\right)\right] \tag{3.3}$$

$\mathbf{X}$ is the spatial coordinate, C_c is the Cunningham correction factor, $q = ne$ is the charge on the particle (a product of the elementary charge and the number of elementary charges), and Z_p is the electrical mobility. Electrically-charged particle-particle interactions can be neglected at these concentrations.

The solution to equation 3.1 for a radially axisymmetric system is shown below. A similar solution for the linearly translational system (Appendix C.3) is used to explain the particle drift in the inlet tube. Linearly translational ESPs have also been suggested for particle collection,

but the radial system has inherently higher collection efficiency and smaller sensitivity to particle size (Section C.4) and will be the focus of this work.
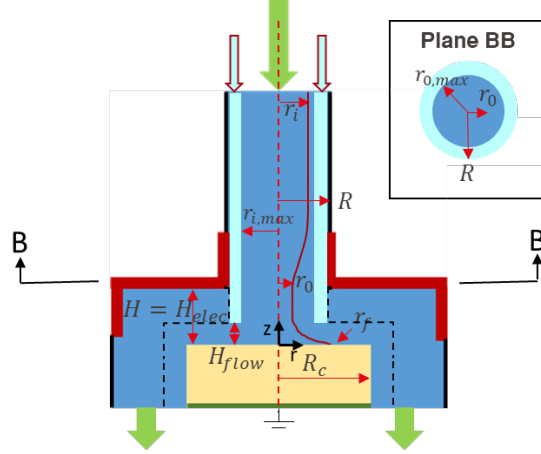
Figure 3.2: Basic schematic with geometric variables for a radial system.

The basic schematic of the radial system (Figure 3.2) has a characteristic length of R_c - e.g., characterizing collection surface size, though it can represent a region of interest (for example probe size or intended spot size for some applications). The fluid inlet is perpendicular to the surface through a tube with radius R, above the plane BB. Particle collection region is below the plane BB for the radial system, and we assume that in this region, the fluid flow is perpendicular to the electric field. The electric field is generated by using electrodes (at a voltage difference of V_0), separated by a distance H from the collection surface (at a voltage V_g).

The FIR model considers the region below the inlet and between the electrodes. The spatial coordinate $\mathbf{X} \equiv (\mathbf{r}, \mathbf{z})$ comprises radial and vertical directions. An analytical solution for $\mathbf{v}(\mathbf{X})$ is found by assuming the electrostatic field and the fluid velocity are perpendicular to each other: $\mathbf{E}_0(\mathbf{X}) = \mathbf{E}_0(\mathbf{z})$ and $\mathbf{u}(\mathbf{X}) = \mathbf{u}(\mathbf{r})$. The electric field largely acts in the $-ve$ z-direction, though the magnitude of this field varies for $r \leq R$ because of the noncontinuous electrode (absent in the cross-section of the tube) and its effect is considered in Section 3.3.1.2. The initial radial position of the particle in the inlet is translated into the vertical position in the ESP from the streamlines in stagnation point flow ($\mathbf{u} = ar\,\mathbf{r} - az\,\mathbf{z}$) where a is an arbitrary constant). For low flow Reynolds number ($\mathrm{Re}_{\mathrm{flow}} < 100$), $z_0 / H_{\mathrm{elec}} = r_0 / R$ where H_{elec} is the height of the high voltage electrode from the base of the collection surface. For higher $\mathrm{Re}_{\mathrm{flow}}$, $z_0 / H_{\mathrm{flow}} = r_0 / R$ where the effective height $H_{\mathrm{flow}} \leq H_{\mathrm{elec}}$ (Section C.1, Figure C.2). The particle trajectory $(r(t), z(t))$ is obtained from integrating $\mathbf{v}(\mathbf{X})$ (Appendix C.2).

Finally, for particle deposition analysis, the final position of the particle at $t \rightarrow \infty$, such that $z(\infty) = 0$, is of interest. Furthermore, by including the characteristic length R_c into the equations we formulate a basic dimensionless analytical model for predicting the final position of deposition (r_f / R_c), given the initial position in the tube (r_0 / R), the ratio of the

average fluid velocity in the inlet tube to the electrostatic migration velocity ($v_{\text{in}}/v_{\text{elec}}$), and the r-direction fluid velocity flow profile $\overline{f}_{vr}(r_0)$ (Appendix C.5). Equation 3.4 shows the dimensionless equation for the radial system and equation C.1 (Appendix C.3) shows a similar equation for the linear system. Equation 3.4 can be arranged into another dimensionless form (equation 3.5) that groups the operational parameters (Q and E) into a single term and the particle dependent variables (D_p, n and C_c) into another, where n is the number of elementary charges on a particle of diameter D_p, and e is the charge on a single electron.

$$\left(\frac{r_f}{R_c}\right) = \left(\frac{r_0}{R}\right)\left(\frac{R}{R_c}\right)\sqrt{1+\left(\frac{v_{\text{in}}}{v_{\text{elec}}}\right)\left(\frac{r_0}{R}\right)^{-1}\overline{f}_{vr}(r_0)} \tag{3.4}$$

$$= \sqrt{\left(\frac{r_0}{R}\frac{R}{R_c}\right)^2 + 3\left(\frac{Q\mu}{eE_0 R_c}\right)\left(\frac{D_p}{nC_c R_c}\right)\left(\frac{r_0}{R}\right)\overline{f}_{vr}(r_0)} \tag{3.5}$$

where

$$\overline{f}_{vr}(r_0) = \begin{cases} r_0/R & \text{plug-flow inlet} \\ (r_0/R)(2-(r_0/R)^2) & \text{parabolic-flow inlet} \end{cases}$$

A more general case involves sheath flow into the radial system. The sheath flow restricts the outermost position of the particle in the inlet tube to $r_i = r_{i,\max}$, and the annular sheath flow takes up $r_{i,\max}$ to R. The geometric proportion of aerosol to total flow comprising the radius is characterized by $r_{lim}^* = r_{i,\max}/R$, which spans between 0 and 1. The total flow rate (Q) now includes both particle laden aerosol flow (Q_a) and the sheath flow (Q_s) such that for plug-flow inlet $Q_a = Q{r_{lim}^*}^2$, and for parabolic-inlet $Q_a = Q{r_{lim}^*}^2(2-{r_{lim}^*}^2)$. Equation 3.6 shows the finite-inlet-radius (FIR)-model with a handful of dimensionless terms for a general case that includes sheath flow. The effect of drift in the inlet tube is represented by $\Omega = r_0^*/r_i^*$, where r_0^* is the dimensionless position of a particle post-drift in the inlet tube, at the entrance of the collection region, and $r_i^* = r_i/R$ is the dimensionless position of the particle pre-drift at the tube inlet. As calculated later in equation 3.10, the drift factor Ω is not only a function of α, β, R/R_c but also H/R, making it the sole term affected by it in the equation, as discussed in Section 3.3.1.2.

$$\left(\frac{r_f}{R_c}\right) = \begin{cases} \Omega\left(\frac{r_i^*}{r_{lim}^*}\right)\sqrt{{r_{geo}^\dagger}^2 + 3\alpha\beta} & \text{plug-flow inlet} \\ \Omega\left(\frac{r_i^*}{r_{lim}^*}\right)\sqrt{{r_{geo}^\dagger}^2 + 3\alpha\beta\left(\frac{2-\Omega^2 {r_i^*}^2}{2-{r_{lim}^*}^2}\right)} & \text{parabolic-flow inlet} \end{cases} \tag{3.6}$$

where

$$\Omega = f\left(r_i^*, \frac{H}{R}, \frac{R}{R_c}, \alpha, \beta\right); \quad r_{geo}^\dagger = \left(r_{lim}^* \frac{R}{R_c}\right); \quad r_0^* = \frac{r_0}{R}; \quad r_{lim}^* = \frac{r_{i,\max}}{R}; \quad \alpha = \frac{Q_a\mu}{eE_0 R_c}; \quad \beta = \frac{D_p}{nC_c R_c}$$

Chapter 3. Design of an electrostatic aerosol collector part 1: dimensionless analytical model for mapping inlet particle positions to collection surface

In this work, we adopt the convention denoting radial positions of particles scaled to the inlet diameter by $\{\}^*$ and those scaled to the characteristic length by $\{\}^\dagger$. β can further be written as a function of the electrical mobility (eq. 3.2).

$$\beta = \frac{e}{3\pi\mu Z_p R_c} \tag{3.7}$$

These parameters are further discussed in Section 3.3.1.3.

3.3.1.2 Electric field at entrance of tube and drift correction

A finite radius device introduces a hole from $r = 0$ to $r = R$ in the top electrode, which imparts an electrostatic force of particles in the inlet tube, and also leads to nonuniform electric fields below the tube. The configuration of the geometry causes particles to drift toward the central axis, as illustrated in Figure 3.2 where the particle enters the tube at a position r_i but drifts inwards towards the center until r_0, before entering the collection region. We approximate the electric field inside the tube by assuming a ring of charge with radius R on the plane AA. Off-axis electric field of a charged ring (Zypman, 2006) is applied to the radial system here (equation 3.8). Furthermore, in order to eliminate the need to estimate the charge on the ring (q_{ring}), we use the boundary condition $E_0 = \sqrt{E_r^2 + E_z^2}$ at $r/R = 1$ and $z/R = 0$, i.e. at the point on collection surface just below the ring. z-direction electric field (E_z/E_0) changes with H/R (Figure 3.3). The dependence on H/R is very strong and is especially sensitive to r/R at lower H/R.

$$E_r = k \left\{ \frac{\xi\sin\theta}{\left(1+\xi^2\right)^{3/2}} \frac{\pi - \frac{2(\pi-\sqrt{2})\xi}{1+\xi^2}\sin\theta}{1 - \frac{2\xi}{1+\xi^2}\sin\theta} - \frac{1}{\left(1+\xi^2\right)^{3/2}} \frac{\frac{2\sqrt{2}\xi}{1+\xi^2}\sin\theta}{1 - \frac{2\xi}{1+\xi^2}\sin\theta} \right\} \tag{3.8a}$$

$$E_z = k \left\{ \frac{\xi\cos\theta}{\left(1+\xi^2\right)^{3/2}} \frac{\pi - \frac{2(\pi-\sqrt{2})\xi}{1+\xi^2}\sin\theta}{1 - \frac{2\xi}{1+\xi^2}\sin\theta} \right\} \tag{3.8b}$$

where

$$k = \frac{1}{4\pi\epsilon_0} \frac{q_{\text{ring}}}{\pi R^2}; \quad \xi = \sqrt{\left(\frac{r}{R}\right)^2 + \left(\frac{z}{R} - \frac{H}{R}\right)^2}; \quad \theta = \arctan\left(\frac{r/R}{z/R - H/R}\right)$$

Particle drift in the inlet tube is approximated using the particle collection equation C.1 of a linear system because the average fluid velocity is a constant (moving in $-ve$ z-direction) and the electrical field that causes the migration is perpendicular to the flow (in $-ve$ r-direction), as illustrated in Figure 3.4. One key difference is that the velocity flow profile is neither plug-flow like, nor parabolic in the collection region which is bound by the points $(r_i, H + L_c)$ and (r_0, H) (Figure 3.4). Using these chosen bounds, the linear system equation C.1 is applied to the drift in the tube by using $x_f/L_c = 1$, $z_0/H = 1$, $H = r_i - r_0$, $L_c = R$ (length scale of drift), and
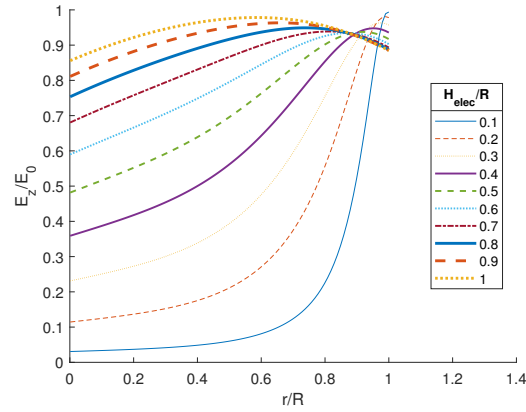
Figure 3.3: Change in the normalized z-direction electric field E_z/E_0 under the tube at the collection surface ($z/H =0$) for different values of H/R.
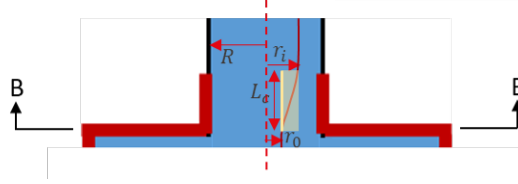
Figure 3.4: Illustration of the region modeled as a linear ESP system (yellow rectangle) to calculate particle drift in the inlet tube of a radial system.

$\overline{f}_{vx}(z_0) = \overline{f}_{vz}(r_i)$, where, $\overline{f}_{vz}(r_i)$ is the flow profile function applicable to the linear system when adapted from the flow profile in the inlet tube (equation 3.9, derived in Appendix C.5).

$$\overline{f}_{vz}(r_i) = \begin{cases} 1 & \text{plug-flow inlet} \\ 2 - \frac{2}{3}\frac{r_i^{*3} - r_0^{*3}}{r_i^* - r_0^*} & \text{parabolic-flow inlet} \end{cases} \tag{3.9}$$

The resulting equation that calculated the post-drift position, r_0, is linear for plug-flow inlet and a cubic polynomial solvable for r_0/R for a parabolic-flow inlet (equation 3.10).

$$\begin{cases} \Omega = 1 - \frac{1}{r_i^*}\left(1 + \frac{v_{\text{in}}}{v_{\text{elec},r}}\right)^{-1} & \text{plug-flow inlet} \\ \Omega^3 = \frac{3}{r_i^{*2}}\left(1 + \frac{v_{\text{elec},r}}{2v_{\text{in}}}\right)\Omega - \left[1 - \frac{3}{r_i^{*2}}\left(1 + \frac{v_{\text{elec},r}}{2v_{\text{in}}}\right) + \frac{3}{r_i^{*3}}\left(\frac{v_{\text{elec},r}}{2v_{\text{in}}}\right)\right] = 0 & \text{parabolic-flow inlet} \end{cases} \tag{3.10}$$

where

$$\frac{v_{\text{in}}}{v_{\text{elec},r}} = \begin{cases} \frac{1}{E_{\text{corr}}}\frac{3\alpha\beta}{r_{lim}^{*2}}\left(\frac{R}{R_c}\right)^{-2} & \text{plug-flow inlet} \\ \frac{1}{E_{\text{corr}}}\frac{3\alpha\beta}{r_{lim}^{*2}(2 - r_{lim}^{*2})}\left(\frac{R}{R_c}\right)^{-2} & \text{parabolic-flow inlet} \end{cases}$$

Here, $E_{\text{corr}} = E_{r,\text{avg}}/E_0$ is the correction factor for average radial electric field strength ($E_{r,\text{avg}}$)

for $r < r_i$ at a height R away from the ring plane, derived using the off-axis electric field equation 3.8a. As $E_{r,\text{avg}}$ is dependent on H/R, the drift factor becomes dependent on it.

The nonuniformity in the E_z below the ring increase with low H/R, and this feature is qualitatively reproduced using the ring charge equation (Figure 3.3). However, incorporating the effect of this nonuniformity on particle trajectories in the simple analytical model of eq 3.6 is nontrivial, as each particle experiences a changing electric field as it moves across r and z. While assuming a constant electric field E_0 imparts some errors on the final location of deposition r_f^*, no approximation of the electric field performed systematically better in its prediction. However, the magnitude of nonuniformity in the electric field was indicative of the nonuniformity in deposition that was not modeled by FIR, and is used to make corrections in our nonuniformity estimate. The magnitude of these errors and the correction is detailed in Section 3.4.1.2.

3.3.1.3 New dimensionless terms and equivalencies in the FIR-model

The FIR model (equation 3.6) can be thought of as a mapping from the position in the inlet, $r_i^* = r_i/R$ to the collection surface $r_f^\dagger = r_f/R_c$ for different geometries ($r_{geo}^\dagger$, H/R), operating conditions (α), particle properties (β) and sheath conditions (r_{lim}^*). It hence allows analyzing the effect of not only these parameters on collection performance but also that of inlet particle concentration distribution. The dimensionless terms are separated with the idea of preserving terms that are aimed to be held a constant. For example, α is parameterized by Q_a rather than Q for assessing particle collection dynamics (e.g., mass flux) directly; the relation to Q is encompassed in r_{lim}^*.

The dimensionless numbers α and β are the ESP operation number and the ESP particle number, respectively, $r_{geo}^\dagger$ is the radial ESP inlet number and $r_{f,\text{max}}^\dagger$ is the ESP performance number. All these four parameters scale with the characteristic size R_c; hence, the FIR model is scalable. For instance, the outermost particle in the inlet, $r_{i,\text{max}}^* = r_i/R$ drifts to the outermost position at the end of the tube and deposits on the surface at the outermost position, $r_{f,\text{max}}^\dagger = r_{f,\text{max}}/R_c$. The 4 dimensionless terms have a physical significance for design and are explained further below.

The ESP inlet number $r_{geo}^\dagger$ is the apparent tube inlet radius, as it represents the position of the outermost particle at the inlet since $R_c r_{geo}^\dagger = R r_{lim}^* = r_{i,\text{max}}$.

The ESP operation number α, includes the operating variables Q_a and E_0. As eE_0 is the electrostatic force on an electron and R_c is the length scale of collection, eE_0R_c is related to the performed work. $Q\mu$ is representative of the energy associated with the fluid flow and related to the Hagen–Poiseuille equation as $Q\mu = (\Delta p \pi R_H^2 L/8)(R_H^2/L^2) \propto W_{\text{flow}}(H^2/R_c^2)$, where W_{flow} is related to the work performed by the moving fluid over length scale R_c and hydraulic radius H. Moreover, for a fixed E_0, α is related to Re_{flow}, as $\alpha \propto Re(Q_a/Q)(R/R_c)$ (Figure 3.5a). For lower r_{lim}^*, $Q_a/Q < 1$ the plotted α values are upper limits for a given R/R_c

and Re at fixed E_0. The values scale inversely with E_0, which can be expected to scale by a single order-of-magnitude in either direction, hence, an estimated range of common α emerges as $\alpha \approx 10^4$ to 10^8.

The ESP particle number β includes all the terms dependent on particle size and is the ratio of slip corrected particle diameter (D_p/C_c) to R_c and the number of elementary charges on the given particle, n. If the amount of charge on a particle strictly scales proportionally to its diameter, the size dependence of particle migration would result solely from C_c — which ranges over orders of magnitude for particle sizes between 100 nm and 1 μm — since D_p/n is present in a single term. However, considering that a distribution of charges can be found across particles of a particular size, size dependence explored with this model through β can be better interpreted as an electrical mobility dependence (equation 4.1). The range of values of β changes with R_c values in addition to electrical mobility (Figure 3.5b). The estimated range of β is estimated to be approximately 10^{-8} to 10^{-3} if we consider a single elementary charge on a particle as the lower bound (though we expect the charge number n to be typically higher especially for larger particles - or smaller Z_p).

The ESP performance number $r^\dagger_{f,\max}$ is the outermost final position of the particle on the collection disc. The larger this value, the more spread out the deposition area, thus, resulting in lower collection efficiency. If the final spatial deposition is uniform, then the collection efficiency is $\eta = (\pi R_c^2)/(\pi r^2_{f,max}) = (r^\dagger_{f,\max})^{-2}$ for $r^\dagger_{f,\max} \geq 1$ (and $\eta = 1$ otherwise). For other spatial distributions of the final particle deposition on the collection surface, efficiency can be calculated empirically — nonetheless, deviation of $r^\dagger_{f,\max}$ from unity can provide qualitative indication of the deposition area to the collector area. The other dimensionless terms also have a defined range: $0 < r^*_{lim} \leq 1$; $0 < \Omega \leq 1$; $0 < r^*_i/r^*_{lim} \leq 1$; and $1 \leq (2 - \Omega r^{*2}_i)/(2 - r^{*2}_{lim}) \leq 2$.

(a)   (b)
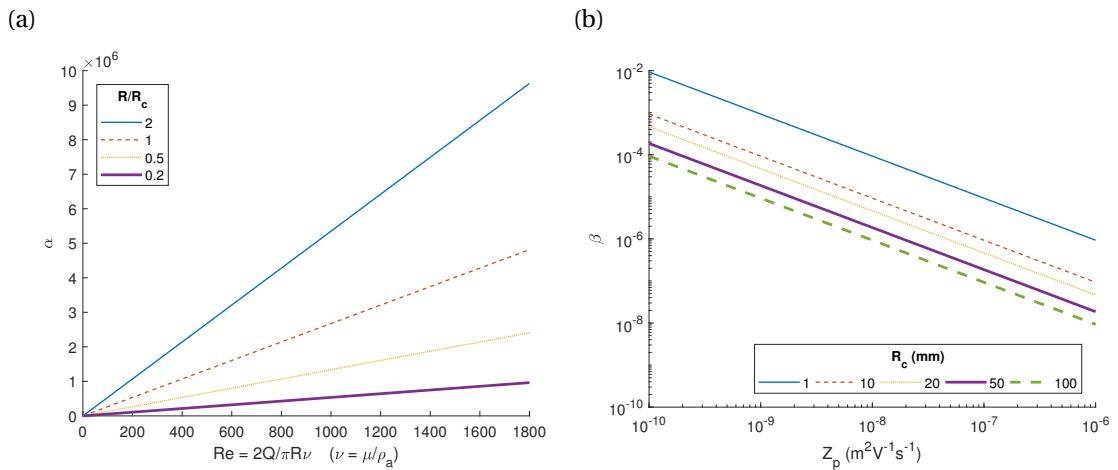
Figure 3.5: Range of (a) α for $r^*_{lim} = 1$ and $E_0 = 1$ kV/mm and various flow Re and R/R_c, and (b) β for different Z_p and R_c.

Some equivalencies can already be inferred from the analytical form of the FIR-model. Drift in

the inlet tube causes particles to be collected over a smaller area than they would have without any drift (as $\Omega < 1$). As $\alpha\beta$ is present as a single term in the model, the operational and particle properties have compensating effects — increasing β by a factor and decreasing α the same factor will not affect collection. The collection performance is not directly proportional to the operation number, particle number, or the inlet number. However, for the ESP operation number, as Q_a/E is present in a single term, doubling the electric field strength and the aerosol flow rate simultaneously would result in the same aerosol collection performance. The term is also present in the drift factor Ω (equation 3.10), making the statement applicable to the entire FIR model.

3.3.2 Numerical Simulations

We performed particle collection simulations in a radial ESP system using a 2D-axisymmetric model in COMSOL Multiphysics 5.2a software. A device geometry similar to radial ESP (Figure 3.2) was built using variable input parameters, such as characteristic length, R_c, and dimensionless ratios R/R_c, H/R, r_{lim}^*. The radius of the collection surface was set to a value higher than R_c to allow particle collection till $r > \max(R_c, R)$, and to reduce fringe effects from the collection surface edges. An extremely-fine physics-controlled mesh was used to run a steady-state study for laminar flow and electrostatics, and a time-dependent study for particle tracing using the steady-state fields with a relative tolerance of 10^{-3} and 10^{-5}, respectively. Laminar flow was setup with a laminar inflow of the set flow rate Q and a 1 atm pressure outlet. Large-scale eddies at the either side of the tube outlet (above the main radially outward flows) were resolved with mesh refinement to circumvent the use of stochastic turbulent parameterizations (Appendix C.7, Figure C.1).

Electrostatics were set up using high voltage on the top-electrodes and a ground voltage, V_{grnd}, on the top surface of the collection substrate, such that the voltage difference between the top-electrodes and collection surface was V_0. V_0 was internally calculated in the simulation using the set electrostatic field strength E_0 and the separation height H. Particle tracing simulation was performed with one thousand particles being released from the top of the inlet tube, uniformly distributed between $0 < r/R < r_{lim}^*$, with the particles freezing on boundaries upon contact. Uniformly distributed particles at the inlet has previously been assumed in other works, (Preger et al., 2020), (Gomes et al., 1993). Particle tracing calculations used Stokes drag force and electric force, where the particle property was defined with charge on the particle n, the slip corrected particle diameter D_p/C_c, and the particle mass density ρ_p. Five elementary charges for every 100 nm increase in particle diameter ($n = D_p/[20\text{nm}]$) from kinetically-limited diffusion charging was assumed (Biskos, Reavell, and Collings, 2005) (the expected charge is higher for larger particles for a combination of field and diffusion charging (Marquard, 2007; Kaminski et al., 2012)). Figure 3.6a shows the fluid streamlines, electrostatic field direction (arrows), and the magnitude of the electrostatic field in the z-direction (surface plot); and Figure 3.6b shows the fluid streamlines and the particle trajectory (colored by the particle velocity at that point). In the end we compare and use 718 COMSOL simulations as

some of the combination of variables did not result in a converging solution, possibly because of the solver not being able to resolve some larger eddies for specific geometry or flow rates.

(a)   (b)
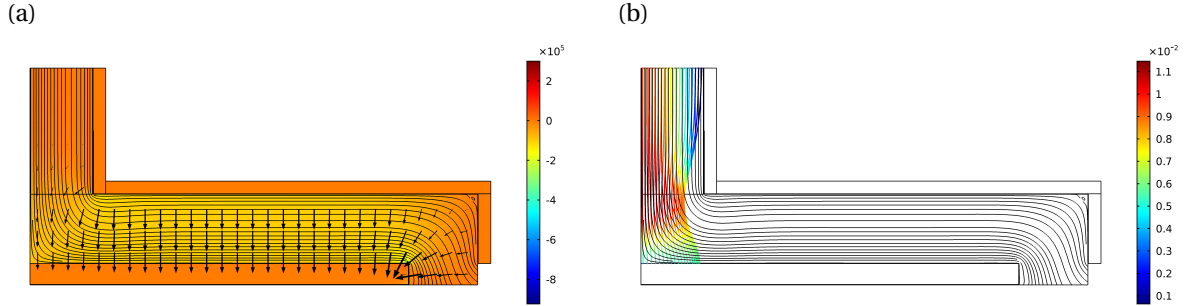
Figure 3.6: COMSOL simulation example result of (a) steady-state simulation for velocity field (black arrows), voltage (color-bar) and electrostatic field (red arrows), and (b) time-dependent simulation for particle tracing (colored trajectory lines) in fluid flow with the steady-state velocity streamlines (black) and particle velocity (color-bar).

3.4   Results and discussion

In this section, the change in electric field under the inlet tube and the drift equation for Ω is discussed in Section 3.3.1.2. We present the comparison of model calculations against COMSOL Multiphysics simulations (in Section 3.4.1) and against previous experiments by various authors (in Section 3.4.2). Details of the new dimensionless numbers of the verified FIR model (Section 3.4.4), along with a 2D-plot that is useful in representing broad ESP designs.

The value of E_z/E_0 at $z/H = 0$ and the average values matches those from COMSOL simulations (Appendix C.7, Figure C.3) along with the functional dependence which is also in general agreement.

3.4.1   Evaluation against numerical simulations

In this section, we compare FIR model outcomes to extensive COMSOL Multiphysics simulations. Firstly, we compare the position of only the outermost particle out of the 1000 particles simulated (Section 3.4.1.1). Thereafter, we evaluate spatial deposition profiles against different hypothetical flow and particle distributions combinations at the tube inlet (Section 3.4.3).

3.4.1.1   Spot size

The spot size of deposition is determined by the outermost final position of the particles ($r_{f,\max}^{\dagger}$). If drift is excluded, $\Omega = 1$ and the outermost particle position would remain the same in the inlet tube ($r_{0,\max}^{*} = r_{i,\max}^{*} = r_{lim}^{*}$). For this hypothetical case, equation 3.6 for both

parabolic-flow and plug-flow cases would reduce to the no-drift equation 3.11, which largely overestimates $r_{f,\max}^{\dagger}$ (Figure C.3).

$$r_{f,\max}^{\dagger} = \sqrt{r_{geo}^{\dagger}{}^2 + 3\alpha\beta} \qquad (3.11)$$

Furthermore, with increasingly small inlet radius and no sheath flow ($R \rightarrow 0$, $r_{geo}^{\dagger} = 0$ and $r_{lim}^{*} = 1$), the spot size estimate of FIR becomes identical to that calculated by the infinitessimal inlet radius (which we refer to as IIR) model of (Preger et al., 2020): $r_{f,\max}^{\dagger} = \sqrt{Q/\pi v_{\mathrm{elec}}}$. Particle drift in the inlet moves the particles closer to the center, extending the applicability of the IIR approximation. However, modeling the finite radius and incorporating drift correction becomes important to reduce prediction errors in devices with increasingly large $r_{geo}^{\dagger}$ (Figure C.3).

$r_{f,\max}^{\dagger}$ from the full FIR model including drift correction (starting from inlet position $r_i^{*} = r_{i,\max}^{*}$) is compared against the position of the outermost particle from 1000 particles released in each particle-tracing study in COMSOL over various different geometries, inlet/ operating condition and particle properties; for the parabolic-flow-inlet (Figure 3.7a) and for the plug-flow inlet (Figure 3.8a). Points from the (Preger et al., 2020)-model which fall within 5% deviation of the FIR-model calculations are also included for reference.

(a)   (b)
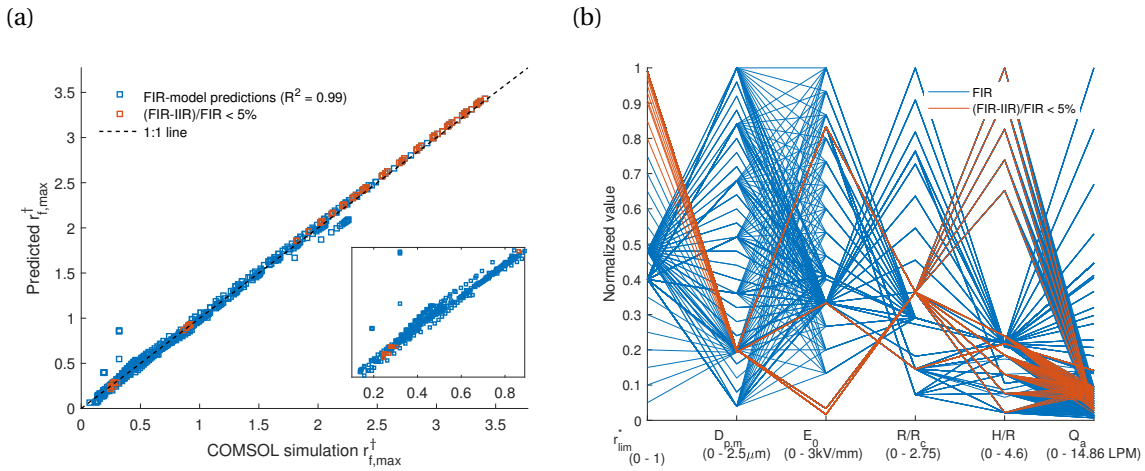
Figure 3.7: Comparison of the FIR model calculations against 718 COMSOL simulations with varied geometry, operating condition, sheath position, and particle sizes for parabolic-flow velocity profile at the tube inlet of a radial ESP system. (a) Comparison of the final position of outermost particle from FIR, $r_{f,\max}^{\dagger}$ (blue and orange) and points from IIR (orange) which are within 5% deviation, and (b) the range of parameters for the simulations in (a) and the colors corresponding to (a). *IIR-model: (Preger et al., 2020)

Figure 3.7a shows the model-calculation comparison for the more likely parabolic-flow inlet. To make a better comparison, we use a large range of input variables in our simulations (Figure

(a)

(b)
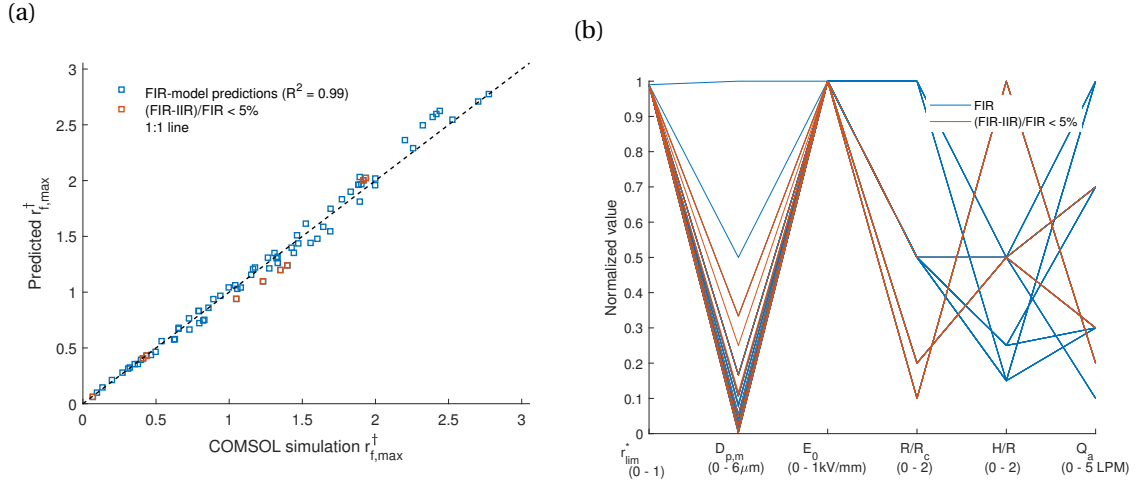
Figure 3.8: Comparison of the FIR model calculation against 77 COMSOL simulations with varied geometry, operating condition, sheath position, and particle sizes for plug-flow velocity profile at the tube inlet of a radial ESP system. (a) Comparison of the final position of outermost particle $r^{\dagger}_{f,\max}$, and (b) the range of parameters. *IIR-model: (Preger et al., 2020)

3.7b) where each simulation is a line connecting the different set of variables. For aerosol applications, a size range of $D_p < 2.5\mu$ m is relevant and n expansive range of Q and E_0 is simulated to assess the performance of the model. All simulations showed a high electric field concentration at the edge of the collection surface, to nearly 2 times to 10 times the set value, as evident from the color bar limits in Figure 3.6a that represent the z-direction electric field. Hence, mostly $E_0 \leq 3$ kV/mm was simulated, considering the theoretical breakdown voltage of air. The plot insert in Figure 3.7a highlights the particle deposition calculation for $r^{\dagger}_f < 1$, as particle collection inside the characteristic length is likely to be of higher interest. Small variations are noticeable in the FIR-model calculations, mainly because of large changes in H/R (few over-predicted calculations between $0.4 < r^{\dagger}_f < 0.5$) and R/R_c (few under-predictions between $2 < r^{\dagger}_f < 2.5$). This is mainly because the z-direction electric field in the collection region is not a constant (Figure 3.6a), as is assumed in the FIR-model calculations. The extent of variation of this electric field is dependent on the R/R_c and H/R ratios (Figure 3.3) congruent with the off-axis electric field equation 3.8. However, as the electric field strength is very near E_0 for all points $r^* > 1$, including this discontinuous variation of E_0 would most probably require an iterative-numerical-model with piece-wise application of the analytical model. This process would become complex, dependent on the number of iterations and highly dependent on the assumption of the electric field distribution $E(r, z)$. This could be possible with a separate future study of the electric field in the particular geometry and the numerical simulation method. E_z from equation 3.8 could in principle be used to derive a first-order approximation. However, as each particle travels both vertically and radially - from different initial heights z_0 - through the changing electric field, no suitable expression for an effective, constant electric field strength has been found. Nonetheless, using average

49

electric field strengths for both drift calculation (average radial electric field for $r < r_i$, Section 3.3.1.2) and for particle collection, results in reproduction of the outermost-final-position of the simulations, allowing facile calculations of particle collection performance for different devices and conditions.

Few simulations for the plug-flow inlet are also compared against FIR-model calculations in Figure 3.8a, to assess whether the functional form of $\overline{f}_{vr}(r_0)$ accounts for the resulting changes, as it is the only term that changes for different flow profiles. As the number of independent variables are large, the 77 simulations were mainly varied in geometry, R/R_c and H/R, while some other parameters covered a smaller range of values (Figure 3.8b).

FIR model is useful in evaluating the particle collection performance in a radial ESP system for both plug-flow inlet and parabolic-flow inlet. Furthermore, as the drift calculation (equation 3.10) is done using the linear system equation C.1, both linear and radial ESP models are useful in particle trajectory evaluation.

3.4.1.2 Depositied positions and spatial uniformity

The FIR model is additionally applicable to the points inside the inlet tube ($r/R < 1$). The $r_f^\dagger$ of all particles in the numerical simulations described above $r_i^* \leq r_{lim}^*$ are compared to predictions from the analytical model generated from the same starting inlet positions (for a total of 718×1000 points, Figure 3.9a). 72% of the points are within $\pm 10\%$ of the FIR prediction (with $< 10\%$ of the points being underestimated), where the % is with respect to R_c and is calculated as $r_{f\,\text{FIR}}^\dagger - r_{f\,\text{COMSOL}}^\dagger$. The 28% deviating points are predominant for very low H/R ($H/R < 0.3$) and inner points ($r_i^* < 0.3$) (Figure C.3), and for high $\alpha\beta$ ($\log \alpha\beta > -0.5$) (Appendix C.6 Figure 3.10). Nearly, 62% of the points have deviations higher than 10% for $\log \alpha\beta > -0.3$ and $H/R < 0.3$ (Figure C.1). The deviations are largely attributed to the radial dependence of the electric field under the inlet tube $z/H < 1$ (Section 3.3.1.2), which is not included in the FIR-model. Therefore, the prediction errors are greatest near $r_f^* = 1$ (i.e. just under R) since they characterize situations when the actual electric field (as simulated by COMSOL) deviates most strongly from the modeled field (as assumed by FIR), and when the electrical migration velocity is much greater than the fluid velocity transporting the particles. There relation of the magnitude of the deviation with the values of r_i^* (Figure C.3a) is not monotonic and is higher for values of $r_i^* \approx 0.2$, which is possibly because of the higher velocity of the particles near this region at the start of the radial flow.

Despite the prominence of the deviation being restricted to only the inner particles for values of H/R and $\log \alpha\beta$, we evaluate its effect on spatial uniformity, an important property in many applications. Patterns of nonuniformity are further discussed in Section 3.4.3, but we evaluate metrics for characterizing this property below. The spatial uniformity for COMSOL simulations is calculated as the normalized median absolute deviation (NMAD$\{x_i\}$ = median$\{|x_i - \tilde{x}|\}/\tilde{x}$ where $\tilde{x}$ = median$\{x_i\}$) of separation distances between neighboring parti-

(a)

(b)
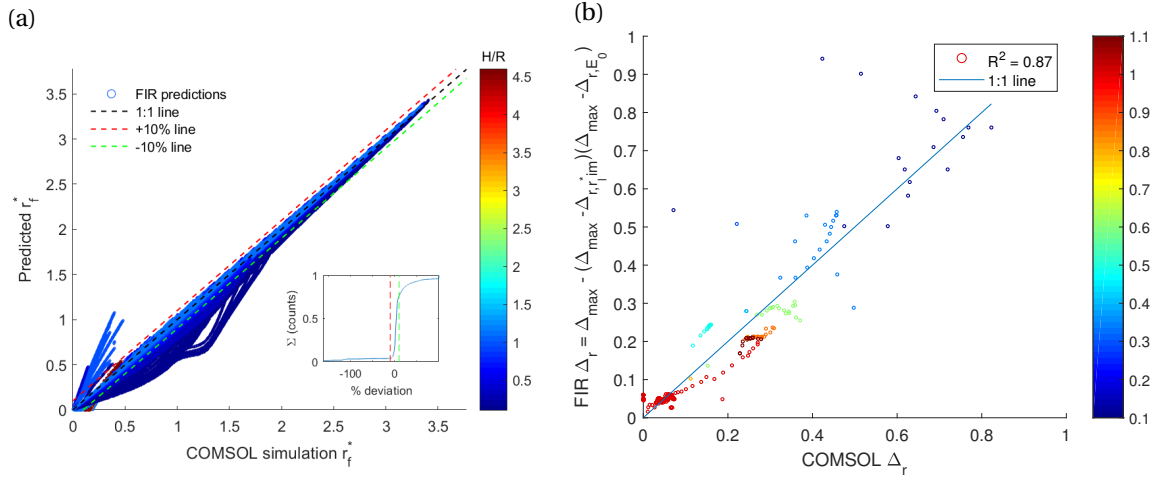
Figure 3.9: Comparison of the FIR-model calculation against 1000 inlet particles for each of the 718 COMSOL simulations in Figure 3.7. (a) Comparison of the final position of all the particles $r_f^\dagger$. The insert plot shows the cumulative fraction of points against deviation in prediction with reference lines at $+10\%$ and -10% deviation, within which 72% of the points lie. (b) Comparison of the reconstructed spatial non-uniformity (FIR Δ_r) against observed COMSOL non-uniformity.
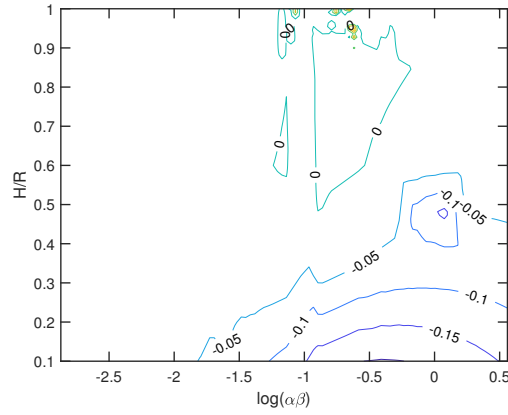
Figure 3.10: Contour plot of the deviation (measured as $\Delta r_f^\dagger = r_{f\,\mathrm{FIR}}^\dagger - r_{f\,\mathrm{COMSOL}}^\dagger$) for different $H/R < 1$ and $\log(\alpha\beta)$ values, formed using. The details of the distribution of the points used for calculating the plot is included in Appendix C.6 Figure C.2b.

cles.

$$\Delta_r = \mathrm{NMAD}\left\{r_{f,i}^\dagger - r_{f,i-1}^\dagger\right\} \tag{3.12}$$

Spatial nonuniformity is generally underestimated by FIR due to variations in the electrical field ($E_z(r,z)$ for $z/H < 1$ and $r/R < 1$), which are not considered by the model. A scale of overall nonuniformity is thus estimated from the nonuniformity in particle deposition

due to changing r_{lim}^* from the FIR model, Δ_{r,r_{lim}^*} (calculated using equation 3.12), and the nonuniformity in the electric field distribution over the collection surface Δ_{r,E_0} (deviation of the electric field from its median value over the region of deposition):

$$\Delta_{r,E_0} = \text{NMAD} \begin{cases} E_z(r_i, 0)/E_0 & \text{for } r_i \leq \min\{R, R_c r_{f,\max}^\dagger\} \\ 1 & \text{otherwise} \end{cases} \qquad (3.13)$$

E_z is taken from equation 3.8b for $z/H = 0$. The uniformity measure for a corresponding nonuniformity Δ_r is $[(\Delta_{max} - \Delta_r)/\Delta_{max}]$. Most statistical distributions have NMADs lower than 1 (Arachchige, Prendergast, and Staudte, 2020). We estimated a maximum value $\Delta_{max} = 1$ over a large range of shape parameters in a two-parameter Weibull distribution (Figure C.5). Thus, the overall nonuniformity was calculated from the product of apparent uniformity in deposition $1 - \Delta_{r,r_{lim}^*}$ and uniformity in electrical field $1 - \Delta_{r,E_0}$, as $\Delta_{r,FIR} = 1 - (1 - \Delta_{r,r_{lim}^*})(1 - \Delta_{r,E_0})$. The measure of nonuniformity from COMSOL can be estimated from the combined corrected measure defined FIR (Figure 3.9b).

3.4.2 Evaluation against previous devices

In addition to comparing the FIR model against computational numerical simulations, we also apply the model to published experimental results from previous device designs (Figure 3.11).

The TEM sampler by (Fierz, 2007) has a parabolic-flow inlet with $R_c = 1.5$ mm, $R/R_c = 1.33$, $r_{lim}^* = 1$, $H/R = 4.25$, $Q = 0.5$ LPM, $E_0 \approx 0.857$ kV/mm (based on -3 kV applied at the electrodes and a closest approach of 3.5 mm between two conducting electrodes). Using the charges measured by the authors, we determine drift corrected $r_{f,\max}^\dagger$ in the device and calculate the collection efficiency (Figure 3.11a). For reference, we also plot the predicted efficiency when we assume a fixed charge-to-diameter ratio, which can generally be estimated based on the charging method or design. Here we used $n = 2 * (D_p(\text{nm})/100)$ (instead of the values we mentioned previously) based on the measured charge on 50 nm particle for the experiments by the authors for the device. For efficiency calculation we assume a spatially uniform final deposition because for these high $r_f^\dagger$ values (corresponding to efficiency, $\eta \approx 5\%$), the applicable "inverse-parabolic" profile (1st row in Figure 3.12) can be approximated as a constant over R_c. The ESP collection device by (Preger et al., 2020) has a parabolic-flow inlet with $R_c = 50$ mm, $R/R_c = 0.02$, $r_{lim}^* = 1$, $H/R = 7.5$, and the other variables were provided as $\sqrt{Q/v_{\text{elec}}}$ by the authors in supplementary material. Using the information, we calculated the drift corrected final deposition position of the outermost particles and compared it against the experiments (Figure 3.11b). In the radial ESP by (Dixkens and Fissan, 1999) the distance of the inlet tube to the collection surface is very high and at the operating flow rate of $Q = 0.3$ LPM, the free jet expansion changes the apparent R/R_c for different particle sizes. As this physics is not included in the FIR model, some discrepancy is expected. The experiments performed by the authors (as reported in the Figure 7 of the publication) shows the collection

(a)

(b)

(c)

(d)
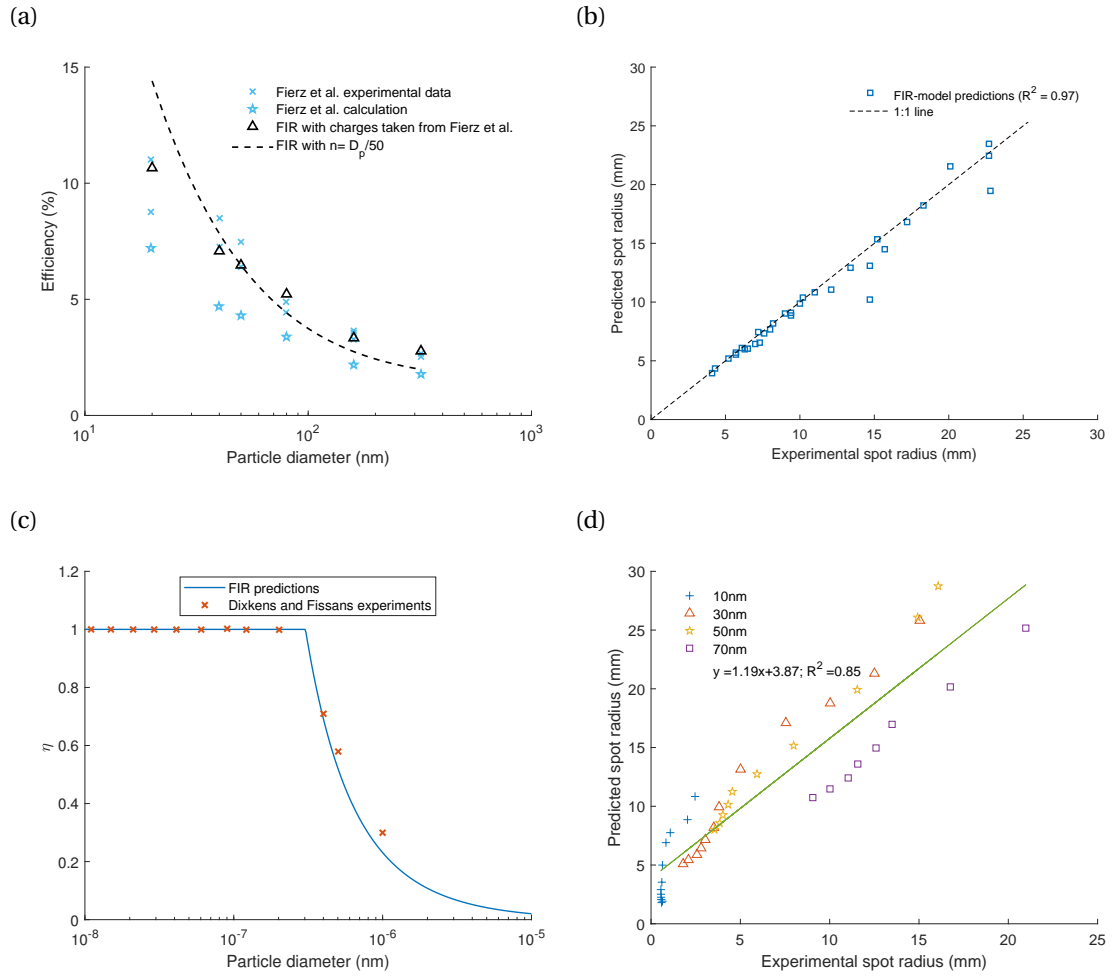
Figure 3.11: Predicting final deposition of particle in experiments of previous publications. (a) Collection efficiency prediction for TEM sampler (Fierz, 2007), (b) collection spot radius prediction for radial ESP (Preger et al., 2020), (c) collection efficiency predictions for radial ESP (Dixkens and Fissan, 1999), and (d) collection spot radius prediction for a different radial system (Kala et al., 2012).

efficiency for singly-charged particles, as predicted by the FIR model in Figure 3.11c. As the cylindrical housing (with radius $R_{ESP} = 42$ mm) is grounded, the applied voltage ($V_0 = 25$ kV) at the base electrode contributes to a much higher electric field at the edges of the collector surface ($R_c = 21$ mm). We estimate this using $E_0 = V_0/(R_{ESP} - R_c)$. and for the inlet, $r^*_{lim} = 1$ and $R/R_c = 0.14$.

Moreover, we attempt to apply the FIR model to a device by (Kala et al., 2012) ($R_c = 25$ mm), which is dissimilar to the previous devices in some aspects. The inlet tube contracts into a small nozzle, $R/R_c = 0.02$, which results in particle impaction and possibly a free jet expansion as the distance from the collection surface is high compared to the inlet nozzle radius, $H/R = 20$.

Furthermore, the fluid outlet is towards the top, which results in some particles running-off directly to the outlet without traveling close to the collection surface, i.e. a collection efficiency, $\eta < 1$, without having particle deposition over the entire collection surface ($r^\dagger_{f,\max} < 1$). Hence, using a plug-flow assumption (based on sudden contraction of fluid flow profile), we calculate the critical radial position r^*_{ic} of the particle in inlet tube, beyond which the particles run-off and contribute to the deposition efficiency, $\eta = r^{*\,2}_{ic}$ reported by the authors. This is mainly because the authors report $\eta < 1$ while having $r^\dagger_{f,\max} < 1$. Hence, we assume that the run-off adjusted particle position r^*_{ic} and not at $r^*_{i,\max}$ corresponds to the outermost position on the collection surface measured by the authors. We compare the reported $r^\dagger_{f,\max}$ against the run-off efficiency and drift corrected FIR-model calculations (Figure 3.11d). Accuracy of the evaluation is subsequently better for each experiment with larger sized particles as the impaction effect reduces and other possible wall-effects or small-particle-related effects possibly reduce. Despite these experiments having a design and operation that is far from the base-design (Figure 3.2), and having extremely small nanoparticle sizes, the FIR model could predict the collection performance.

Overall, these comparisons illustrate the flexible application of the FIR model. With different inlet tube sizes, separation distances, flow rates and electric field conditions, the model was able to provide some estimate of the particle collection dynamics.

3.4.3   Exploration of spatial particle distributions for various inlet conditions

Mapping each particle from $r^*_i \leq r^*_{lim}$ to its corresponding final position $r^\dagger_f$ generates deposition profiles for various inlet conditions (Figure 3.12). There is a small deviation near
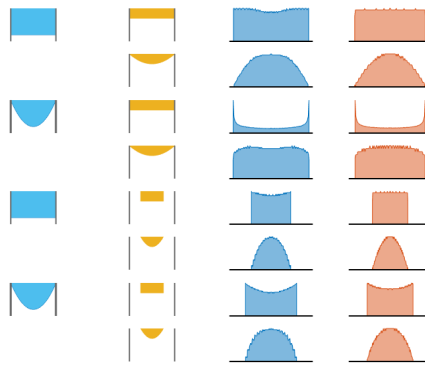
Figure 3.12: Predicting final particle deposition profile using the analytical model (right most column) and comparing against the deposition profile from COMSOL simulations (3rd column) for plug-flow inlet or parabolic-flow inlet velocity flow profile (1st column) and for uniform or parabolic particle distribution in the inlet tube, with or without sheath flow (2nd column).

the center of the deposition, where the deposition profile from COMSOL Multiphysics has a "recess" which is not represented by the FIR model. As mentioned in Section 3.3.1.2, this

discrepancy results because of the lower E field in z-direction just below the tube outlet leads to further migration of particles radially than estimated by an invariant E-field assumed by the FIR model. However, other features of the deposition profile are well-reproduced by FIR (and corrections to nonuniformity estimates due to this recess are discussed in Section 3.4.1.2); particularly the merits of sheath flow that makes the spatial deposition profile much more uniform for a parabolic-flow-inlet.

Previous studies reported a "top-hat" deposition profile from radial ESPs (Dixkens and Fissan, 1999; Preger et al., 2020) and that the final particle velocity profile is representative of the deposition profile (Dixkens and Fissan, 1999). We instead find the deposition profile for a parabolic-flow inlet with uniform-particle-distribution (2nd row in Figure 3.12) to be closer to an inverse parabola, which is supported by the increasing proximity of the particle trajectory lines farther away from the center in Figure 3.6b. The sharp rise at the periphery is also caused by discontinuity in the high-voltage plate electrode (use of a ring-electrode at the exit of the sample inlet could reduce such effects, but at a substantial expense to collection performance). The difference with the conclusions from (Preger et al., 2020) may be due to their examination of deposition profiles with binned concentrations in particles per area, from which a top-hat can be derived when normalizing by the collection area. Furthermore, z-direction velocity magnitude are shown not to be indicative of deposition profiles when considering a range of scenarios (Appendix C.7, Figure C.2). Ultimately, these tools must be used to find the least nonuniform configurations when spatial uniformity is desired.

Preliminary sheath flow addition ($r^*_{lim} < 0.5$) has the potential to improve spatial uniformity based on the deposition profile for parabolic flow inlet and uniform particle inlet (Figure 3.12. The sheath flow advantage is one of the main reasons large R devices should be modeled accurately along with ensuring that the flow is laminar and impaction is negligible.

3.4.4   Exploration of collection performance for various parameter values

In this section we describe a new 2D visualization to represent ESPs, and compare their collection dynamics over extensive conditions.

For a given distribution, the particle collection performance (related to $r^\dagger_{f,\max}$) is dependent on $r^\dagger_{geo}$; r^*_{lim}; H/R (which affects drift) and the product of $\alpha\beta$, which appears as a single term in the analytical model. We demonstrate this approach for a parabolic-flow inlet in Figure 3.13 using a new 2D visualization, where contours of $r^\dagger_{f,\max}$ are shown for different values of $r^\dagger_{geo}$ and different orders of magnitude of the product $\alpha\beta$. Different plots are shown for changing r^*_{lim} and H/R. A combined range of $\alpha\beta \approx 10^{-3}$ to 10^2 has been used for the plots based on the individual ranges discussed previously. In our observation simulations with $H/R > 1$ had electric fields that are similar to that for $H/R = 1$, so efficiencies are similar, though for very high $H/R \gg 1$ jet-expansion effects (Bergthorson et al., 2005; Bühler, Obrist, and Kleiser, 2014) (the physics of which is not included in the model) can reduce the efficiencies.
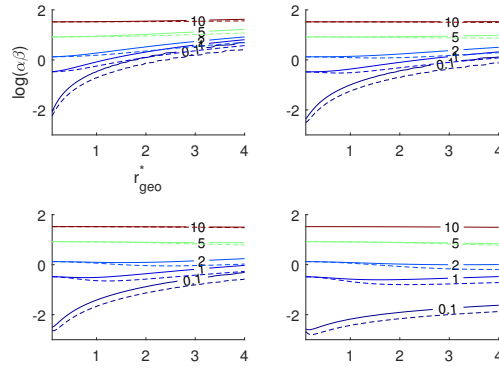
Figure 3.13: Collection performance (in terms of $r^{\dagger}_{f,\max}$) for various operating condition and particle sizes ($\alpha\beta$), geometry (r^{*}_{geo} and H/R), and inlet sheath condition (r^{*}_{lim}) - each column corresponds to $r^{*}_{lim} = 0.3, 0.5, 0.7$ and 1, respectively for $H/R = 1$ (solid lines) and $H/R = 0.5$ (dotted lines).

The collection performance with respect to r^{*}_{lim} is not monotonic, because two separate terms in the FIR-model, $r^{*}_{lim}{}^{2}$ and $\left(2 - r^{*}_{lim}{}^{2}\right)$ increase and decrease, respectively, with an increasing r^{*}_{lim}. As expected, $r^{\dagger}_{f,\max}$ for small Q_a (lower $\alpha\beta$) and smaller apparent inlet $r^{\dagger}_{geo}$ would be very low as the drift effect would push the particles very close to the center. Moreover, this effect is more prominent for lower r^{*}_{lim} values as the particles are closer to the center initially, and for higher H/R which corresponds to larger drift. On the contrary, at very high Q_a or very low E_0 (high $\alpha\beta$), the drift effect is negligible and the value of $\alpha\beta$ controls $r^{\dagger}_{f,\max}$ values (as $\alpha\beta \gg r^{\dagger}_{geo}$). For moderate Q_a ($\alpha\beta > 1$), it is interesting that the effects of drift and radially outward particle migration counter-balance themselves such that the $r^{\dagger}_{f,\max}$ contours stay within similar order-of-magnitude of $\alpha\beta$ for different $r^{\dagger}_{geo}$. At a constant $r^{\dagger}_{geo}$ closer inter-distance of any two iso-$r^{\dagger}_{f,\max}$ contours suggests a higher sensitivity to $\alpha\beta$ at that point, i.e. when the contours are closer a smaller change in operating parameters or particle related property results in a change in $r^{\dagger}_{f,\max}$ that is higher than in a case where the contours are further apart.

This $\log(\alpha\beta) - r^{\dagger}_{geo}$ space facilitates understanding particle collection behavior for parabolic-flow inlet in a radial ESP. For example, the points simulated using COMSOL Multiphysics in Figure 3.7 are represented on the space in Figure 3.14a, and the experimental points in Figure 3.11 that used parabolic-flow inlet and do not have jet expansion are represented on the space in Figure 3.14b. This representation allows a quick approximation and understanding of $r^{\dagger}_{f,\max}$ for a given design by comparison to reference contour plots. A device operating at a particular condition collecting a specific particle size will be a point on this 2D-space. For a poly-disperse aerosol population, multiple points at the same $r^{\dagger}_{geo}$ will ensue. A desirable design space to reduce size-dependence of collection efficiency can be found in regions with slowly varying contours. For a fixed particle-size range (D_p), the corresponding range of β is constrained and

for a fixed geometry ($r^\dagger_{geo}$), and at a particular value of the variable α, the difference in $r^\dagger_{f,max}$ over the D_p is lowest. For example, if a device is already built with no sheath flow (i.e. $r^*_{lim} = 1$) and has $H/R = 1$ (Figure 3.14b), and $0.25 \le \eta \le 1$ is desirable, then $r^\dagger_{geo} = 1.5$ has the farthest separation between $r^\dagger_{f,max} = 1$ and $r^\dagger_{f,max} = 2$ lines (Figure 3.13).

Another example of the model application is in device design for environmental chamber experiments where lower sampling flows are advantageous along with high collection efficiencies (say $\eta = 1$). The contour for $r^\dagger_{f,max} = 1$ in Figure 3.13 (for $H/R = 0.5$) for different r^*_{lim} allows choosing a $r^\dagger_{geo}$ such that the flow rate (translated to α) value is the lowest for a given particle size and charge (fixed β). For $R_c = 10$ mm, $r^*_{lim} = 0.5$, $E_0 = 3$ kV/mm, $D_p = 500$ nm, $n = 20$, Q_a has a lowest value of $Q_{a,min} = 2.28$ LPM at $r^\dagger_{geo} = 0.77$ i.e. $R/R_c = 1.54$ or $R = 15.4$mm - a radius larger than R_c, which is counter-intuitive without sheath flow considerations. Similarly, the model has numerous other applications for device design and tuning existing devices. An elaborate example of using the model for a device design for IR spectroscopy analysis is presented by us in Part II of this paper (Dudani and Takahama, 2021b).

(a) (b)
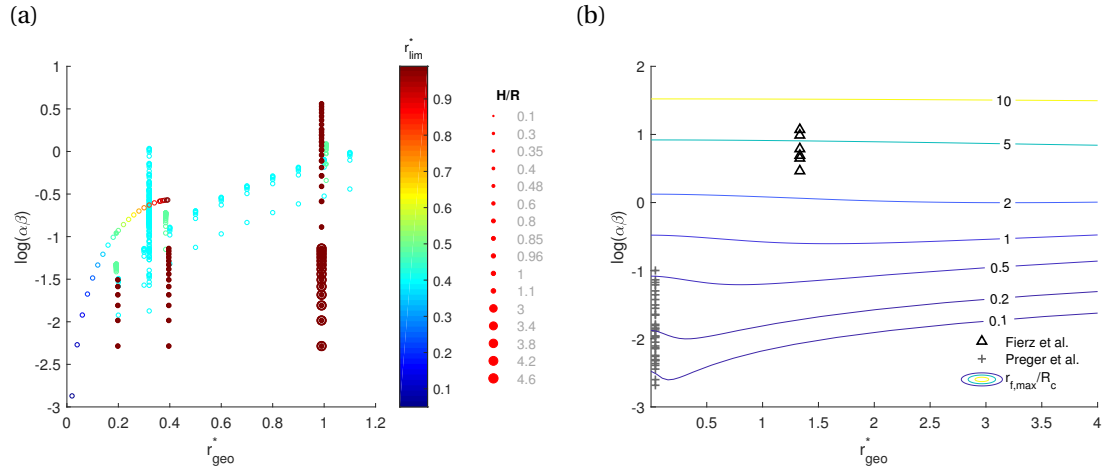
Figure 3.14: (a) Representation of COMSOL Multiphysics simulations from Figure 3.7a on the $\log(\alpha\beta) - r^\dagger_{geo}$ space with difference color-coded r^*_{lim} and different point sized H/R values. (b) Representation of prior experiments with parabolic-flow inlet from Figure 3.11 on the $\log(\alpha\beta) - r^\dagger_{geo}$, along with $r^\dagger_{f,max}$ contours for $r^*_{lim} = 1$, the relevant r^*_{lim} for both the prior devices (Fierz, 2007; Preger et al., 2020).

3.5 Conclusions

In this work, we derive an analytical model (the finite-radius model, or FIR) to explain particle deposition dynamics in a two-stage ESP. We model the collection dynamics in a linear (constant velocity in direction of flow) and a radial ESP (radially decreasing velocity). Additionally, the charged particles entering a radial ESP drifts towards the center in the inlet tube and is explained with the linear ESP equation. The combined drift and collection equation forms

the finite inlet radius (FIR) model and is a mapping function from inlet position to that on the collection surface, as a functions of several geometric, operating, inlet and performance variables. The model is capable of modeling sheath flow and different inlet flow and particle distribution profiles. It is valuable for predicting particle deposition dynamics in cases where numerical simulations are difficult and for analyzing a large number of designs simultaneously. We found the FIR model to generate useful characterizations of collection efficiency and deposition profiles when evaluated against COMSOL Multiphysics simulations and previous experimental devices. Some prediction errors against numerical simulations were mainly attributed to varying $E_z(r, z)$ under the electric tube, which is assumed as constant in the analytical model.

We introduce new dimensionless numbers that parameterize the FIR model: the ESP operating number, α, ESP particle number β and the radial ESP apparent inlet radius $r_{geo}^\dagger$. We found these numbers to be physically significant and useful in explaining ESP performance over orders-of-magnitude of values of α and β. Using these numbers we also propose a new 2D-graph to plot ESP designs and visually compare device performance. For the range of operating conditions over which the fundamental assumptions of the FIR model are valid i.e. for laminar flow and for no impaction, there are some interesting equivalencies amongst the operating and geometric variables. The entire model is scalable i.e. for a higher R_c, if α, β, r_{lim}^* and $r_{geo}^\dagger$ are maintained the same, then the relative performance $r_f^\dagger$ remains unchanged. Q/E_0 appears in α in both the drift number Ω and the collection region equation, which implies that proportional change in both the variables results in the same collection performance. The final particle position is closer to center because of drift. H/R does not affect the dynamics in the collection region but does affect Ω as it indirectly affects the E under the inlet tube. The deposition profile for a parabolic-flow-inlet is an inverse parabola and is not the same as the particle velocity distribution upon collection.

Overall, the analytical model emerges as a useful tool that is applicable to versatile real-life scenarios, where using the model can result in estimation of appropriate operating conditions, or for comparing or creating device design. The model has applications in controlled particle deposition applications and enables much higher tunability of ESP devices.

3.6   Nomenclature

- C_c - Cunningham slip correction factor
- $D_p(m)$ - Particle diameter
- $e(C)$ - Elementary charge on an electron
- $E_0(V/m)$ - Electric field in the collecting region
- $H/H_{elec}(m)$ - Spacing between the two electrodes at the tube exit and the collecting substrate
- $H_{flow}(m)$ - Approximate height of the radial flow profile right after stagnation point flow.
- Kn - Knudsen number of the particle

- $L(m)$ - Length of the collecting substrate for linear ESP system
- n - no. of elementary charges on a particle
- $q(C)$ - Total charge on a particle
- $Q(m^3/s)$ - Inlet flow rate in the system
- $Q_a(m^3/s)$ - Inlet aerosol flow rate in the system
- $r_i(m)$ - Initial position at the inlet in the radial direction for radial ESP system
- $r_0(m)$ - Initial position at the exit of the tube (or at the entry to the collection region) in the radial direction for radial ESP system
- $r(m)$ - Position in the radial direction at any given t for radial system
- $R(m)$ - Radius of the inlet tube
- $R_c(m)$ - "Characteristic" radius of the device
- r^* - Dimensionless radial position with respect to the inlet radius R.
- $r^\dagger$ - Dimensionless radial position with respect to the characteristic radius R_c.
- r^*_{lim} - Sheath position in the inlet tube
- $r^\dagger_{geo}$ - Dimensionless term that relates to the device geometry.
- $t(s)$ - Time
- $V_0(V)$ - Voltage difference between the two electrodes.
- $v_{in}(m/s)$ - Mean velocity of the particle in the inlet tube
- $v_{elec}(m/s)$ - Mean migration velocity of the particle in the influence of the electric field
- $v_x(z)(m/s)$ - The velocity profile in the x direction as a function of height
- $v_r(r,z)(m/s)$ - The velocity profile in the r direction as a function of r and z
- $W(m)$ - Width of the collecting substrate for linear ESP system
- $x(m)$ - Position in the horizontal direction at any given t for linear 2D system
- $z_0(m)$ - Initial position in the vertical direction
- $z(m)$ - Position in the vertical direction at any given t
- α - New dimensionless ESP operation number
- β - New dimensionless ESP particle number
- η - Efficiency of collection
- Γ - Ratio of the dimensionless final position on the collection surface to the dimensionless position before entering collection region
- $\mu(Pa.s)$ - Dynamic viscosity of the carrying fluid (air in this case)
- Ω - Extent of the drift in the inlet tube, expressed as a ratio of the final radial position after drift to the initial position before drift, r^*_0/r^*_i

4 Design of an electrostatic aerosol collector part 2: design for poly-dispersed aerosol collection for spectroscopy analysis

Chapter 4. Design of an electrostatic aerosol collector part 2: design for poly-dispersed aerosol collection for spectroscopy analysis

4.1   Abstract

Aerosol collection for ambient monitoring and laboratory studies are inherent in any aerosol measurement technique and different collector types and design are in use. Electrostatic precipitators (ESP) present the advantage of higher tunability and lower pressure drop which has motivated design of several devices for different applications with direct or indirect measurement of aerosol. Spectroscopy methods are non-invasive and infrared (IR) spectroscopy allows measuring functional-group information and has been shown to be useful in chemically-speciated mass measurements. Despite the large range of ESP designs, their application has been specific and not directly transferable for use in transmission-IR-spectroscopy application. Unlike impaction and filtrations the methods of evaluating ESP designs against design objectives have been diverse, further diminishing facile cross-evaluation. We present a method of designing a two-stage radial ESP by establishing distinctive design objectives and evaluating them against multiple geometric, operating and inlet variables associated with an ESP. The connection between the variables is established through an analytical model which is used to valuate the objectives. We identify the trade-offs among the variables and use a qualitative and quantitative analysis to identify their values that are appropriate for the design objectives. The obtained design-space additionally takes into consideration other physical constraints and elucidates the ESP geometry and operating conditions that facilitate quantitative measurement of chemical composition using transmission-IR-spectroscopy. The obtained results and the presented design methodology both are transferable to different spectroscopy methods and other applications where an ESP device is required for collecting poly-dispersed aerosol while reducing collection artifacts.

Keywords: Design, ESP, radial, two-stage, aerosol, collection.

4.2   Introduction

Particulate matter (PM) analysis is important to understand the aerosol chemical composition and their related health effects. Currently, PM is monitored in terms of mass concentrations and filter collection for offline measurement has remained the dominant method of analysis. For mass or chemical analysis semi-continuous devices have also been used (McKeown, Johnston, and Murphy, 1991; Weber et al., 2001; Öktem, Tolocka, and Johnston, 2004; Su et al., 2004). Some independent collectors and samplers have been developed for either direct or subsequent analysis of PM (I. V. Novosselov et al., 2014; Iida et al., 2017; Kim, Sioutas, and Chang, 2000; Foat et al., 2016) especially for applications in bio-aerosol sampling (T. Han, Fennell, and Mainelis, 2015; Pardon et al., 2015; Ma et al., 2016; Mahamuni, Ockerman, and I. Novosselov, 2019). The common methods of collecting the particles have been inertial impaction (V. A. Marple, Rubow, and Behm, 1991; V. A. Marple, Rubow, and Olson, 1995; Mercer, Tillery, and Newton, 1970; Furuuchi et al., 2010) (sometimes with inertial focusing (P. Liu et al., 1995)), filtration (Yaffe, 1943; Monnett, 1920; Soo et al., 2015), liquid impinges (Michaelis, 1890; Winslow, 1908) and electrostatic precipitation (Ofner, Krüger, et al., 2009;

Dixkens and Fissan, 1999; Fierz, 2007). Each method of collection has its own limitations and advantages. Impactors have bounce off effects and liquid/ solid based difference in collection performance (Dzubay, Hines, and Stevens, 1976; Esmen and T. C. Lee, 1980); filtration methods create large pressure drop and other sampling biases (C.-N. Liu et al., 2014; Vecchi et al., 2009); impinges require an external liquid media to hold the aerosol that can modify the composition and has size and volume dependence (Y. Zheng and Yao, 2017); and conventional ESP uses high electric field strengths that can perturb the aerosol and result in biases. Except ESP devices, other methods require bulky vacuum pumps to overcome high pressure drops and can also be a disadvantage for certain applications.

Limitations of the collection method become increasingly important when the chemical information of the PM is needed to be determined. As the chemical composition is size-dependent, it becomes important to consider size-dependent parameters, such as efficiency and losses. As more standardized device setups, filtration (Caroff, Choudhary, and Gentry, 1973; Stafford and Ettinger, 1972; Montassier, Dupin, and Boulaud, 1996; Sioutas, 1999; Yamamoto et al., 2004; Soo et al., 2015) and impaction (Vanderpool et al., 2001; C.-Y. Lai et al., 2002; Furuuchi et al., 2010; Durand et al., 2014) have been rigorously analyzed for the size, velocity, loading or time based dependence of collection-efficiency or profile. These effects remain less of a consideration for methods of analysis that subsequently use the collected aerosol in an altered form i.e. either thermally desorbed (Greaves, Barkley, and Sievers, 1985; Veltkamp et al., 1996) or transferred through solvent extraction (Cheng and S.-M. Li, 2004). Spectroscopy or spectrometric methods however can be more sensitive to these factors. Some guidelines and standards have been suggested on collector designs (Lidén, 1994; Chow, 1995), though it mostly always remains a question of the performance, novelty and statistical robustness against reference measurements that remains the concluding test.

ESP devices have a large range of design geometry and each device has been analyzed for the dependencies mainly by the authors, but the method of analysis also remains large. Linear ESP devices (Ofner, Krüger, et al., 2009; Harrick and Beckmann, 1974; B. Y. H. Liu, Whitby, and Yu, 1967; T. T. Han, Thomas, and Mainelis, 2017); cylindrical ESP devices (Mahamuni, Ockerman, and I. Novosselov, 2019) and radial ESP devices (Dixkens and Fissan, 1999; Fierz, 2007; Kala et al., 2012; Preger et al., 2020) are the most commonly developed types. ESP devices for different spectroscopy applications (Chippett and Gray, 1978; B. Y. H. Liu, Whitby, and Yu, 1967; Dixkens and Fissan, 1991; Mahamuni, Ockerman, and I. Novosselov, 2019) have been developed over the years, and some recent devices collect the particles on a miniscule collection area for Raman spectroscopy (L. Zheng et al., 2017). For infrared (IR)-spectroscopy a deposition larger than the beam is required to prevent beam filling or other optical effects and lower size-dependence in collection is required to quantitatively analyze poly-dispersed aerosol.

For IR-spectroscopy applications, some ESP collectors for attenuated total reflection (ATR)-IR spectroscopy exist (Ofner, Krüger, et al., 2009; A. Arangio et al., 2019) but ATR-IR-spectroscopy has been shown to have inherent size-dependence in measurement because of the wavelength

dependent evanescent wave (**Milosevic2012**; A. Arangio et al., 2019). ESP collector designs that enable transmission IR spectroscopy are rare. Few reports are available concerning the method of development of a collector design, along with its design objectives and variables. COMSOL Multiphysics remains the dominant method of choice for designing a device through simulation-prototyping-cycle. In most applications, the substrate dimensions or desired flow rate are known and high collection-efficiency is desired and using COMSOL still remains a facile method of designing and verifying the performance of a collector device.

In this exploratory study, we identify and define the objectives that are important considerations for being able to make quantitative chemical fraction composition measurement of PM with IR spectroscopy. Filtration (Russell, Bahadur, and Ziemann, 2011; Takahama, Schwartz, et al., 2011), electrospray (A. Arangio et al., 2019) or pressing the sample against IR optical substrate (Hung, Y.-Q. Chen, and S. T. Martin, 2012) have used for analysis with IR spectroscopy. We propose the design that would allow collection directly on an IR transparent surface while aiming for lower chemical detection limit and higher collection-efficiency of PM in the accumulation mode, all while reducing chemical modification possibility in the ESP device. The design is formulated by using an analytical equation that has been formed for a two-stage radial ESP and includes various design and operating parameters and sheath flow consideration (Dudani and Takahama, 2021a). The paper describes the device design which collects PM$_{2.5}$ after charging the particles and collecting it using the defined geometry and the operating conditions.

4.3 Method

The design goal is to determine the geometry and operation of a two-stage radial ESP to employ in a quantitative analysis of aerosol composition using IR-spectroscopy with the objectives that relate to the goal (Section 4.3.2). The goal is achieved by collecting particles on an IR-transparent substrate and is founded on a combination of qualitative and quantitative analysis of the different geometric and operating variables, inlet conditions and performance variables which are inter-related by the analytical model in the Section 4.3.1. It allows assessing the effect of the variables on the objectives in order to determine the design specifications.

4.3.1 Finite inlet radius (FIR)– model for a two-stage electrostatic precipitator

The particle collection dynamics in a two-stage ESP is explained by the FIR model (Dudani and Takahama, 2021a), shown in Table 4.1 for a parabolic flow inlet. It includes the change in particle position in two main regions, the drift in the inlet tube where the average velocity in the direction of motion is a constant and the collection region where the average velocity reduces with increasing r. Both regions have the electric field acting perpendicular to the flow. Ω is the term that results from the particle drift in the inlet tube and is the ratio of the final position of the particle after drift (r_0^*) to the position before drift at the inlet (r_i^*), and the combined final position on the collection surface is r_f/R_c. Primarily, some key summarizing

Table 4.1: FIR model equations for the collection zone (first row) and the drift in the inlet tube, Ω (second row) for a parabolic flow inlet, along with the variable descriptions in their respective categories.

$$r_f/R_c = \Omega\left(\frac{r_i^*}{r_{lim}^*}\right)\sqrt{r_{geo}^{\dagger 2} + 3\alpha\beta\left(\frac{2 - \Omega^2 r_i^{*2}}{2 - r_{lim}^{*2}}\right)}$$

$$\Omega = \frac{r_0^*}{r_i^*} = f\left(r_i^*, \frac{H}{R}, \frac{R}{R_c}, \alpha, \beta\right) \;;\; r_{geo}^{\dagger} = \left(r_{lim}^*\frac{R}{R_c}\right) \;;\; \alpha = \frac{Q_a\mu}{eE_0R_c} \;;\; \beta = \frac{D_p}{nC_cR_c} \;;\; r_0^* = \frac{r_0}{R} \;;\; r_{lim}^* = \frac{r_{i,\mathrm{max}}}{R}$$

$$0 \leq r_i \leq r_{lim}^* \;;\; 0 \leq \Omega \leq 1$$

$$\Omega^3 - \frac{3}{r_i^{*2}}\left(1 + \frac{v_{\mathrm{elec},r}}{2v_{\mathrm{in}}}\right)\Omega - \left\{1 - \frac{3}{r_i^{*2}}\left(1 + \frac{v_{\mathrm{elec},r}}{2v_{\mathrm{in}}}\right) + \frac{3}{r_i^{*3}}\left(\frac{v_{\mathrm{elec},r}}{2v_{\mathrm{in}}}\right)\right\} = 0$$

where $v_{\mathrm{in}}/v_{\mathrm{elec}} = \dfrac{1}{E_{\mathrm{corr}}}\dfrac{3\alpha\beta}{r_{lim}^{*2}(2 - r_{lim}^{*2})}\left(\dfrac{R}{R_c}\right)^{-2}$; $E_{\mathrm{corr}} = f(H/R)$

Geometric variables	Operating variables	Inlet variables	Performance variables
R_c: Collection disc radius R: Inlet radius H: Electrode separation distance	Q_a: Aerosol flow rate E: Electric field strength V_0: Voltage difference between $z = 0$ and $z = H$	D_p: Particle diameter n: no. of elementary charges on the particle r_{lim}^*: Sheath position r_i^*: Inlet position	$\frac{r_f}{R_c}$: Dimensionless final position of deposition

points from the equation that are useful considerations in the design approach.

1. H/R affects Ω only as the ratio affects the radial distribution of electric field which affects the drift in the inlet tube.

2. Q_a/E_0 is present as a term in both the drift and the collection equations through the presence of α. Hence, doubling the electric field and aerosol flow rate concurrently will not alter the collection in any manner, provided the assumptions of laminar flow and no-impaction are not violated.

3. nC_c/D_p is present as a single term in both the drift and the collection equations through the presence of β. If $nC_c \propto D_p$ then the system has no size-dependence in collection. Most particle chargers however charge the particle such that $n \propto D_p$ in which case C_c (which spans orders-of-magnitude) becomes the main contributor to size-dependence.

4.3.2 Design objectives

For IR spectroscopy applications, the collection process and the deposition profile should achieve some objectives aimed at increasing the quantitative capabilities for a poly-dispersed PM population. Any collection method introduces some bias in the collected sample and the objectives are formed around reducing them by diminishing the possibility of modifications to the chemical composition or size of the particles in the population and by collecting more particles faster to reduce the time taken for a measurement.

1. High spatial-uniformity in the deposition pattern relates to a higher consistency of

mechanical, chemical, and optical properties across the film. Many factors can cause spatial non-uniformity in deposition, such as velocity profile in the inlet tube, radial particle-concentration-profile in the inlet tube, impaction effects, and presence of obstruction in flow line/ inlet tube.

2. Low size-dependence in collection is desired because aerosol chemical composition is size-dependent and the deposition film should minimize the sensitivity of deposition pattern to particle sizes. Particles of different size will have different charge and different flow drag and hence will follow different paths. The dependence biases the analysis of the collected particles and is not desirable.

3. Low chemical-interference of the particles during or after collection introduces the modification in the aerosol sample and is a point of deliberation in ESP devices. Reactive molecules (e.g., ozone, radicals) are produced from gases in air in regions of very high-electric field strength. They can change the chemical composition of the deposited particles by either contributing to generation of condensable or directly reacting with particles in the flow steam or those that are already deposited if it reaches its vicinity.

4. High collection-efficiency reduces the probability that collected particles are unrepresentative of the inlet population.

5. High collection-mass-flux enables rapid particle accumulation on the collection surface over a given period of time and describes the overall throughput of the system. The operating conditions determines the achievable deposition volume flux for a pre-specified collection efficiency.

The objectives are defined and summarized in Table 4.2. All the objectives are defined in terms of the performance or operating variables except "Low chemical-interference" which is not measurable in terms of the design parameters but is expected to be a direct result of modifications because of gas ionization and free radical reactions during or after collection. In this regard, chemical-interference is reduced by using limited but adequate voltages or electric field strength during charging and collection. Non-uniformity takes into consideration all the final particle positions corresponding to a uniform particle-inlet-concentration distribution ($0 \leq r_i^* \leq r_{lim}^*$). It is the ratio of the median absolute median deviation normalized by the median of the difference in the position of subsequent particles. The measure has been selected as median is more robust to local perturbations and has been previously shown to be more accurate when comparing against COMSOL Multiphysics simulations (Dudani and Takahama, 2021a). Collection efficiency and size-dependence are based on the outermost particle position $r_{f,max}/R_c$ because the spatial deposition profile is nearly a constant for a given inlet-flow-profile and r_{lim}^* allowing comparing the final position for variable sizes to assess the size-dependence. As collection efficiency, η is inversely related to the aerosol flow rate Q_a, but the overall throughput is related to the effective aerosol flow rate ηQ_a, the collection volume flux φ is useful to find an operating region where the trade-off is well balanced.

Table 4.2: Definition and acceptability criteria for the different design objectives.

Property	Definition	Objective
Non-uniformity	$$\Delta_r = \frac{\text{median}|x_i - \tilde{x}|}{\tilde{x}} \;;\; \text{where} x_i = \left(\frac{r_f}{R_c}\right)_i - \left(\frac{r_f}{R_c}\right)_{i-1}$$	$\Delta_r \leq 0.05$
Chemical-interference	c(Free radicals) ; where c is the total concentration in the particle stream of the device	$c \downarrow$
Collection efficiency	$$\eta = \frac{\int_0^{R_c} r f(r) dr}{\int_0^{r_{f,\text{max}}} r f(r) dr} \;;\; \text{where} f(r) = \text{pdf}\left(X = \frac{r_f}{R_c}\right).$$ For uniform deposition, $f(r) = \text{const}$, i.e. $\eta = \left(\frac{r_{f,\text{max}}}{R_c}\right)^{-2} = \frac{A_{\text{ref}}}{A_{\text{deposit}}}$	$\eta \geq 0.95$
Size-dependence	$$\Delta_{D_p} = \frac{\text{median}|x_i - \tilde{x}|}{\tilde{x}} \;;\; \text{where} x_i = \frac{r_{f,\text{max}}(D_p)}{R_c} \;;$$ $\log(D_p) = \text{Uniform}(\log(D_{p,\text{min}}), \log(D_{p,\text{max}}))$	$\Delta_{D_p} \leq 0.1$
Collection-volume-flux	$$\varphi = \left(\frac{\eta Q a}{\pi R_c^2}\right)$$	$\varphi \uparrow$

4.3.3 Numerical simulations

For illustrations that show the final particle deposition profile, COMSOL Multiphysics simulations are used (Figure 4.3 and Figure 4.1) as the changes in the electric field under the inlet tube affects the deposition and the FIR model does not include its effect. The effect is accommodated to evaluated the overall uniformity (Section 4.4.1.2) but the exact spatial deposition profile might not be accurate in the extreme cases (low H/R). COMSOL simulations are also used to assess the change in electric field over the collection surface for different R/R_{elec} and H/R. The simulation comprises a steady-state study of the laminar flow and electrostatic fields in a given design, and a time-dependent particle-tracing study of differently sized particles. The mesh is extremely fine and physics dependent and turbulent flow physics have not been used even if the simulation has a large scale eddy, as the eddy is resolved through the laminar flow physics, as confirmed by the flow field remaining unchanged after refining the mesh further. (Dudani and Takahama, 2021a) shows additional details of the simulations and their comparison against the FIR model.

4.4 Results and discussion

The dependence of the objectives on the design variables is not apparent from the FIR model and the effect of different variables can be favorable or unfavorable to different objectives. A summary of the final design variable ranges, along with a qualitative direction of a variable which is favorable to an objectives is shown in Table 4.3. Though the table presents a qualitative analysis of the variables, some of the effects are not monotonic and the details of the trade-offs are highlighted in the subsequent sections. In addition to the design objectives, some consideration of the limits of the FIR model and other practical considerations are discussed in Section 4.4.6 and 4.4.7 respectively. The variables are sequentially constrained by each analysis and the final design space is identified.

4.4.1 Spatial uniformity

For a given combination of inlet velocity profile and particle spatial distribution, we have shown 1) that the final spatial distribution profile on the collection surface is close to an inverse-parabolic distribution, and 2) the overall nonuniformity in the deposition as observed in COMSOL simulations can be predicted by FIR using combined nonuniformity from particle deposition and nonuniformity in electrical field (estimated from ring charge) over the collection area (Dudani and Takahama, 2021a). Local and overall non-uniformity can be different and both are important considerations. The overall nonuniformity is calculated over all the entire deposition position range (0 to $r_{f,\mathrm{max}}/R_c$) final positions, whereas the local nonuniformity is calculated over a 5% moving-window on the final position.

Table 4.3: Qualitative assessment of design variables on the different design objectives, along with its final value/ value range based on design analysis in the respective sections.

		High spatial uniformity	Low chemical interference	High collection efficiency	Low size dependence	High collection volume flux iii	Final value	Sections
Geometric	R_c ii	-	-	-	-	-	12.7 mm	4.4.6
	R/R_c i	-	-	Lower	Higher	-	0.4 - 0.8	4.4.3.2 4.4.4.1 4.4.5.2 4.4.6.1 4.4.7.2
	H/R	Higher	-	Higher	Lower	-	1	4.4.1.2 4.4.3 4.4.4
	R/R_{elec}	Lower	Lower	-	-	-	≤0.5	4.4.1.3 4.4.2
Operating	Q_a	-	-	Lower	Higher	Higher	1.7 - 3.5 LPM	4.4.3 4.4.4.2 4.4.5.1
	E_0	-	Lower	Higher	Lower	-	1-2 kV/mm	4.4.2.1 4.4.3 4.4.4
	V_0	-	Lower	-	-	-	≤ 10 kV	4.4.2.2
Inlet	D_p ii	-	-	-	-	-	0.1 - 2.5 µm	4.4.4.3
	n ii	-	-	Higher	-	-	$D_p(nm)/20$	4.4.3.1
	r^*_{lim} i	Lower	Lower	Lower	Higher	-	≤ 0.4	4.4.1.1 4.4.2 4.4.3.2 4.4.4.1 4.4.5.2 4.4.6.1 4.4.7.1

i Subject to combined $r^{\dagger}_{geo} \geq 1.5$ (Section 4.4.5.2)
ii Variables constrained as design inputs or charger output
iii Also higher for higher η (column "High collection efficiency")

Chapter 4. Design of an electrostatic aerosol collector part 2: design for poly-dispersed aerosol collection for spectroscopy analysis

4.4.1.1 Inlet condition: r_{lim}^* - Sheath flow position

For laminar flow, as considered in the present design, the flow develops into a typical parabolic-flow-like profile. The associated spatial deposition profile is shown in Figure 4.1a (lower half). Changing the sheath flow alone has a large effect on the non-uniformity as evident when comparing Figure 4.1a (no sheath) and Figure 4.1b (sheath with $r_{lim}^* = 0.5$). Using sheath flow moves the particle stream more towards center and in effect increases the overall uniformity. More precisely, the nonuniformity measure, Δ_r, for different r_{lim}^* is shown in Figure 4.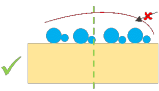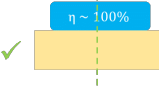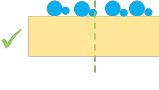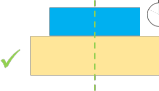2 and with a cut-off of 5% nonuniformity, it emerges that $r_{lim}^* < 0.5$ should be maintained. In that limiting case $r_{lim}^* = 0.5$ though, any nonuniformity in the electric field (Δ_{r,E_0}) will make the combined nonuniformity (Δ_r) exceed this limit. Hence, accommodating a 2.5% non-uniformity in electric field ($\Delta_{r,E_0} = 0.025$) as derived in Section 4.4.1.2, along with the limit on combined nonuniformity of $\Delta_r < 0.05$, the nonuniformity because of sheath alone should be $\Delta_{r,r_{lim}^*} < 0.026$, which corresponds to $r_{lim}^* \leq 0.4$. The local variability (Δ_r over a 5% moving window) is also low for these cases (Appendix D.1, Figure D.1). r_{lim}^* itself might be further constrained by size-dependence considerations (Section 4.4.4.1), high collection flux (Section 4.4.5.2), with lower limits imposed by Reynolds number limits (Section 4.4.6.1) and other practical considerations (Section 4.4.7.1).

4.4.1.2 Geometry: H/R - Ratio of the separation distance to the inlet tube radius

Electric field non-uniformity because of top electrode discontinuity just under and around the inlet tube is another main contributor to the deposition profile nonuniformity. As explored by (Dudani and Takahama, 2021a), the effect is dependent on H/R and the radially and axially changing electric field not only affects the extent to which particles drifts in the inlet tube but also the collection performance and uniformity. A simple illustration of changing H/R is sown in Figure 4.3 where all other parameters are kept the same. Additionally, as R_c is the size of interest for collection, different R/R_c values change the proportion of length over R_c for which the electric field is changing. By changing the H/R values for different R/R_c, the changing nonuniformity (Δ_{r,E_0}) in the electric field over R_c is shown in Figure 4.4. The overall large-scale nonuniformity, Δ_{r,E_0} goes to 0 for values of $R/R_c < 0.5$ as more than 50% of the points have the same value E_0, making the median $\tilde{x} = E_0$ and hence the median$|x - \tilde{x}| = 0$. The small scale, or local, variations in the profile (Δ_{r,E_0} over a 5% moving window) is however very high for $R/R_c < 0.5$ (Appendix D.2, Figure D.2b). For $H/R = 1$, Δ_{r,E_0} is around 2.5% and nearly independent of R/R_c which allows flexibility in choosing its value for other objectives. The uniformity constraint on H/R is important and the fixed value aids higher collection efficiency and increasing to an even higher value is discredited by free jet expansion considerations (Section 4.4.7) and size dependence (Section 4.4.4).

(a)

(b)
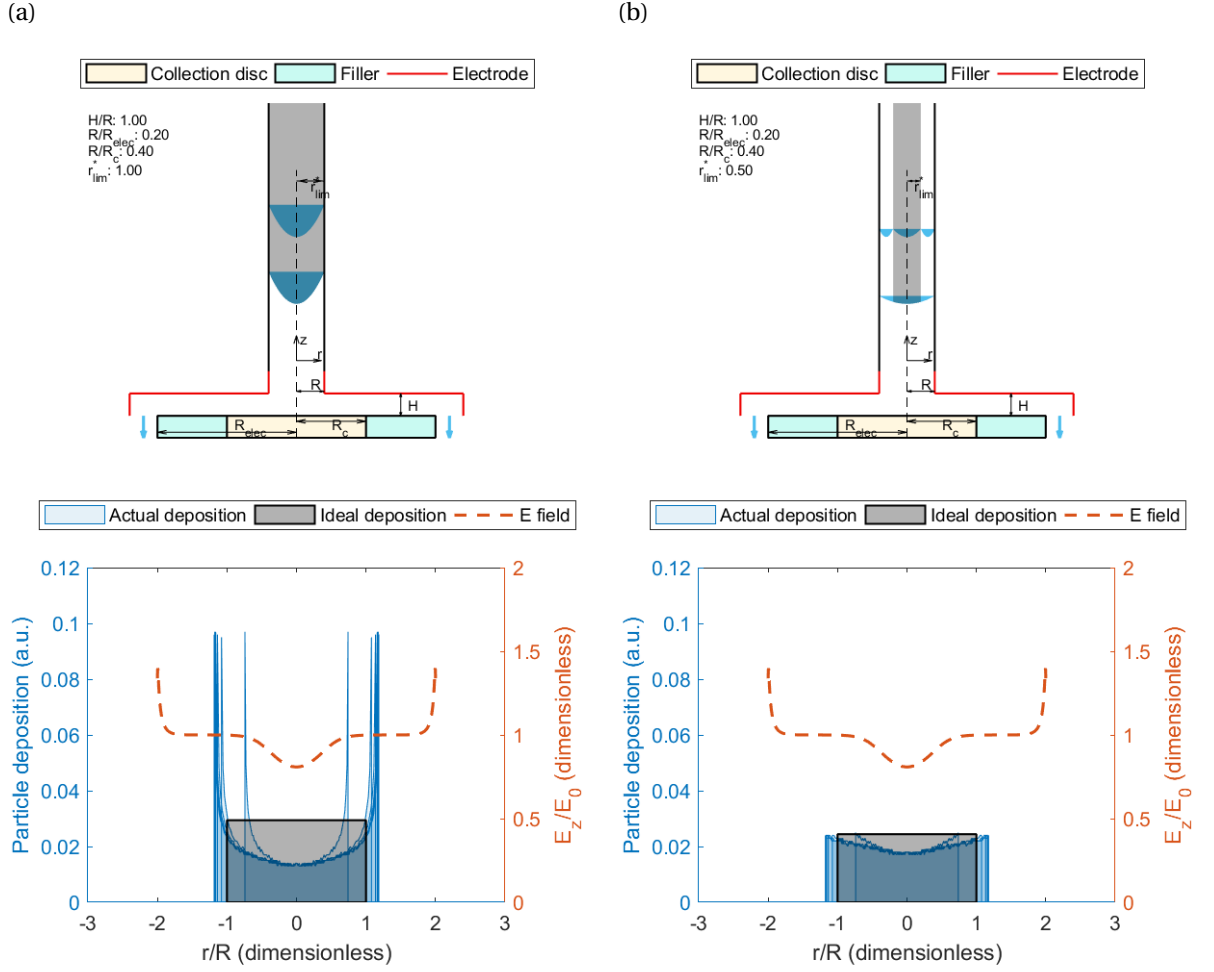
Figure 4.1: Effect of changing sheath position (r^*_{lim}) on the collection profile and spatial uniformity of deposition. (a) $r^*_{lim} = 1$ (b) $r^*_{lim} = 0.5$. The top half shows the device schematic with the axial velocity flow profiles of both particle and sheath streams illustrated, and the geometric lengths and ratios mentioned. The bottom half is aligned with the top-half and shows the COMSOL Multiphysics simulation of the electric field strength and of the particle tracing simulation for selected particle diameters (100 nm to $2.5\mu m$ spaced by 400 nm), and the ideal deposition profile for reference.

4.4.1.3   Geometry: R/R_{elec} - Ratio of the inlet tube radius to the base electrode

The electric field at the edge of the electrode increases to level which is much higher than the designed E_0 because of electric field concentration at the edges of the base electrode. The effect is seen in each E_z/E_0 curve in the bottom-half of Figures 4.1 and 4.3. The high change causes the particle collection to be non-uniform in the region where the electric field is changing. Hence, the end of the base electrode should be kept further outward from the collection region. The electric field concentration effect is dependent on the ratio of the inlet
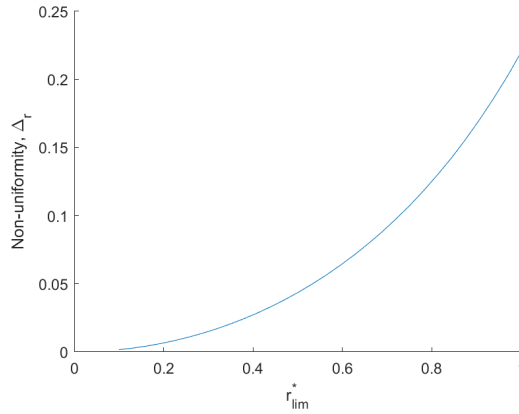
Figure 4.2: Change in non-uniformity because of sheath, $\Delta_{r,r^*_{lim}}$, against different values of the sheath position (r^*_{lim}).

tube radius and the size of the base electrode, R/R_{elec} (the Figure 4.5) where the normalized electric field against r/R is plotted at a fixed $H/R = 0.5$ at $z = 0$. The concentration effects of the changing electric field for $R/R_{\mathrm{elec}} > 0.5$ is so strong that it alters the expected radial electric field distribution for the example in Figure 4.5 at $H/R = 0.5$. Values of $R/R_{\mathrm{elec}} \leq 0.5$ is hence required as it reduces the effect of R/R_{elec} on the electric field strength, thus resulting in the variation from H/R becoming the key controlling factor. The set limit on R/R_{elec} aligns with the requirement for low size dependence (Section 4.4.2).

For reasons similar to that above, the electrode surface should also be kept further away from the collection surface R_c. Thus, in addition to the requirement $R/R_{\mathrm{elec}} \leq 0.5$ we also consider $R_c//R_{\mathrm{elec}} \leq 0.5$. These constraints are combined into a single one that determined the electrode size, $R_{\mathrm{elec}} \geq 2R_c \max(R/R_c, 1)$.

4.4.2 Effect on low chemical-interference

Chemical-interference is reduced by reducing the chances of free radical formation because of electrical parts and by keeping the particles farther away from regions where any such formation is plausible. As such, E_0 and V_0 become they key parameters in achieving the objective but some variables can also help in achieving the objective. Concurring with the requirement of r^*_{lim} (Section 4.4.1.1) and R/R_{elec} (Section 4.4.1.3) for high spatial-uniformity, lower r^*_{lim} keeps particles further away from the high voltage on the ring electrode in the tube and the top electrode; and $R/R_{\mathrm{elec}} \leq 0.5$ keeps the region of field concentration far from deposition area. (Jodzis and Patkowski, 2016) have shown that any ozone produced between electrodes has a hyperbolic concentration profile which decreases further away from the discharge electrode making r^*_{lim} beneficial to lowering chemical interference. Even if the design E_0 is such that chemical interference is theoretically low, the sudden increase in electric field strength values at the edges of the base electrode for $R/R_{\mathrm{elec}} > 0.5$ is undesirable because

(a)

(b)
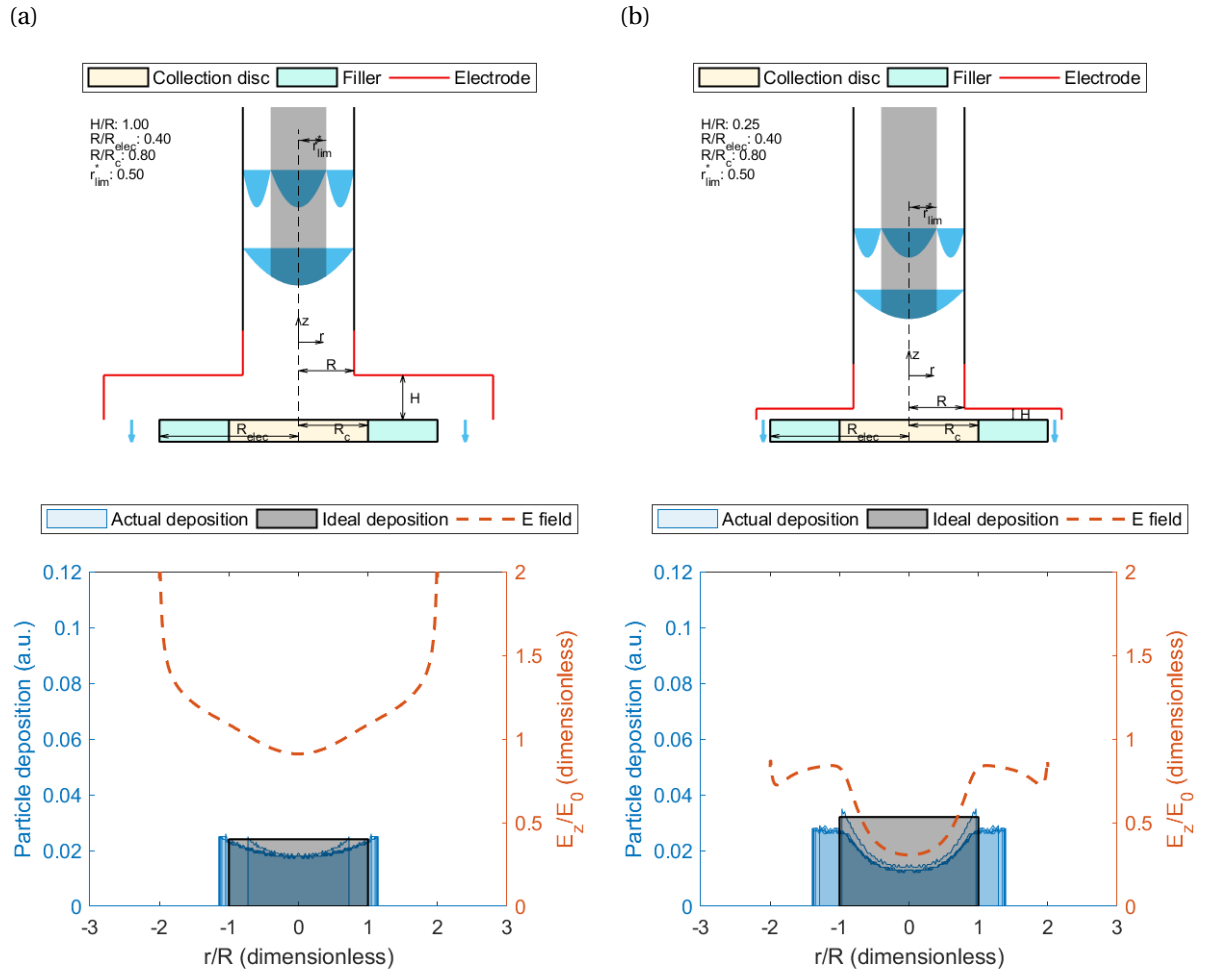
Figure 4.3: Effect of changing H/R on the collection profile and spatial uniformity of deposition. (a) $H/R = 1$ (b) $H/R = 0.25$.

it might result in possible chemical modification.

4.4.2.1 Operating condition: E_0 - electric field strength

Very high electric field strengths are undesired as chemical interference can increase through generation of reactive free radicals that react with the particles. The electrical breakdown of air (the working fluid) is around 3 kV/mm though some studies have calculated streamer discharge onset from 2.28 kV/mm (Heiszler, 1971). The average electric field strength is the ratio of the applied voltage (between the top electrode and the top surface of the collection surface) and the separation distance, but edge effects (discussed in Section 4.4.1.3) can enhance the local electric field strength values. Keeping a factor of safety (FoS) of 1.15 (assessed according to equation 12.1 (Jack, 2013) by assuming 15% statistical variability in design, 100%
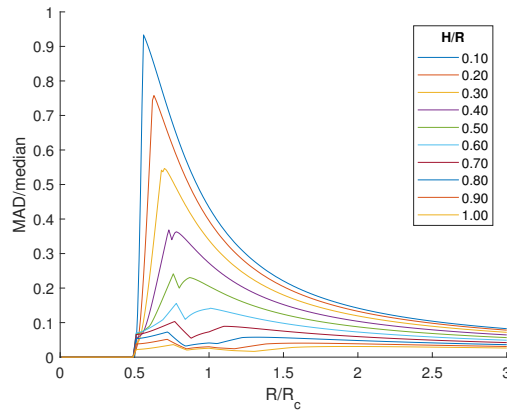
Figure 4.4: Change in electric field nonuniformity, Δ_{D_p} over r in $[0, R_c]$ for different H/R (legends) and R/R_c (abscissa) values.
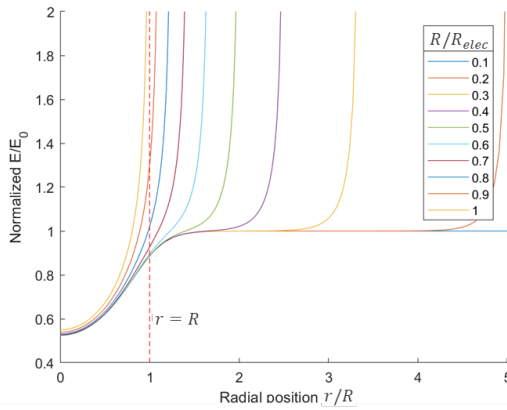
Figure 4.5: Effect of R/R_{elec} on the electric field strength over and around the collection disc for a fixed $H/R = 0.5$.

pre-knowledge of the design subject and a 0% hazard of failure as there are no lethal implications of failure) it would be preferable to maintain $E_0 < 2kV/mm$ and using FoS of 2.3 (using 50% knowledge instead) we formulate a lower limit of $E_0 > 1$ kV/mm. Lower E can be employed for special applications where the corresponding reduction of collection efficiency and overall collection flux is not against the design objective.

4.4.2.2   Operating condition: V_0 - High voltage at the electrode

Apart from an electrical discharge stemming from the local electric field strength, there are a few processes which also limit the voltage directly, to a degree. For example, Trichel discharge from generally sharp electrodes with high negative potential or streamer discharge from electrodes with high positive potential have similar onset conditions (Rees, 1973). Trichel discharge has been shown to have lesser dependence on the separation distance and an onset

from above 10 kV in magnitude. For these reasons the chances of chemical modification are reduced when operating the device such that no electrode has an absolute voltage higher than 10 kV i.e. $|V_0| \leq 10kV$.

4.4.3   Collection efficiency

Collection-efficiency (η) is the fraction of particles deposited on the collection surface with radius (R_c). For the special case of a spatially uniform deposition the efficiency becomes equal to the ratio of the area of the collection surface (A_{ref}) to the hypothetical disc area where the particles would have deposited if the surface had an infinite radius ($A_{deposit}$). When $A_{deposit}$ is smaller than A_{ref} the ratio is smaller than one but inherently efficiency is defined to be limited to a maximum 1. Hence the area ratio ($A_{ref}/A_{deposit}$)is used in many places in the document to avoid discontinuity for $A_{ref}/A_{deposit} > 1$.

Understanding the relationship of Q_a and E_0 is fairly straight-forward with respect to η. A higher flow rate, Q_a will result in lower η as the particles would drift less in the inlet tune and will travel further out in the collection zone. At a fixed Q_a, higher E_0 will result in a smaller deposition area and consequently a higher η, but the limits of E_0 is dictated by chemical-interference considerations (Section 4.4.2.1) and is dependent on the R/R_c (Section 4.4.6.1). Related to the effect of E_0 is that of reducing H/R which also lowers the E under the inlet tube (Figure D.3, lower half). Not only does that reduce introduce non-uniformity (Section 4.4.1.2) but also the overall average E for collection.

4.4.3.1   Inlet condition: n - Charge

The charger used for the design is a 3D-printed reconstruction of the charger published as a part of a bio-aerosol sampling device that has low ozone generation (T. T. Han, Thomas, and Mainelis, 2017). Any charger that charges the particles using field charging/ diffusion charging/ UV charging can be used, provided the ozone generation is low. In the design analysis it has been assumed that 1 elementary charge per 20 nm diameter is present as it aligns well with the observed collection-efficiency in some preliminary experiments.

4.4.3.2   Geometry: $r_{geo}^{\dagger}$ - $(R/R_c)r_{lim}^{*}$

Figure 4.6a shows the change in efficiency ($A_{ref}/A_{deposit}$) against $r_{geo}^{\dagger}$. Even for different R/R_c the overall trend is proportional to $r_{geo}^{\dagger}$ alone, though there are some deviations as represented by the tails extending away from the line, mainly for higher r_{lim}^{*}. For uniformity requires $r_{lim}^{*} \leq$ 0.4 already, these deviations do not have much effect and for the given geometry at $Q_a = 1.75$ LPM, the efficiency is higher for lower $r_{geo}^{\dagger}$. The resulting requirement is in accordance with the requirement for higher collection flux but in contrast to lower size dependence, the trade-off of which is discussed in Section 4.4.5.2.

(a)

(b)
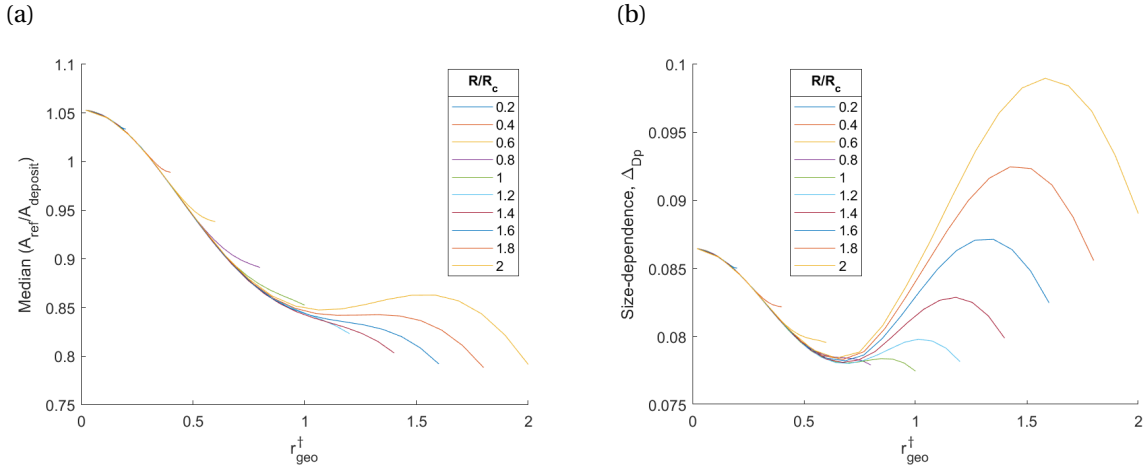
Figure 4.6: Effect of changing $r_{geo}^\dagger$ on (a) final collection area ratio, $A_{\text{ref}}/A_{\text{deposit}}$ (related to η), and (b) final size-dependence, Δ_{D_p}, for a fixed aerosol flow rate $Q_a = 1.75$ LPM and a sheath flow rate changing according to $Q_s = Q_a \frac{1}{r_{lim}^{*2}(2-r_{lim}^{*2})} - 1$ where r_{lim}^* in$[0,1]$ and $r_{geo}^\dagger$ in$[0, R/R_c]$.

4.4.4 Size dependence

Size dependence, Δ_{D_p} does not have a clear monotonic relation with most of the design variables. The reason is that two effects change the size-segregation with both acting stronger on particles with higher electrical mobility. At low flow rates, particle drift in the inlet tube dominates while the electrostatic force in the collection is the major contributor to size-stratification at higher flow rates. The trade-off is also dependent on geometry for drift in the inlet tube (Appendix D.3 Figure D.1b) and for the dispersion in the collection region (Figure D.2b). The combined overall size dependence is discussed in Section 4.4.4.1, and is also dependent on the flow (Section 4.4.4.2) and as Q_a/E_0 ratio is present in all the equations in Table 4.1, reducing E_0 by a factor has mathematically the same effect as increasing Q_a by the same factor. The dependence on H/R is to a small extent, and Δ_{D_p} decreases with lower H/R (Appendix D.4, Figure D.3b). As the contribution of H/R does not change Δ_{D_p} by a large factor (as does $r_{geo}^\dagger$ or Q_a) and stands in opposition to the requirement of H/R for high spatial-uniformity (Section 4.4.1.2) and collection efficiency (Section 4.4.3), it has been not considered as a major variable for reducing Δ_{D_p}. However, it also motivates not increasing H/R to a very large number ($\gg 1$) besides other considerations motivating the same consideration (Section 4.4.7).

4.4.4.1 Geometry: $r_{geo}^\dagger$ - $(R/R_c)r_{lim}^*$

Overall size dependence (Figure 4.6b), results from opposing effects of the drift in the inlet tube and the particle movement in the collector region. For $r_{geo}^\dagger < 0.6$, the size dependence decreases with increasing $r_{geo}^\dagger$. For $r_{lim}^* < 0.4$, as required for spatially uniform deposition,

the size dependence decreases with increasing R/R_c for a fixed r^*_{lim} until $R/R_c < 1.5$ (corresponding to $r^\dagger_{geo} = 0.6$). Hence, a higher $r^\dagger_{geo}$ is useful for reducing the size dependence but this stands in contrast to the requirements for high collection efficiency (Section 4.4.3.2) and high collection flux (Section 4.4.5.2). The trade-off is evaluated in Section 4.4.5.2 and the exact value is fixed based on some additional considerations in Section 4.4.6.1.

4.4.4.2 Operating condition: Q_a - Aerosol flow rate

Figure 4.7a shows the changing Δ_{D_p} when operating at a fixed flow rate of $Q_a = 1.75$ LPM. For a given particle-size-range however, the overall size-dependence decreases with increasing flow rate for a given geometry $r^\dagger_{geo}$ (Figure 4.7b (bottom-panel)) for $r^\dagger_{geo} = 1.22$ and $r^*_{lim} = 0.4$. The corresponding $r_{f,\max}/R_c$ for different D_p and Q_a is shown in Figure 4.7b, (top panel), which marks the cut-off flow rate for $\Delta_{D_p} = 0.1$ with a green and a red dotted vertical line, for size-dependence calculated based on the Δ_{D_p} for log-uniform distribution of particle number or that of particle mass, respectively for a given particle size range. The difference in the Q_a cutoff for the two basis is negligible, as also seen by overlapping Δ_{D_p} lines in Figure 4.7b (bottom panel) because the D_p distribution was log-uniform. Using either basis there is hence a single lower flow-rate limit for a given $r^\dagger_{geo}$, above which the size-dependence is acceptable as $\Delta_{D_p} < 0.1$. However, the flow rate cannot be indiscriminately increased as the collection efficiency and collection flux are both adversely affected, a trade-off discussed in Section 4.4.5.1. The lower flow-rate limit is also dependent on the particle-size-range and the resulting analysis can change substantially.
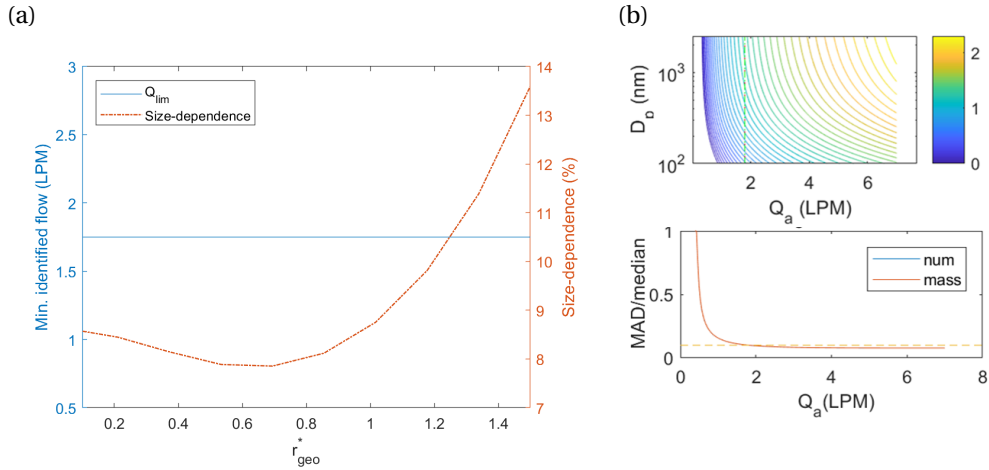
Figure 4.7: (a) Change in size-dependence, Δ_{D_p} for a fixed $Q_a = 1.75$ LPM and $r^*_{lim} = 0.4$. (b) (Top-panel) Contour plot of $r_{f,\max}/R_c$ for different D_p and Q_a, and (bottom-panel) the resulting changing Δ_{D_p} vs. Q_a, for a fixed $r^\dagger_{geo} = 1.22$ and $r^*_{lim} = 0.4$. The vertical dotted line in the top-panel represents the minimum flow rate where the size-dependence is low, as represented by the horizontal dotted line in the bottom-panel.

4.4.4.3 Particle: D_p - Particle size distribution

Apart from particle size range which can affect the analysis of Q_a in section 4.4.4.2, the size-distribution within the range will also change Δ_{D_p}. The analysis of size-dependence has been done on the basis of a log-uniform distribution between $100nm \leq D_p \leq 2.5\mu m$, because it represents the log-spaced particle sample for the size-range and brings out a worst-case-scenario of Δ_{D_p} for a given size-range allowing an analysis without assuming a distribution. The effect of change in particle-size-distribution is presented here. Most practical applications have a log-normal particle size-distribution within the given range with a count mean diameter (CMD), and a geometric standard deviation (σ_g). For the case of $r^*_{lim} = 0.4$, $R/R_c = 0.4$ and $Q_a = 1.75$ LPM, Figure 4.8 shows the median $A_{ref}/A_{deposit}$ and Δ_{D_p} contours for different CMD and σ_g values. Δ_{D_p} is much lower than 0.1 for almost all distributions and lower than 0.05 for most combinations. It is also systematically lower for a higher CMD and lower σ_g. The analysis allows better estimates of Δ_{D_p} for a given distribution or choosing a specific size distribution, if possible, for an application where stricter constraints on Δ_{D_p} is required.

(a)   (b)
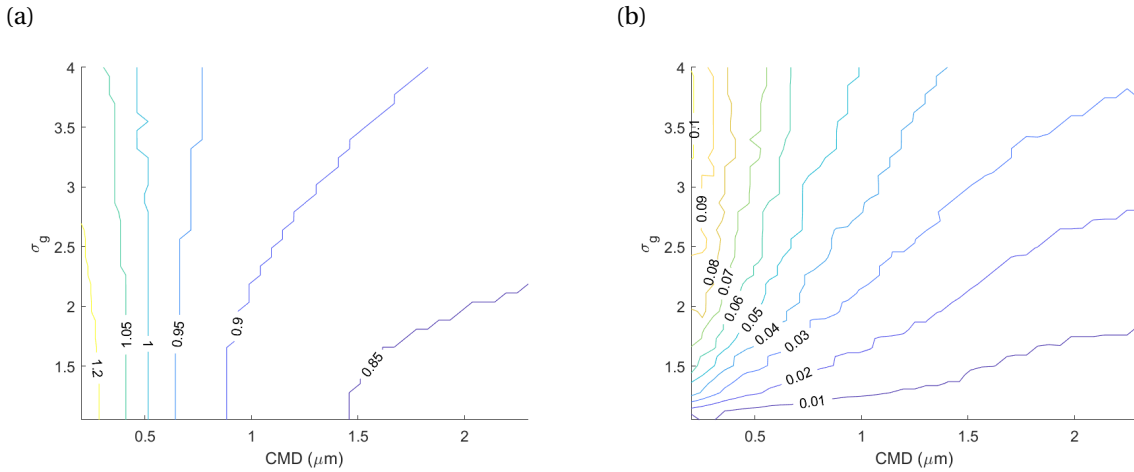
Figure 4.8: (a) Median $A_{ref}/A_{deposit}$ contours and (b) Δ_{D_p} contours, for log-normal distribution of 1000 particles for different combinations of count mean diameter(CMD) and geometric standard deviation (σ_g) .

4.4.4.4 Inlet condition: n - Charge

The number β is also expressed in terms of the electrical mobility, Z_p (equation 4.1).

$$\beta = \frac{e}{3\pi\mu Z_p R_c} \tag{4.1}$$

A design targeted at a particular mobility-size range (D_p range) translates into a corresponding range of mobilities (Z_p range) for an assumed charge level ($n(D_p)$) and calculated slip factor ($C_c(D_p)$). The relation allows evaluating the deviation in acceptable charge levels such that a

particle with a given D_p still is within the design Z_p. For example, we analyze the deviation for an expected charge level n that is proportional to D_p such that $n = 5(D_p(nm)/100)$ i.e. 5 elementary charges are present on a 100 nm particle, as expected from diffusion charging alone (e.g. for (Biskos, Reavell, and Collings, 2005)). The expected charge is higher for larger particles for a combination of field and diffusion charging (Marquard, 2007) (e.g. (Kaminski et al., 2012)). For a size range of D_p in [100nm, 2.5μm] corresponds to Z_p in [4.9, 13.3] $\times 10^{-8}(\mathrm{m^2V^{-1}s^{-1}})$. The charge levels for a D_p that would be within the intended Z_p range have a large margin - 0.5 to 2 times that of the starting value (Figure 4.9). The mobility diameter (D_p) in the ESP should be converted to the volume-equivalent diameter ($D_{\mathrm{p,ve}}$) (DeCarlo et al., 2004) for evaluating congruence with inertial devices (e.g. cyclones).
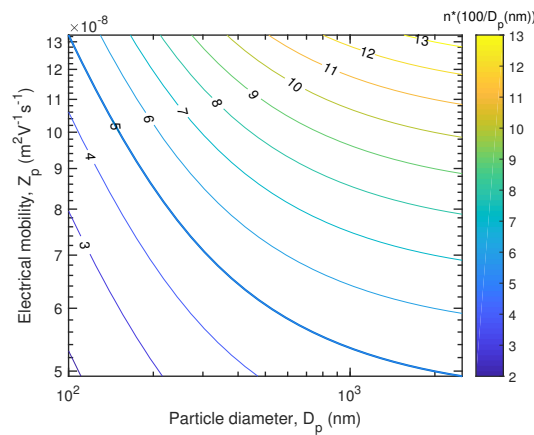
Figure 4.9: Range of the number of elementary charges (n) on a particle with mobility diameter D_p falling within a range of electrical mobilities (Z_p).

4.4.5 Collection flux

The volumetric collection flux of the system defines the overall throughput of the collector. It is equal to the ratio of the aerosol flow rate (Q_a) and the area of the disc where the particles are deposited (A_{deposit}) which can be smaller or larger than the area of the collection disc (A_{ref}). Higher flux not only reduces the time to collect enough particles to make a confident measurement but also ensures that more particles are collected on a given area. Moreover, for a spectroscopic system, the product of the volumetric-flux $[LT^{-1}]$ with the ratio of particle mass concentration $[ML^{-3}]$ to particle's material density $[ML^{-3}]$, corresponds to the rate of increase of the effective depth of particle film per unit time. It becomes a useful measure for the mass collection on the surface as it represents the effective depth (or length) in a Bouguer-Lambert-Beer-type model and would scale linearly with collection time.

4.4.5.1 Operating condition: Q_a - Aerosol flow rate

Increasing Q_a increases A_{deposit} and if it exceeds A_{ref}, the efficiency starts decreasing below 1 and, as discussed, iff the deposition can be considered as uniform, $\eta = A_{\text{ref}}/A_{\text{deposit}}$. Just as Figure 4.7b shows the lower flow-rate limit for $r^{\dagger}_{geo} = 1.22$, Figure 4.10a shows different lower flow rate limits (labeled Q_{lim}) for different $r^{\dagger}_{geo}$ values at a fixed $r^{*}_{lim} = 0.4$ for which $\Delta_{D_p} = 0.1$. The corresponding normalized deposition area, $A_{\text{deposit}}/A_{\text{ref}}$ is labeled "Normalized deposition area" and the ratio of the two $Q_{lim}(A_{\text{ref}}/A_{\text{deposit}})$ is labeled by the same name. The ratio is akin to deposition-flux ($\varphi = Q_a/A_{\text{deposit}} = Q_{\text{lim}}(A_{\text{ref}}/A_{\text{deposit}})/(\pi R_c^2)$), but by using the prior form it has the same units as flow rate. As the ratio is nearly a constant, the deposition volume flux (φ) is also nearly a constant over different $r^{\dagger}_{geo}$ if $\Delta_{D_p} = 0.1$.

In actuality though operating the device with $A_{\text{deposit}}/A_{\text{ref}} < 1$ is sub-optimal and in those cases operating with a higher flow rate such that $A_{\text{deposit}}/A_{\text{ref}} = 1$ (i.e $\eta = 1$) is desirable, as in Figure 4.10b ("Flow Q_a"). With these conditions the operating flow is higher of the two: that which is required for $\eta = 1$ or that for $\Delta_{D_p} = 0.1$. The result flow rate is the higher flow limit in most cases, as increasing the flow rate any further (at a fixed E_0) would reduce η. The resulting effect as seen in the Figure, is that the collection-flux is higher for $r^{\dagger}_{geo} < 1$ (corresponds with the range that has $\eta = 1$). Concurrently, Δ_{D_p} no longer stays at 0.1 as was the case in Figure 4.10a, but changes as shown in Figure 4.10b ("Size-dependence Δ_{D_p}(%)") which enumerates the trade-off between size dependence and collection flux for $r^{\dagger}_{geo} \leq 0.6$ where higher volume flux (favorable) also has a higher size dependence (unfavorable). All the calculations are done for $E_0 = 1$ kV/mm and $n/D_p = 1/20$ nm, and doubling either of the values will directly double the Q_a, as both the drift and collection equation uses $\alpha\beta$ in the equation (and $\alpha \propto Q_a/E_0$; $\beta \propto D_p/n$) in their equations.

The near constant φ_{const} in Figure 4.10a, stays exactly the same over different R_c magnitudes and nearly the same over different r^{*}_{lim} values (Appendix D.6 Figure D.2). The maximum flux at $\lim_{r^{\dagger}_{geo} \to 0} \varphi = \varphi_{\text{max}} \approx 1.19\varphi_{\text{const}}$ and stays exactly the same for different R_c and r^{*}_{lim} values (Appendix D.6 Figure D.1).

$$\varphi_{\text{const}} \approx 0.3058 \left(\frac{E_0}{1\text{kV/mm}} \right) \left(\frac{n/D_p}{1/20\text{nm}} \right) \text{LPM/cm}^2$$

.

These flux values allow estimating the operating aerosol flow rate Q_a for different geometries. For example, to operate at 95% of the maximum flux, $\varphi = 0.95\varphi_{\text{max}}$ with $r^{*}_{lim} = 0.4$, we get $Q_a = 1.75$ LPM at $E_0 = 1$ kV/mm. The other values of Q_a for different E_0 is shown in Section 4.4.6.1.
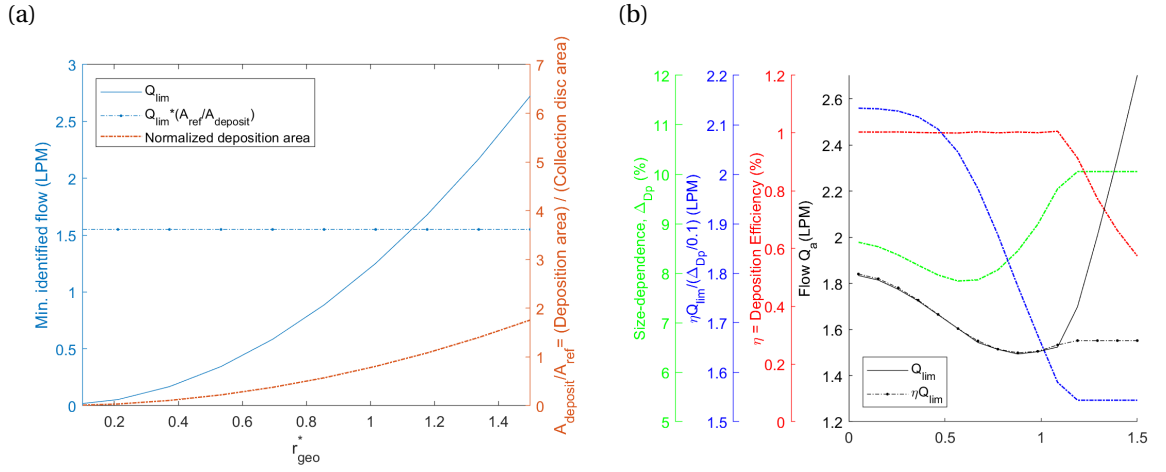
Figure 4.10: (a) Change in the minimum flow rate (left y-axis) as a function of $r_{geo}^{\dagger}$ for maintaining $\Delta_{D_p} \leq 0.1$ at $r_{lim}^{*} = 0.4$. The final deposition area can be smaller or larger than the collection disc size and this normalized collection spot area is shown on the right y-axis. By dividing the flow rate with its spot area we get the flux representation (dotted horizontal line). (b) The "Flow Q_a" y-axis (from the right) represents the flow rate (solid-line) and flux representation (dotted-line) similar to that in part a, with the difference that the flow rate is increased for regions where $A_{\text{ref}}/A_{\text{deposit}} < 1$ till the ratio becomes 1 (represented by "η" y-axis). The changed size-dependence from 10% is shown in the "Size-dependence, Δ_{D_p}" y-axis. The ratio of the flux representation ηQ_a and normalized-size-dependence $\Delta_{D_p}/0.1$ is shown in the "$\eta Q_a/(\Delta_{D_p}/0.1)$" y-axis.

4.4.5.2 Geometry: $r_{geo}^{\dagger}$ - $(R/R_c)r_{lim}^{*}$

In Figure 4.10b ("Flow Q_a" y-axis), the region corresponds with higher collection-flux (labeled "ηQ_a") has a trade-off between collection-flux (represented by ηQ_a), which is highest at $r_{geo}^{\dagger} = 0$, and size-dependence ("Δ_{D_p}"), which is lowest at $r_{geo}^{\dagger} \approx 0.6$ (similar to the limits in Figure 4.6b and Figure 4.7a). In order to evaluate the trade-off, Figure 4.10b ("$\eta Q_{lim}/(\Delta_{D_p}/0.1)$") plots the ratio of the flux representation (ηQ_a) to the size-dependence (Δ_{D_p} normalized by the reference, 0.1), a ratio whose higher-value would mean a beneficial trade-off point. As it emerges the ratio is nearly a constant for $r_{geo}^{\dagger} < 0.4$.

4.4.6 Reynolds number (Re) and Stokes number (St) limits

The analytical model derivation assumes a laminar flow and no impaction effects i.e. $Re < 1800$ and $St < 0.1$ (for less than 1% impaction (Rader and V. a. Marple, 1985)). With the respective equations 4.2 and 4.3, the limits result in an upper bound and a lower bound on R_c as a function of R/R_c for a given value of r_{lim}^{*} (Figure 4.11) for $r_{lim}^{*} = 0.4$. The lower limit on R_c from St is not as imposing as the upper limit from Re, but is increasingly important for smaller r_{lim}^{*} as shown in Appendix D.5, Figure D.1 for $r_{lim}^{*} = 0.1$ to 0.5.

$$Re = \frac{4\rho_{\text{air}}Q_{\text{tot}}}{\pi\mu D}; \quad St = \frac{4\rho_{\text{air}}C_c D_p^2 Q_{\text{tot}}}{9\pi\mu D^3}$$

$$\text{where, } Q_{\text{tot}} = \frac{\pi\varphi R_c^2}{r_{lim}^{*\,2}\left(2 - r_{lim}^{*\,2}\right)}; \quad D = 2R_c\left(\frac{R}{R_c}\right)$$

Here, $\varphi = 0.95\varphi_{\max}$ which corresponds to $Q_a = 1.75$ LPM for $R_c = 12.7$ mm, $E_0 = 1$ kV/mm and $n/D_p = 1/20$ nm.

$$R_c < 1800\frac{\mu(R/R_c)r_{lim}^{*\,2}\left(2 - r_{lim}^{*\,2}\right)}{2\rho_{air}\varphi} \tag{4.2}$$

$$R_c > \frac{1}{0.1}\frac{\rho_{air}C_c D_p^2\varphi}{18\mu(R/R_c)^3 r_{lim}^{*\,2}\left(2 - r_{lim}^{*\,2}\right)} \tag{4.3}$$
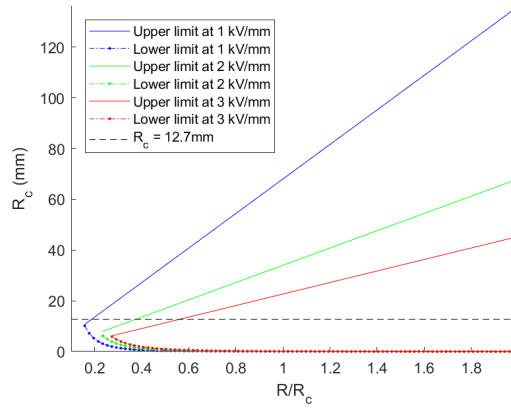
Figure 4.11: If the operating Q_a is derived from the operating $\varphi = 0.95\varphi_{\max}$ then the upper and lower limits on collection disc size (y-axis) over which the FIR-model would be valid for different R/R_c values (x-axis) for sheath positions, $r_{lim}^* = 0.4$, with a horizontal line at $R_c = 12.7$ mm for reference. The limits are different for different E_0 as φ and hence Q_a scales proportionally.

4.4.6.1   Geometry: R/R_c and r_{lim}^* - Ratio of the inlet tube radius to the characteristic radius and sheath flow position

Figure 4.11 labels the limits for arbitrary E_0, however, the maximum E_0 varies with R/R_c with a parallel constraint from the upper limit on $V_0 = 10$ kV (in Section 4.4.2.2) and $H/R = 1$ (in Section 4.4.1.2) (Figure 4.12a (left y-axis)). The graph is limited to $E_0 \le 2$ kV/mm (using the upper limit in Section 4.4.2.1) and a reference horizontal line is drawn at the preferable lower limit of $E_0 = 1$ kV/mm. Hence at $R_c = 12.7$ mm and $r_{lim}^* = 0.4$, for $E_0 > 1$ kV/mm, we should maintain $R/R_c \le 0.8$. At a given R/R_c, when operating at the maximum E_0 (up to a further

maximum of 2 kV/mm) according to Figure 4.12a (left-axis), Q_a will be higher by the same proportion without affecting the performance, as shown on the same figure's right-axis. When operating at the higher Q_a there exists a lower r_{lim}^* limit below which $Re > 1800$ (so not certain to be a laminar flow) (Equation 4.4).

$$r_{lim}^{*}{}^{2}\left(2 - r_{lim}^{*}{}^{2}\right) < \frac{1}{1800}\frac{2\rho_{air}Q_a}{\pi\mu R_c(R/R_c)} \tag{4.4}$$

The corresponding lower r_{lim}^* vs. R/R_c curve is shown in Figure 4.12b, which empirically falls in-line with approximately the hyperbola, $r_{geo}^\dagger = (R/R_c)r_{lim}^* \approx 0.15$. The operable pair of values of $(R/R_c, r_{lim}^*)$ is additionally bounded by $E_0 > 1$ kV/mm (corresponding to $R/R_c \approx 0.8$ as shown in Figure 4.12a (left y-axis)) and by the desired sheath flow, $r_{lim}^* \leq 0.4$ (Section 4.4.1.1). *Any pair of points $(R/R_c, r_{lim}^*)$ in the operable region* will be acceptable according to the set design objectives.

(a)   (b)
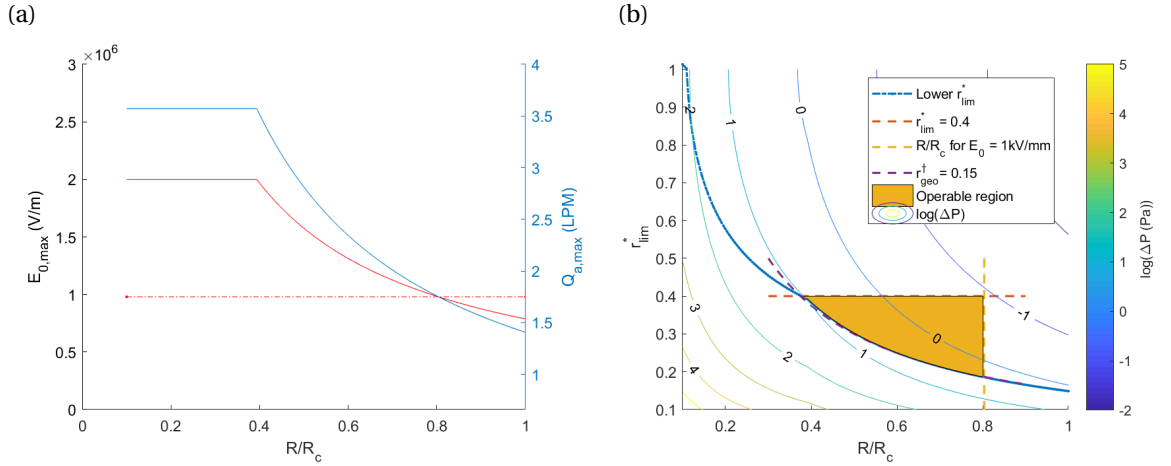
Figure 4.12: (a) Upper limit on E_0 (left y-axis)for different R/R_c based on the limit on voltage, $V_{max} = 10kV$ and $H/R = 1$ along with the corresponding upper limit on Q_a (right y-axis) for $\varphi = 0.95\varphi_{max}$. (b) Lower limit on r_{lim}^* for different R/R_c (thick blue line) when operating at the Q_a limit in part a along with the requirement of $Re \leq 1800$. Along with the limit on $r_{lim}^* \leq 0.4$ and that on R/R_c corresponding to $E_0 > 1$ in part a, the bounded operable region for $(R/R_c, r_{lim}^*)$ is also shown. The skin-friction related pressure loss in the inlet tube length as required for flow development (Section 4.4.7.1) is represented as contours of the order-of-magnitude, $log(\Delta P(Pa))$.

Fixing a particular R/R_c value will allow a possible range of operation for r_{lim}^*. As r_{lim}^* is not physically constrained or hard-built into the device, but is a result of the inlet aerosol and sheath flow, it can be changed by adjusting the sheath flow, Q_s such that $Q_{tot} = Q_s + Q_a = \frac{Q_a}{r_{lim}^{*}{}^{2}(2-r_{lim}^{*}{}^{2})}$ for the operating Q_a, up to the maximum Q_a in Figure 4.12a (right y-axis) for any fixed R/R_c.

4.4.7 Other practical considerations

Values of $H/R \gg 1$ require consideration of free-jet-expansion physics (Bergthorson et al., 2005; Bühler, Obrist, and Kleiser, 2014) which is not part of the analytical model. As a first principle analysis, the free jet expansion would result in the particles moving further outward and introduces another mechanism than can alter the size dependence and add complexity for prediction. Some other considerations of flow development length and pressure drop related to skin friction in the development tube is shown in the subsequent sections.

4.4.7.1 Inlet condition: r^*_{lim} - Sheath flow position

Lower values of r^*_{lim} will also increase the pressure drop as Q_{tot} increases (Figure 4.12b) where the pressure drop is from the skin friction calculated in the development tube, using the Darcy-Weisbach equation (Weisbach, 1845). Thus, initially keeping r^*_{lim} at the higher limit of the operable region in Figure 4.12b, i.e. $r^*_{lim} = 0.4$ is good. Another factor for consideration is that reducing r^*_{lim} increase length of development of the combined aerosol and sheath stream into a parabolic-flow. As D in Re's denominator and in $L/D = 0.055Re$ (Christiansen and Lemmon, 1965) cancel out, so L is not dependent on R/R_c but on r^*_{lim}). Very long tubes are undesirable as the chances of a problem/ damage to the system over time become higher. For $r^*_{lim} = 0.4$, L becomes 45 cm, which is already very high. Based on COMSOL simulations, we set $L = 30cm$ where the center-line velocity becomes 95% of the theoretical value instead of 99% as required by "fully-developed". The resulting reduction in development length is around 40% and is important to reduce the total volume of air column with particle which can have its own artifacts and to reduce chances of large eddy formation, as the probability of a surface irregularity reduces by that much. The equation for 95% center-line velocity ($L/D = 0.034Re$) is predicated on that for a sharp-edge inlet (Emery and C. S. Chen, 1968) and some new analysis (Poole, 2010) also gives similar L values. Evaluations by (Fargie and B. W. Martin, 1971) also show that the formula can be more relevant for pressure drop (and friction coefficient) analysis than the 99% formulas. The sharp-edge inlet is similar to the case in this work and both have a decelerating center-line velocity rather than an accelerating one, common to fully developed flow length calculations. Moreover, as we have an annulus around, the deceleration is by a lesser amount, so the limit can be treated as an upper bound.

4.4.7.2 Geometry: R/R_c - Ratio of the inlet tube radius to the characteristic radius

R/R_c has to be larger than typical IR beam size to counter the possibility of any unexplored edge effects/material chip-off/ electrode degeneration over time at the tube edge. In similar manner, it has to be smaller than the collection surface to prevent any edge effects from the collection substrate. So $R > 7.5$ mm (the beam radius of a potentially employable IR-equipment) and $R < 12.7$ mm. The limits correspond to $0.6 < R/R_c < 1$ for $R_c = 12.7$ mm. Lower R/R_c is associated with a higher pressure drop as shown in Figure 4.12b, where the pressure drop is calculated for the skin friction is calculated in the development tube. As even

the higher pressure drop is not unachievable though small vacuum pumps it is not considered as a limitation on design, but lower pressure drop is more favorable to preserve lower volatility compounds for a longer time on the collection surface.

4.5   Conclusions

We present a method for designing a two-stage radial ESP that aims at collecting poly-dispersed aerosol for quantitative measurement of chemical composition using IR-spectroscopy. A set of five design objectives are relevant to a device that performs particle collection through ESP, subsequent measurement through transmission IR spectroscopy and with other considerations for reducing chemical or size modification in collection, and increasing the overall device throughput to achieve faster collection. High spatial uniformity requirements dictates that higher $H/R \approx 1$ be used along with a lower sheath flow position, $r^*_{lim} < 0.4$. The base (collection) electrode should be atleast twice as large as the tube inlet or the collection surface. Possible chemical interference of the particles during flow or after collection is reduced by lowering the applied voltage $V_0 < 10$ kV and resulting electric field strength $E_0 < 2$ kV/mm. A lower Q_a, higher E_0 and higher number of elementary charges on the particle increases the collection efficiency of the device. A smaller apparent inlet position, $r^{\dagger}_{geo}$ causes a higher collection efficiency but at the loss of higher size-dependence in collection. The overall-size dependence is a combination of that caused because of particle drift in the inlet tube and that in the collection region. The resulting size-dependence is lower for higher flow-rates, and for higher $r^{\dagger}_{geo}$ at a fixed flow rate. The trade-off is evaluated using the collection flux as the overall throughput, and using the limits of the analytical model regime (range of Reynolds and Stokes numbers). Laminar flow consideration limits the E_0 and Q_a creating a lower bound on $r^{\dagger}_{geo}$, which in combination with bounds on $r^*_{lim} < 0.4$ and $R/R_c < 0.8$ results in a range of acceptable design geometries.

The work demonstrates a procedure for systematic evaluation of ESP design and operation along pre-defined criteria, which is applied toward improving quantitative capabilities and time resolution of IR spectroscopy on aerosols analyzed via direct collection on an optical substrate. The device and the design technique can find multiple applications in other aerosol measurement methods either directly or with a brief re-analysis for different objective criteria.

5 Conclusion

In this work we evaluated collector designs and explored the design and fabrication of an electrostatic precipitator for improved quantitative measurements of chemical constituents of aerosol using IR spectroscopy. Among the various collector types, ESP emerged as having relevant advantages for the application with radially symmetric ESP having inherently lower dependence on operating conditions and particle properties. We explored and established a method to prototype multiple devices using numerical simulations and 3D-printing, which is advantageous for developing early stage devices without imposing many constraints from the onset. The method was used to fabricate a two-stage ESP collector which was observed to have IR absorbance scale with mass loading, low size segregation and a high collection efficiency. We formulated a method using variable aperture IR spectroscopy (VAIRS) to analyze the surface mass distribution on the collector surface, in addition to an image analysis method which also provided a good estimate of the radially changing effective film thickness. The spatial uniformity was varying within experiments and motivated efforts to develop an analytical model with which surface deposition profile could be computed, without the need of numerical simulations, which are limited in the range of variables it can reliably simulate and has a computational cost involved. We derived a dimensionless analytical model that maps particle each particle position in the inlet tube to a corresponding position on the collection surface, for a two-stage ESP. It was derived using the balance of the drag force and the electrostatic force as the other forces where neglected based them being orders-of-magnitude smaller. The model was derived for a linear translationally symmetric system and a radially axi-symmetric system and the radial system was found to be less sensitive to changes in design variables and having inherently lower size-segregation. For the radial system, the particle drift in the inlet tube contributes significantly to the overall particle deposition dynamics. We derive an equation for the particle drift in the tube by using the linear system model for a radically changing electric field in the tube. The analytical model not only includes the inlet particle position but also includes a general case where a sheath flow around the particle laden stream for a finite inlet radius. We modify the model to make is scalable with respect to the collection disc radius. We identify key geometry and operating parameters and group them into dimensionless terms while rearranging the model and propose 4 new dimensionless

numbers. The ESP operating number includes all the operating parameters, ESP particle number includes all the particle dependent parameters, ESP inlet number denotes the apparent inlet radius and the ESP performance number which is represented by the outermost particle position with respect to the collection disc radius. These are in addition to 2 other geometry terms and a sheath position terms. The model calculations when evaluated against several numerical simulations performs much better for the outermost particle position and has a slight deviation from expected value, mainly because the non-uniformity under the inlet tube induces particle migration to a different degree than that expected from a constant electric field. The electric field non-uniformities are higher for lower H/R ratios. The model, owing to its large range of included variables, allows assessing particle spatial distribution, size stratification, collection efficiency and sensitivity to different parameters. Qualitatively, a larger inlet radius can have lower size stratification for a given particle size range. Interestingly, the spatial distribution of the particles was not the same as the particle velocity distribution upon collection, as previously though and neither was it uniform or top-hat for a parabolic flow inlet with a uniform particle distribution in the inlet. With its large number design variables incorporated the analytical model is useful to evaluate different designs tailored for diverse applications. We identify a set of objectives that for the design goal in this work of a collector that can reliable perform a quantitative measurement of chemical constituents of aerosol with IR spectroscopy. High spatial uniformity, low chemical interference, low size dependence, high collection efficiency and high collection flux are identified as the primary objectives which the collector should achieve. In order to quantitatively analyze the objectives, we define them in terms of the design variables in the analytical model, wherever possible. Collection flux is important as it represents a variable that should higher value amidst the trade-off between collection efficiency and operating aerosol flow rate. Each objective affects the range of appropriate values for some variables and by analyzing the multiple objectives, we identify the design space where the ESP collector should belong. Spatial uniformity requirements dictates that higher H/R values be used along with a sheath position $r^*_{lim} \leq 0.4$. Chemical interference requirements mainly limits the operating filed strength and the operating voltage. There was a tradeoff between size dependence and collection flux over the value of ESP inlet number. Ultimately, the range of operating values of the inlet radius and the sheath position $(R/R_c, r^*_{lim})$ was found to be bound by lower limits on electrical field strength, higher limits on r^*_{lim} which was related to maintaining spatial uniformity and a lower limit on both imposed by the limits of laminar flow. The operating area of the two geometric terms allows for fabricating a number of device geometries. The proposed collector should be tested by collecting a host of different atmospherically relevant materials (organic and inorganic) to evaluate the performance over different materials and combinations. After some testing the device can find applications in many areas. Experiments that use the device for reactive oxygen species (ROS) detection can especially be useful, as ROS has been linked to oxidative stress and other harmful effects to the human body. IR has a unique advantage of detecting peroxide bonds and with the device having high collection flux, it should be able to detect some fraction of the labile compounds within its lifetime. As the device can provide much lower detection limits than conventional Teflon filters, it can be used alongside an IR-spectrometer to make frequent

aerosol composition measurements, for example for ambient monitoring or during chamber experiments where the orthogonal information provided by the IR spectra will be valuable for research. Apart from the device, the analytical model can be employed in designing multiple other devices for separate applications. They can involve substantially different design objectives, making very different conclusion that those in the proposed device. The model is very versatile and by defining the objectives it can be used to design and fabricate other ESP collectors. On the other hand, for existing devices the model can be applied to tune the operating parameters to match the desired performance for different particle properties. Hence, the devices developed in this work has application in aerosol monitoring and scientific research and the methods are employable in aerosol technology for device design and fabrication.

Appendixes Part II

Appendixes Part II

A Types of chargers

Depending on the mechanism that produces the gaseous ions, we can classify a unipolar charger into (i) corona, (ii) ionizing radiation and (iii) photoelectric/ UV- light source Intra and Tippayawong, 2011.

A.0.1   Corona discharge chargers

Corona discharge is extensively used in industrial processes and is an established technique (Hewitt, 1957, 1957). The discharge corona is produced in a non uniform electrostatic field (obtained by using needle/wire to cylinder/plate) and the resulting ions concentration is high in such devices. Incoming air stream is ionized in some regions that has high enough electric field strength. This results in production of ions and electrons that then migrate in the field. These migrating ions/ electrons attach themselves to the incoming particles (through diffusion or electrostatics or both), charging the particles in the process.

A.0.1.1   Hewitt-type corona charger

The earlier designs employed a corona wire at the axis of a cylinder and a coaxial mesh that has an AC voltage applied to it, which helps transport the ions from the ion generation zone to the charging zone. The incoming particles are charged in the charging zone, through combining with these cahrged ions, as shown in figure A.1. A design that uses the above arrangement with sheath air was developed by Liu and Pui, 1975 B. Y. H. Liu and Pui, 1975, as shown in figure A.2.

A significant improvement to this Hewitt-type charger was made by Biskos et al. in 2005 Biskos, Reavell, and Collings, 2005. The design comprised of two concentric electrodes with a corona wire at the axis. The arrangement, as shown in figure A.3, allows the inner electrode to maintain a laminar flow of aerosol in the annular region. This is important in controlling the residence time of the particles in the charger. Moreover, a sheath flow in the ion generation region prevents the hydrodynamic flow of particles into the ion generation region. This control allows charging particles with high reproducibility. Furthermore, the arrangement allows very
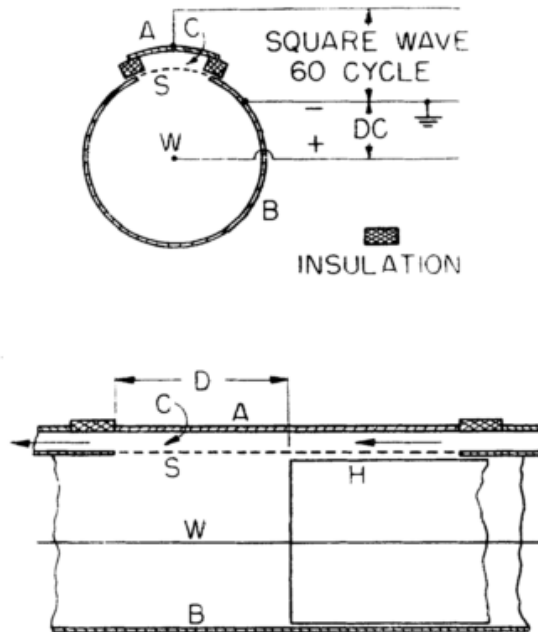
Figure A.1: Hewitt type charger developed in 1957 .Uses a corona discharge wire placed on the axis of a cylinder. A metal mesh then pushes these ions into the concentric charging zone where the aerosol flows and the particles are charged. (figure taken from Hewitt, 1957))
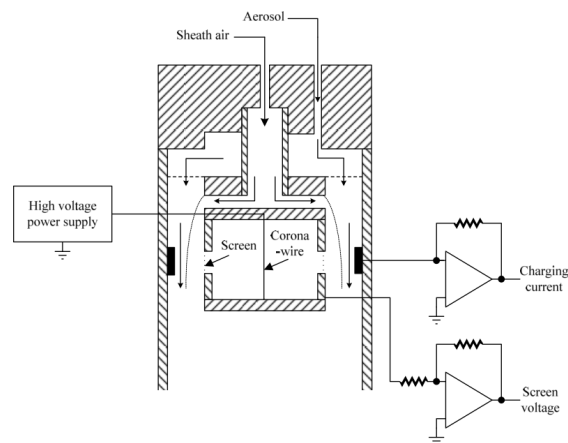
Figure A.2: Hewitt type charger with sheath air added by Liu and Pui 1965. The sheath air keeps the aerosol particles away from the mesh and the high ion intensity of the generation zone (figure taken from B. Y. H. Liu and Pui, 1975)

high intrinsic efficiency Marquard, Meyer, and Kasper, 2006 as the charging process is highly optimized.
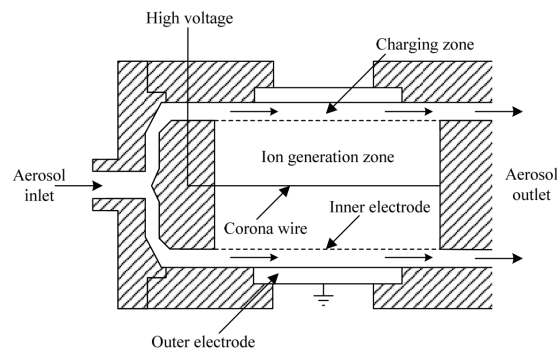
Figure A.3: Hewitt-type charger developed by Biskos et al. (2005) with sheath air and concentric cylinders. Promoted laminar flow of the aerosol in the charging region. (figure taken from Biskos, Reavell, and Collings, 2005)

A.0.1.2 Direct DC corona charger

A simple corona charger design brings the aerosol particles in direct contact with the corona region, i.e. not separating the ion generation and charging region. One of the first such design was made by Whitby et al. in 1961 Whitby, 1961.The design (shown in figure A.4) used a needle charger and was used to charge particles with positive/ negative or both polarity, depending on the mode of operation.
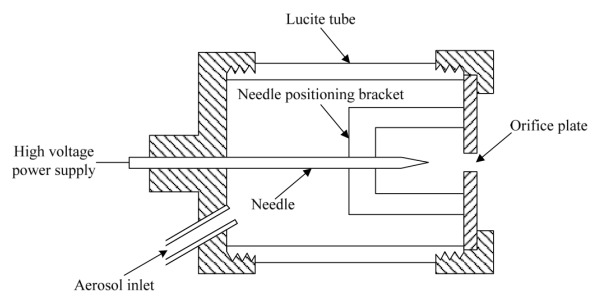
Figure A.4: Direct corona charger. The aerosol particles are brought in direct contact to the stream of ions from the corona discharge. This design was used to connect different polarity DC or AC to the electrodes to produce ions with positive/ negative or both polarity. (figure taken from Whitby, 1961)

Later, Hernandez-Sierra proposed a modified design (shown in figure A.5) that could charge particles with high efficiency **Hernandez-Sierra2003**. Alonso et al. in 2006 M. Alonso, M. Martin, and Alguacil, 2006 simplified the design, as shown in figure A.6.

Tsai et al., in 2010, developed a charger with multiple metal wires to produce the corona C.-j. Tsai et al., 2010. A sheath air flow was used that helps in keeping the particles away from the charger wall, resulting in lower wall losses. The design is shown in figure A.7. The design uses multiple corona discharge wires and a movable teflon tube to control the effective length of the wires, in order to limit the particle electrostatic losses.
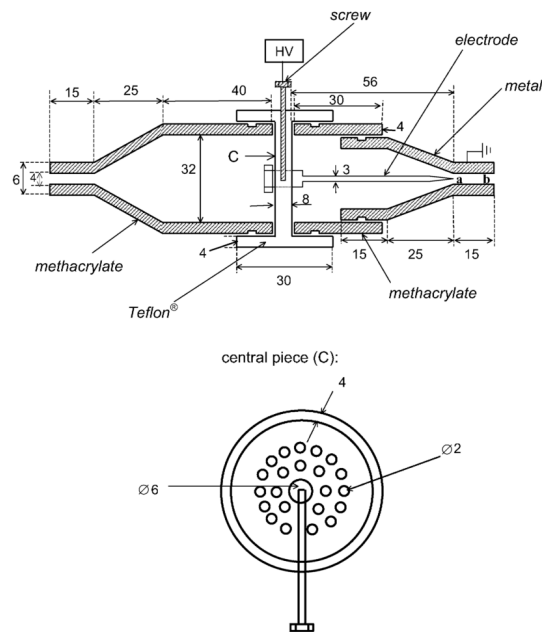
Figure A.5: Direct DC charger proposed by Hernandez-Sierra et al. in 2003. The charger is a cylindrical tube with tapered ends. There are multiple orifices at the centre through where the aerosol flows out around the corona needle that can be varied in position (a to b) and maintained at different voltage. (figure taken from **Hernandez-Sierra2003**)
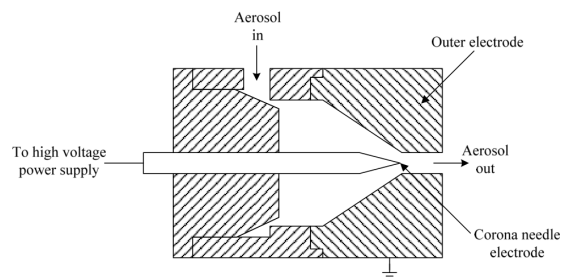
Figure A.6: Direct DC corona charger with modified geometry, simplifying the design of Hernandez-Sierra (2003), was developed by Alonso et al. in 2006. The simple design allows charging the aerosol particles. (figure taken from M. Alonso, M. Martin, and Alguacil, 2006)

Han et al., in 2008, developed a direct corona charger using carbon fibers as the corona wire material B. Han et al., 2008. This was helpful in reducing the amount of produced, an important factor to consider in charger design (discussed in section 1.4.1). However, the fiber material was not stable for long operating period.

In 2017, T. T. Han et al. employed a 'wire-to-wire' charger in a personal bio-aerosol sampler (PEBS). The charger was designed with special attention to lower ozone production which was principally achieved by lowering the corona current through lowering the ground electrode area (reduced to a wire) T. T. Han, Thomas, and Mainelis, 2017. This is shown in figure A.8.
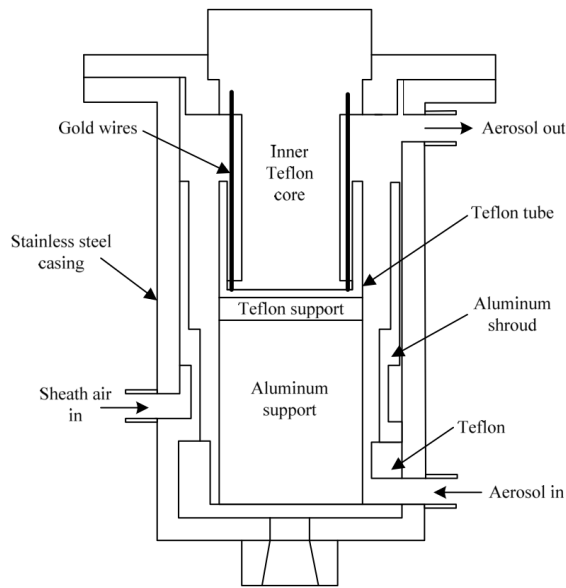
Figure A.7: Direct DC corona charger with sheath air to keep particles away from charger walls to prevent losses. Multiple corona wires are used to increase the ion concentration and the effective length can be controlled to attempt limiting the losses. Design proposed by Tsai et al. in 2010. (figure taken from C.-j. Tsai et al., 2010)
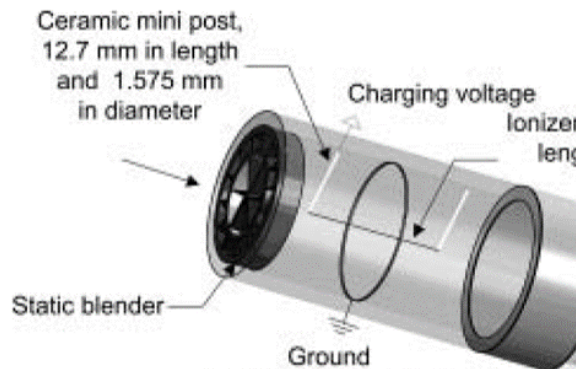
Figure A.8: A wire-to-wire charger with a premixing blender, which was used to promote the blending of the incoming particles with the produced ions. The smaller area of the ground electrode would result in a lower corona current and thus lower ozone production, as suggested by T. T. Han et al. in 2017. (figure taken from T. T. Han, Thomas, and Mainelis, 2017)

A.0.1.3   Indirect DC corona charger

Indirect corona chargers consists of two zones, one for ion generation and the other for particle charging. The generated ions enters the charging zone mainly through a carrier gas that then mixes with the aerosol stream to charge the particles.

A simple design by Medved et al. in 2000 Medved et al., 2000 (shown in figure A.9) has the generated ions and the aerosol stream mixing in a chamber and delivered at the outlet.

Marquard et al. in 2005 Marquard, Meyer, and Kasper, 2006 used two such ionizers (ion generation and injection with carrier gas) in an arrangement shown in figure A.10. The isolation of the charging region from electric field is helpful in preventing electrostatic losses. Kimoto et al. in 2010 Kimoto et al., 2010 also presented a mini version of the charger and called it the Small Mixing-type Unipolar charge (SMUC) and verified that the electrostatic losses in the charger are minimized.
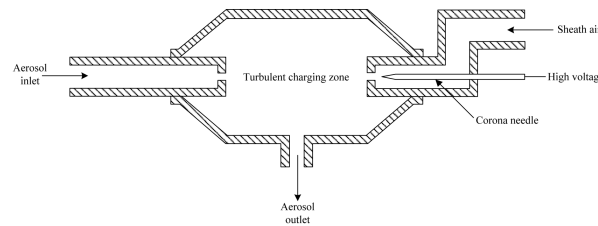
Figure A.9: Indirect DC charger with two zones (ion generation and charging) developed by Medved et al. in 2000. The ions are generated through a conrona discharge and the ions are carried with a carrier gas into the charging zone where the ions mix with the aerosol particles. The separation of the ion production isolates the aerosol particles from electric fields, reducing electrostatic losses. (figure taken from Medved et al., 2000)
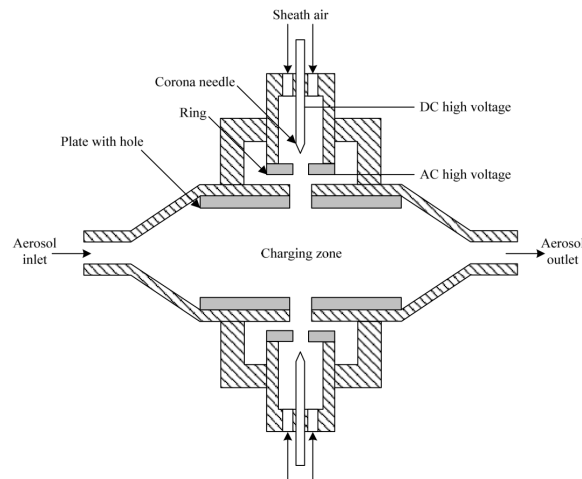
Figure A.10: Indirect charger with two corona ionizer streams entering perpendicular to the aerosol flow, developed by Marquard et al. in 2006. (figure taken from Marquard, Meyer, and Kasper, 2006)

Another design worth noting was presented by Qi. et al in 2007 Qi, D. R. Chen, and Pui, 2007 where two sonic-jet ionizers were used at equal and opposite angle to the inlet (as shown in figure A.11. This is aimed at not only isolating the electric field outside the particle flow but also at increasing the longitudinal momentum to facilitate the particle transport to the output while cancelling the radial flows through the design arrangement. The ion concentration can be controlled by using only one injector (as the authors later reported that when both the ionizers where on the ion concentration was very high and resulted in losses). Moreover, the

authors mention that the charger is "relatively insensitive" to the operation flowrates. This is relatively unique and desirable as it can allow operation of a downstream device over a wider flowrate range with lower variability from the upstream charged particle stream.
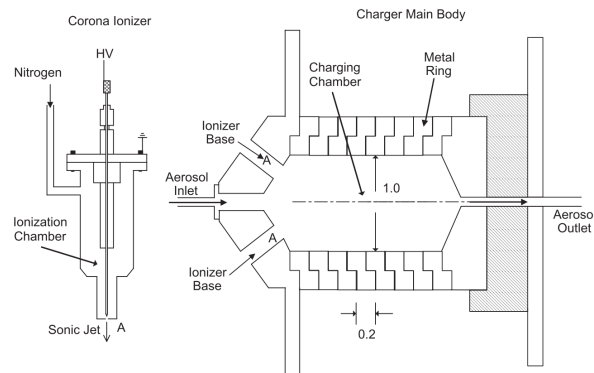
Figure A.11: Indirect corona charger with two sonic-jet type ionizers placed at equal and opposite angle fromt he aerosol input, developed by Qi et al. in 2007. The charger tries to transport the particles to the exit by using jets to transfer momentum to the particles. The charger was shown to be stable over a wide range of flow-rates. (figure taken from Qi, D. R. Chen, and Pui, 2007)

A.0.1.4 Other types

Apart from use of corona discharge from a wire and or needle, Kwon et al. in 2006 Kwon, Sakurai, and Seto, 2007 used a DC pulsed supply to achieve surface discharge from a single electrode. The device demonstrated high penetration of around 90% without the use of sheath air. This device (as shown in figure A.12) is commonly referred to as the Surface discharge Microplasma Aerosol Charger (SMAC).

The discharge is produced by applying a DC pulse to the electrode across a mica sheet, held between the ground and the top electrode. The ions enter the tube where the passing aerosol particles are thereafter charged. The charger showed low ozone production (as reported in their study on similar design in 2005) and high charging efficiency especially in the 3 to 15 nm size range.
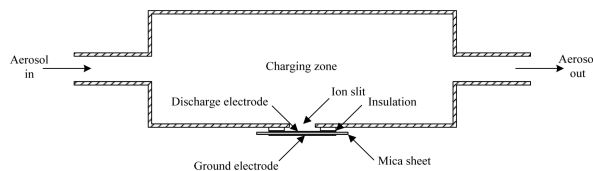
Figure A.12: Surface discharge microplasma aerosol charger that uses a dielectric in strong (pulsed) DC voltage producing electrons that are transported to a mizing chamber and used to charge cross flowign arerosol particles. (figure taken from Kwon, Sakurai, and Seto, 2007)

A.0.2 Ionizing radiation chargers

Ionizing radiation type chargers are not the most desirable for application in field studies and in monitoring network due to the employed use of radioactive materials or high energy X-ray producing system, and their associated health effects and concerns. Though the chargers are used in many laboratory equipments and can be used to produce unipolar by selecting out the desired charged ions from the source (by passing through an electric field), its use for sample collection in field and/or in monitoring stations is being avoided in this study.

A.0.3 Photoelectric chargers

Charging particles through photoionization has been studied by many authors for particle characterization Burtscher et al., 1982 Grob, Wolf, et al., 2014Nishida, Boies, and Hochgreb, 2018 Shimada et al., 1999. However, the process has also been used to make UV photoionization chargers Hontañón and Kruis, 2008 Grob, Burtscher, and Niessner, 2013. The charging process can be direct (by photo-ionizing the aerosol particle directly) as done by Nishida et al. Nishida, Boies, and Hochgreb, 2018 (shown in figure A.13) or indirect, where the UV is used to emit electrons from a metal surface as used by Grob et al. Grob, Burtscher, and Niessner, 2013 (shown in figure A.14. UV radiation is used to either directly ionize the particles or generate enough electrons to controllably charge the particles.
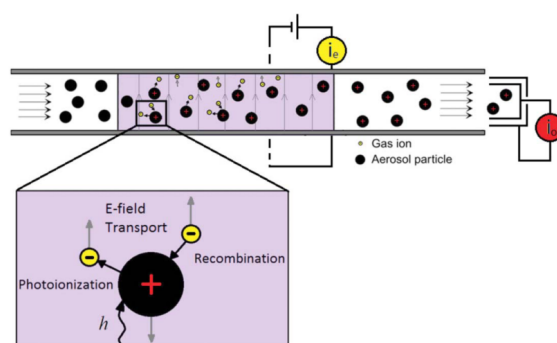
Figure A.13: Direct UV charger with UV rays entering parallel to the arerosol flow in a tube and charging the particles through photoionization. The illustration shows how the charged particles in an electric field produces a current that is then measured to characterize the particle size. (figure taken from Nishida, Boies, and Hochgreb, 2018)

It must be noted that for direct charging in this manner the aerosol particle must be photo-ionizable, which is not true for all aerosol particles. At the same time for controlled indirect UV charging, direct photoelectron emission should be at the minimum, which again is material and UV wavelength dependant. The level of control on charging depends on the relative difference of the work function of the particles and the irradiating UV photon energy. For example, Grob et al. Grob, Burtscher, and Niessner, 2013 observed no direct photoelectron emission for NaCl particles but estimated it to be the major charging mechanism for flame
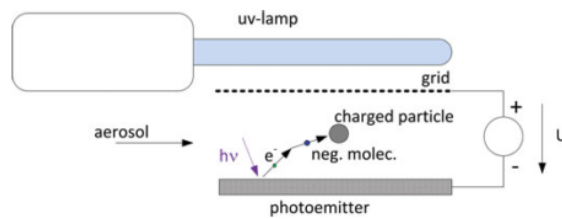
Figure A.14: Indirect UV charger where UV lamp is used to emit electrons from a metal surface that then produces negative ions that combine with incoming aerosol particles to negatively charge them. (figure taken from Grob, Burtscher, and Niessner, 2013)

soot particles. This effect can majorly effect other combustion and metal aerosols. However, even with some uncertainty in charging induced by this material dependance, the use of indirect UV chargers has its own advantages for its low ozone production, lower losses and comparable efficiency to corona chargers Grob, Burtscher, and Niessner, 2013.

Another design that potentially significantly reduces direct photoemission in indirect UV charger was developed by Shimida et al. in 1999 Shimada et al., 1999 where a thin gold foil was irradiated with UV from one side and electrons are emitted on the other side (as shown in figure A.15). However, the device was employed as a precipitator and thus was not characterized for charging efficiency.

Indirect UV charging is a promising mechanism for the current application and can be used with dielectric barrier discharge eximer lamps, which can produce a range of wavelengths and has a longer lifetime.
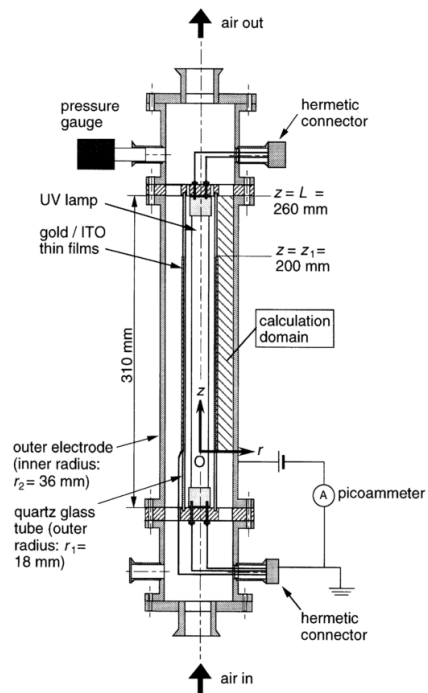
Figure A.15: Indirect UV charger where UV lamp is irradiated on one side of a gold foil and is used to emit electrons on the other side which is used to charge aerosol particles in the annulus tube. (figure taken from Shimada et al., 1999)

B Appendix to chapter 2

B.1   Baseline correction

The spectra are baseline corrected using a smoothing spline fitting and subtraction (Kuzmi-
akova, Dillner, and Takahama, 2016). The background points to which the smoothing spline
is fitted can be identified using a number of methods (e.g., derivatives, mixture models, and
asymmetric weights) (Liland, AlmÃ¸y, and Mevik, 2010; Rooi and Eilers, 2012). In this work, the
points belonging to the background are selected by applying a moving window within which
the mean and standard deviation of absorbance is calculated, and excluding points with a
standard deviation exceeding a preselected threshold. The moving mean was additionally
used to differentiate the broader diffused peaks (e.g. 2700 cm^{-1} - 3200 cm^{-1}) from background.

(a)

(b)

(c)

(d)
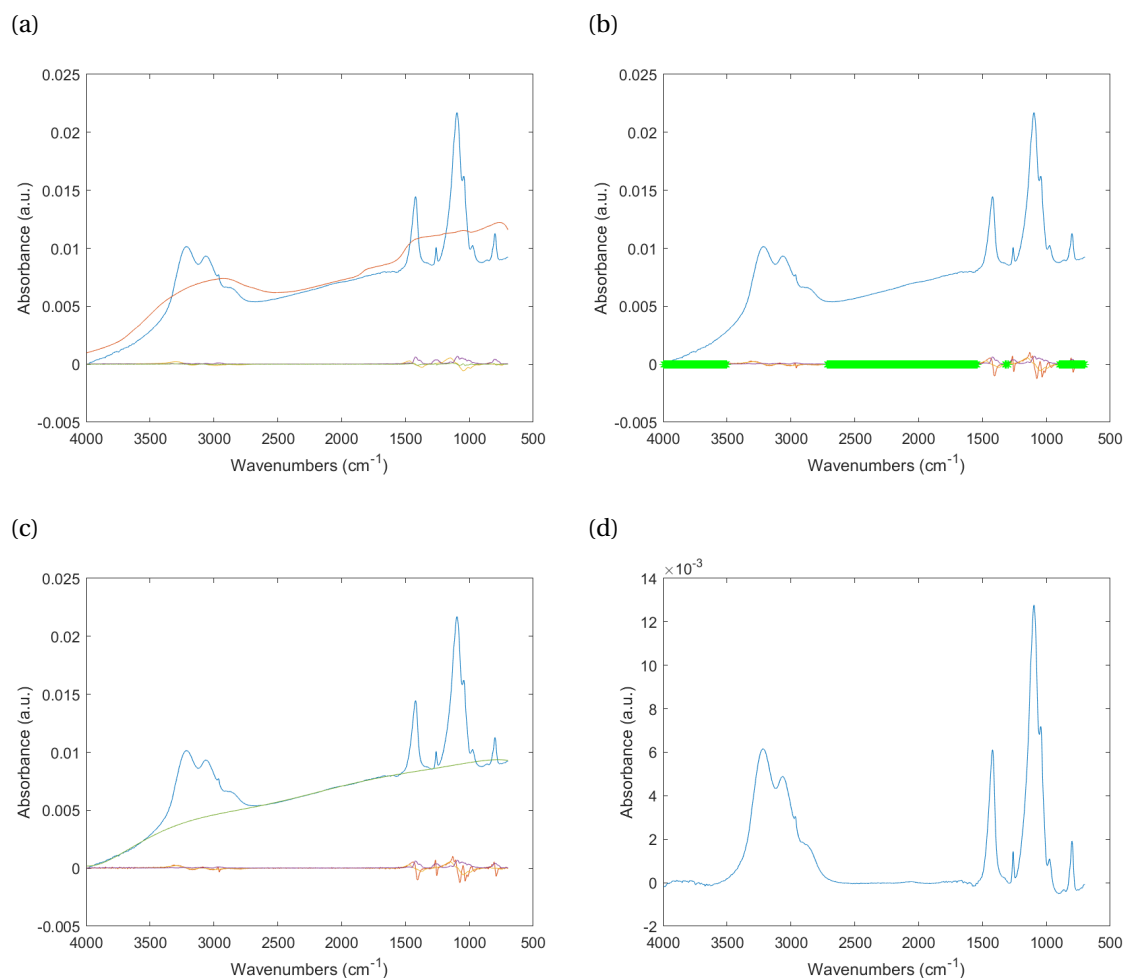
Figure B.1: (a) Absorbance spectra (blue), moving mean of the absorbance spectra (red), slope
of the absorbance spectra (yellow), moving mean of the slope (green) and te moving standard
deviation of the slope (purple); (b) Identified baseline points (green points); (c) A smoothed
spline fitting the baseline points (green), and (d) baseline corrected spectra.

B.2   VAIRS against image analysis

Spatial distribution representation as obtained from variable aperture IR spectroscopy analysis and that from image analysis (Section 2.4.2) for the various experiments.
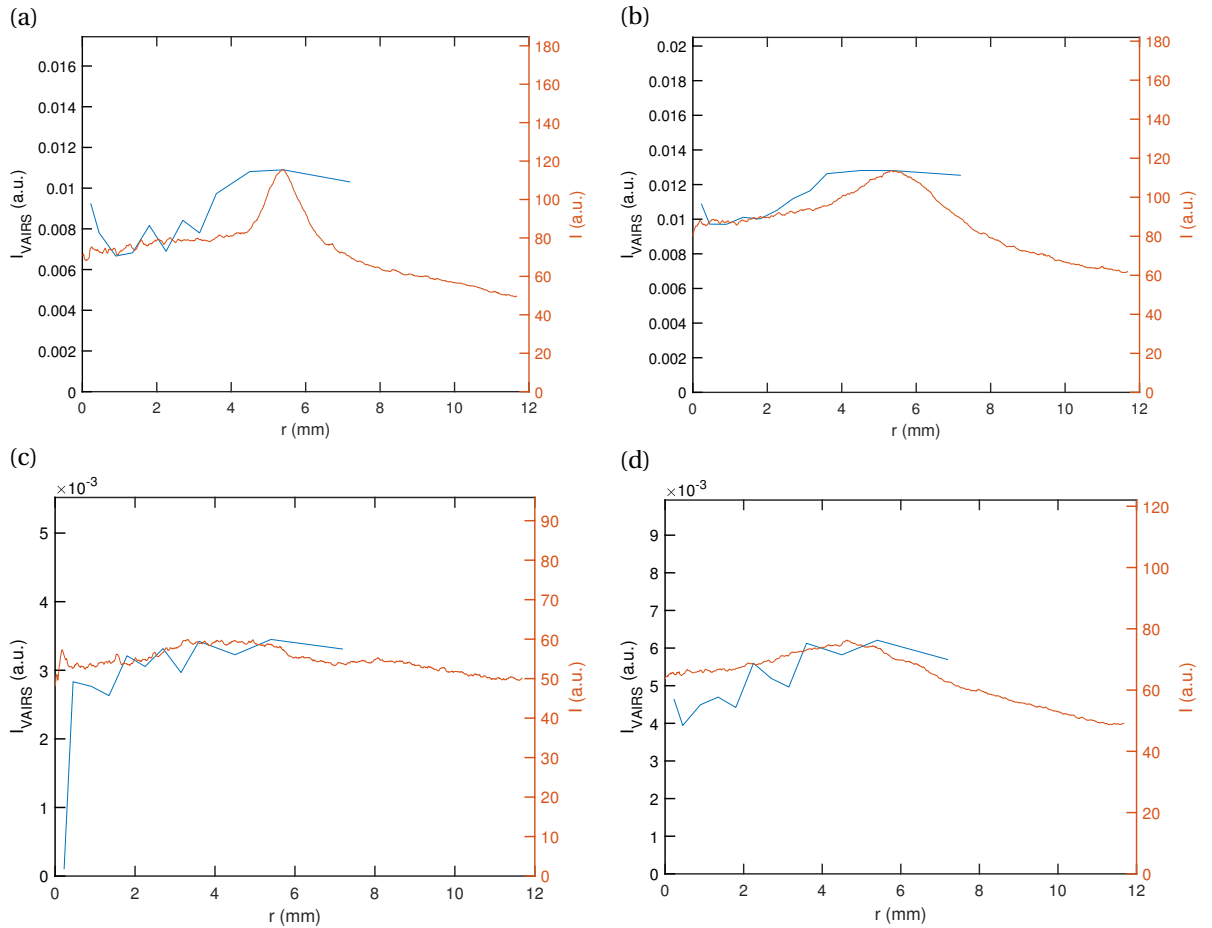
Figure B.1: Comparison of the m/A profile obtained from variable aperture IR spectroscopy (VAIRS) with the average intensity profile that obtained from the image analysis for different experiments.

(a)

(b)

(c)

(d)
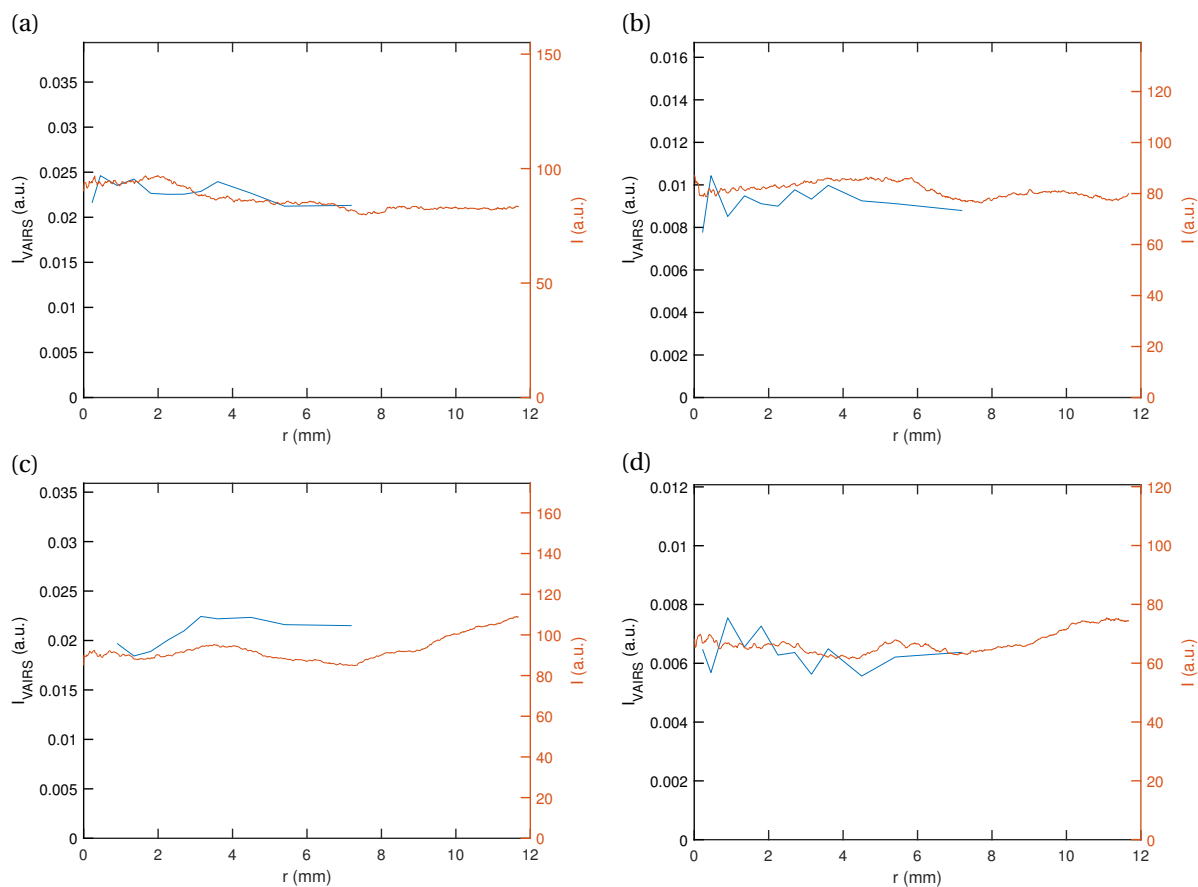
Figure B.2: Comparison of the m/A profile obtained from variable aperture IR spectroscopy (VAIRS) with the average intensity profile that obtained from the image analysis for different experiments.

B.3 Quantitative analysis

The IR response to particle loading when the peak heights of α_v, α_{ref} and $\alpha_{v,ref}$ around 1110 cm^{-1} and 1410 cm^{-1}, instead of the exact values at those wavenumbers (Figure B.2).

IR response against particle loading that does not use the image analysis of the optical microscopy images, rather uses the crystal diameter is as a fixed scaling factor (Figure B.1). The overall effect is that the points move in the abscissa when compared to Figure B.3.

The lower detection limit (LDL) can be calculated using multiple methods (Armbruster and Pry, 2008). One method is to calculate the value that corresponds to a signal-to-ratio (SNR) of 3.

The measured absorbance values in Figure B.3 corresponds to the 6 mm diameter aperture (standard in the current ambient FT-IR measurements) whilst the volume areal density corresponds to the entire crystal diameter. Although the deposition over the crystal determines the

(a)

(b)
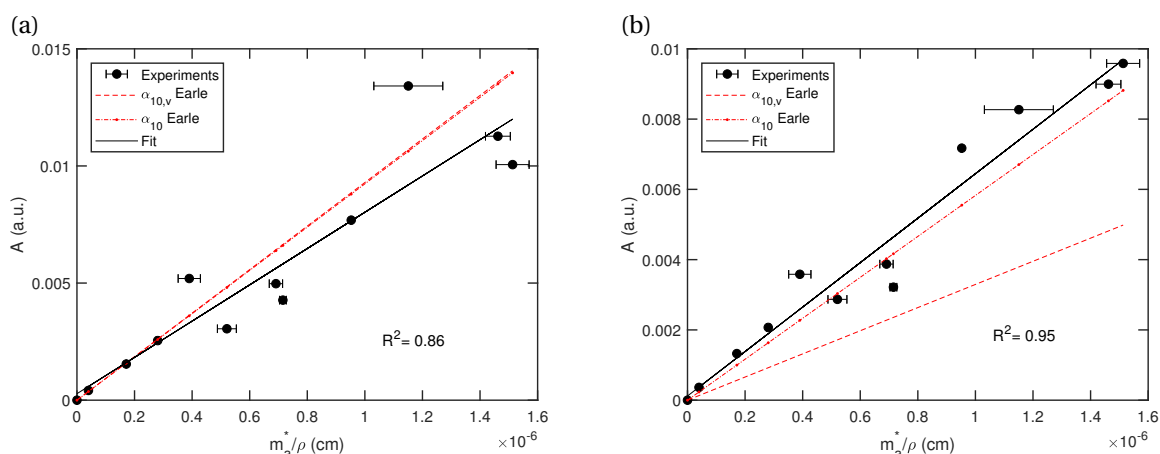
Figure B.1: Response of IR absorbance (A) against the volume areal density (cm) of the total particle collected reference from CPC transients graphs (Figure 2.4) calculated using no image analysis, for (a) absorbance at 1110 cm^{-1} (for $\nu_3(SO_4^{2-})$) and (b) 1410 cm^{-1} (for $\nu_4(NH_4^-)$). The fractional uncertainly in the volume areal density estimate (the error bars) remains unchanged from Figure 2.12 as it is a direct outcome of the ratio of the deviation in particle collected count (Figure 2.4).

(a)

(b)

Figure B.2: Response of IR absorbance (A) against the volume areal density (cm) of the total particle collected reference from CPC transients graphs (Figure 2.4), for (a) absorbance at the peak near 1110 cm^{-1} (for $\nu_3(SO_4^{2-})$) and (b) at the peak near 1410 cm^{-1} (for $\nu_4(NH_4^-)$). The fractional uncertainty in the volume areal density estimate (the error bars) remains unchanged from Figure 2.12 as it is a direct outcome of the ratio of the deviation in particle collected count (Figure 2.4).

LDL, it is the $m^{(a)}$ over the beam diameter that corresponds to the spectroscopic measurement, for example the lowest measured total mass of 415 ng over the crystal corresponds to only 80 ng under the beam. As for a fixed deposition mass over the crystal the SNR will be different for

(a)

(b)
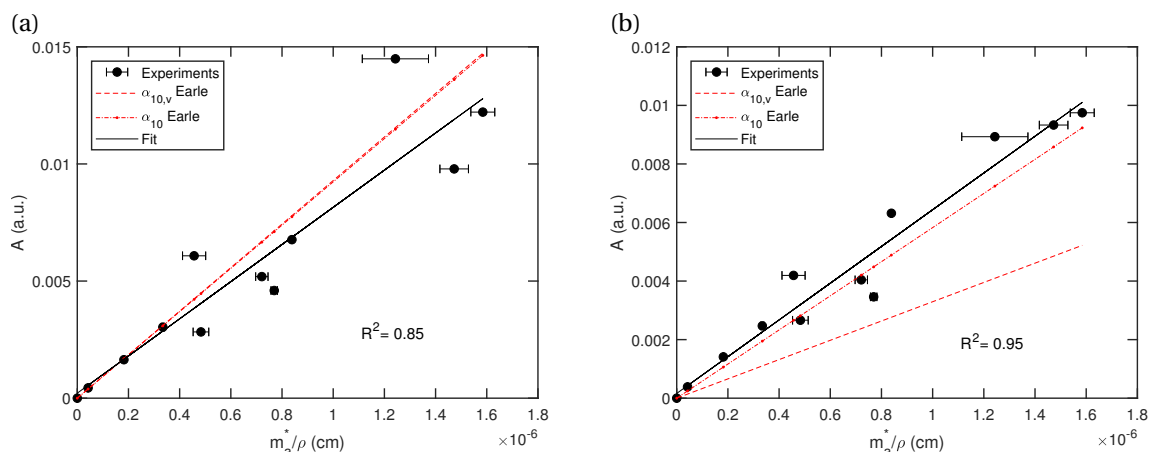
Figure B.3: Response of IR absorbance (A) against the volume areal density (cm) of the total particle collected reference from CPC transients graphs (Figure 2.4), for (a) absorbance at 1110 cm^{-1} (for $\nu_3(SO_4^{2-})$) and (b) 1410 cm^{-1} (for $\nu_4(NH_4^-)$). The fractional uncertainly in the volume areal density estimate (the error bars) remains unchanged from Figure 2.12 as it is a direct outcome of the ratio of the deviation in particle collected count (Figure 2.4).

Figure B.4: Comparison of the volume areal density (cm) of the total particle collected reference from CPC transients graphs (Figure 2.4) calculated using no image analysis against that calculated using the image analysis.

different measurements apertures, we use the analysis of the baseline corrected FT-IR spectra of different apertures to assess the LDL. This allows us to use the other measurements with apertures down to 0.25 mm to estimate the signal the device and method combination is able to statistically differentiate from a blank (just noise). We calculate the $m^{(a)}$ under the beam, and compare it against SNR - measured as the square of the ratio of the peak height to the root mean square (RMS) of $\nu > 3500$cm^{-1}, a region characteristic of the noise. As the height of the diffused peak (around 3200 cm^{-1}) is lower than the pronounced peaks and is sensitive to

the baseline correction, we use it for determining the SNR for different apertures that have different $m^{(a)}$ (Figure B.5). SNR > 3, corresponds to $m^{(a)} > 1 (\text{ng/cm}^2)$ (and 2(ng/cm^2) for SNR >10) and to a LDL of 6.3 ng total mass of ammonium sulfate on the crystal, when measured using a 6 mm diameter aperture. Hence, using SNR analysis the LDL is 6 ng - the lowest amount that can be detected by the device and analysis method.

Another method is to use the residual and slope of the calibration curve formed with low concentrations (Centre., 2016) - where low concentration is a maximum of 10 times the LDL and the calibration curve has 5 points (1 unloaded and 4 loaded). The LDL in such a case is calculated using the equation B.1, where $s_{y,x} = \sqrt{\frac{(y_i - \hat{y})^2}{n-2}}$ is the standard deviation of the residuals. As we have error in reference (x) values, the procedure can result in biased estimation. With the experimental data we have, the first 5 points (including a 0 and 4 loaded points), we obtain an LDL of 259 ng for the 1410 cm^{-1} peak, 10 times of which is much smaller than the larger mass of the 5$^{\text{th}}$ point 4.4 µg. Taking the fist 4 points instead for the calculation results in a LDL of 52 ng instead. The variability is expected as the concentration range is very large and the points have heteroscedasticity - both of which are expected to give high estimates (Centre., 2016). Considering the limitations of the slope analysis of the calibration curve we calculate a weighted average for the lower limit of the LDL using the SNR analysis (70%) weight and the slope analysis with 5 points (30%). The resulting in the lower estimate of the LDL to be around 82 ng.

$$\text{LDL} = 3.8 \frac{s_{y,x}}{b} \sqrt{1.1 + \frac{\bar{x}^2}{\sum_1^n (x_i - \bar{x})^2}} \tag{B.1}$$

(a)

(b)

(c)
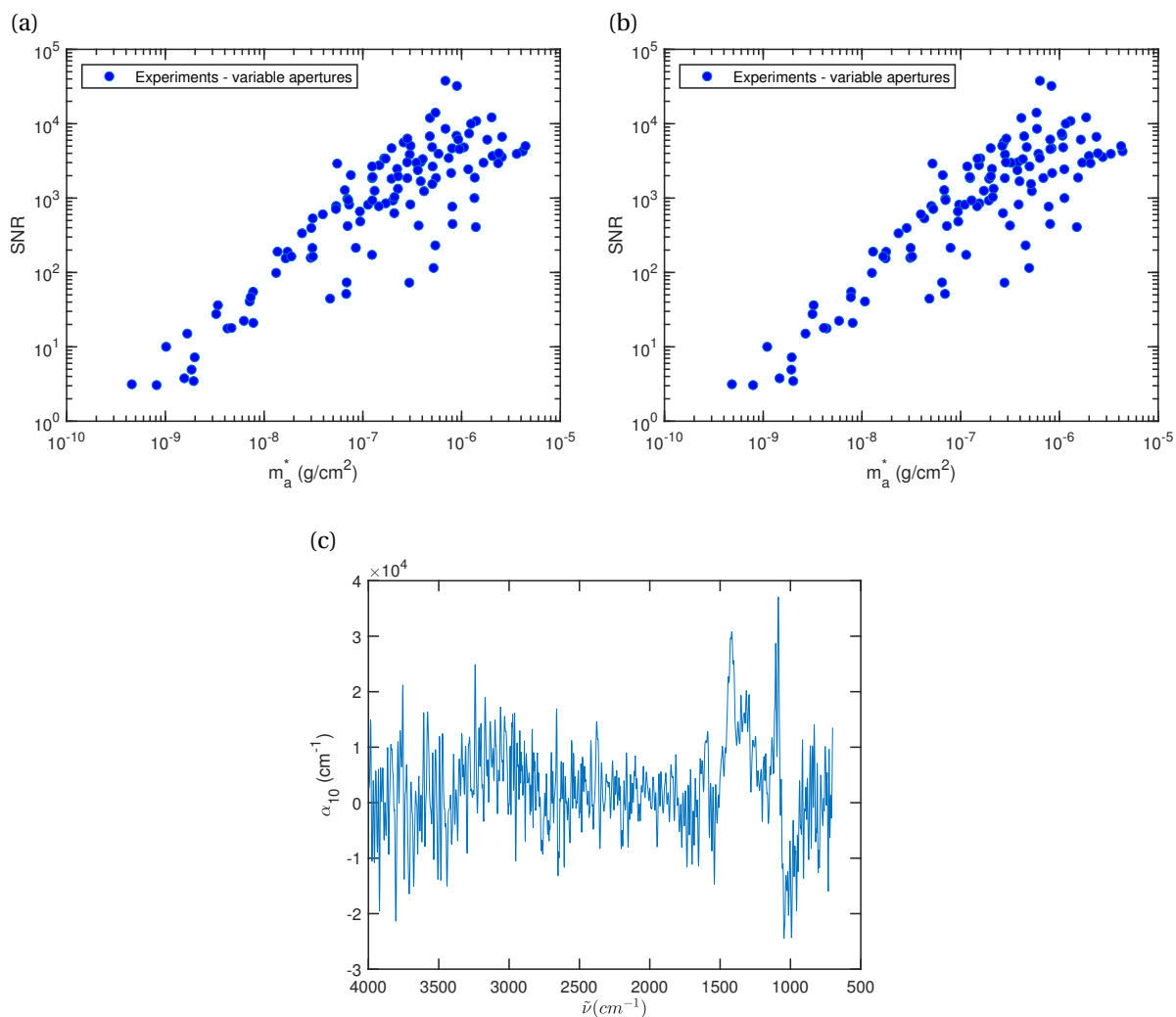
Figure B.5: Signal-to-noise ratio (SNR) calculated for IR absorbance spectra for all experiments measured using different aperture sizes (119 points in total). The SNR is plotted against the corresponding mass areal density for the mass under the beam, with the total mass areal density calculated using (a) image analysis (b) no image analysis. (c) The absorbance spectra corresponding to SNR =10.

C Appendix to chapter 3

C.1 Comparison of scale of diffusion and momentum and verification of flow assumptions

The Péclet number and Stokes number range for different flow Reynolds number (in laminar regime) and different particle size, allows assessing whether diffusion and impaction effects can be neglected (Figure C.1). Another important validation is to check whether the assumption of the particles starting to move radially from an apparent line $r/R = z/H$, where H can have any value is congruent to the numerical simulations (Figure C.2).

(a)   (b)
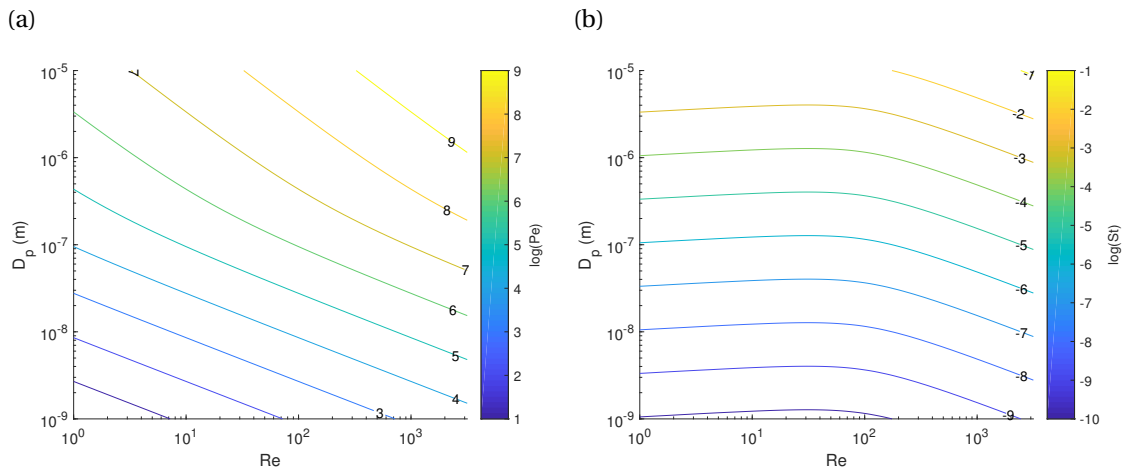
Figure C.1: (a) Order of magnitude of Péclet number (contour of $\log Pe$), and (b) order-of-magnitude-of Stokes number (contour of $\log St$) for length scale $10\,mm$; both for a range of particle sizes and flow Reynolds number .

(a)

(b)
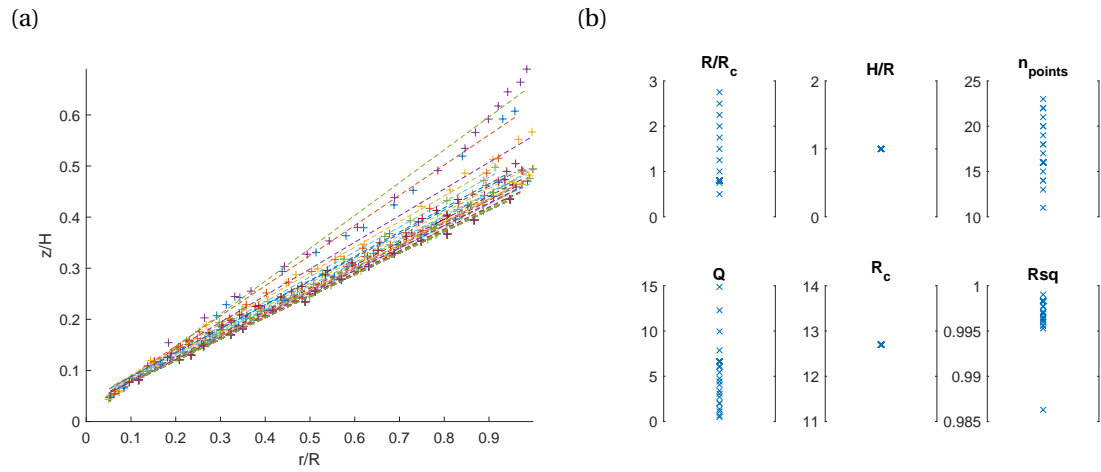
Figure C.2: Analyzing the velocity flow profile in COMSOL simulations for points where the magnitude of v_r and v_z are within 5% deviation. (a) Linear fit of normalized z (z/H) against normalized r (r/R) for the said points, and (b) the range of geometric and flow parameters for the simulations and the number of points used for determining the linear fit and R^2.
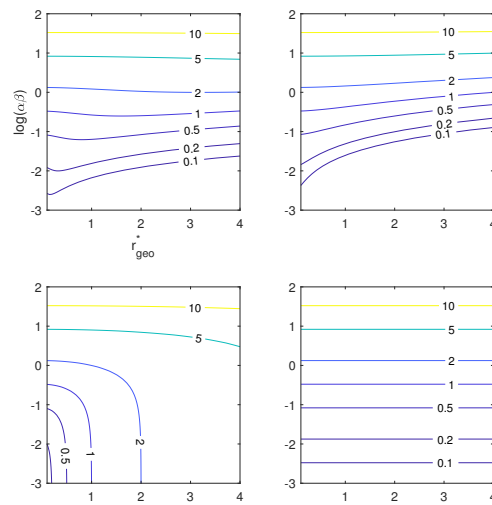
Figure C.3: $r^\dagger f$, max on the $log(\alpha\beta) - r^\dagger_{geo}$ space for drift included (top row) or excluded (bottom row), and finite R/R_c (left column) or $R/R_c = 0$ (right column) for fixed $r^*_{lim} = 1$ and $H/R = 1$.

C.2 Derivation: Radial system

During particle collection, $\mathbf{u} = v_r(r,z)\mathbf{r}$ and $\mathbf{E}_0 = -E_0\mathbf{z}$, which means:

$$\mathbf{v} = \mathbf{u} + \mathbf{v}_{elec} = v_r(r,z)\,\mathbf{r} - v_{elec}\,\mathbf{z}$$

where $v_r(r,z)$ is the fluid velocity in r direction and $v_{elec} = \frac{qE_0 C_c}{3\pi\mu D_p}$ is the electrical migration velocity. Assuming, that the particle movement in r and z directions are independent of each other and are both a function of time (t) only, we obtain:

$$\frac{dr}{dz} = \frac{dr/dt}{dz/dt} = \frac{\mathbf{v}\cdot\mathbf{r}}{\mathbf{v}\cdot\mathbf{z}} = \frac{v_r}{-v_{elec}}$$

$$\frac{dr}{dz} = -\frac{v_r}{v_{elec}} \tag{C.1}$$

We solve this differential equation for the particle trajectory in (r,z) with the boundary conditions

$$\text{at } t = 0, (r,z) \equiv (r_0, z_0) \text{ ,and}$$

$$\text{at } t \to \infty, (r,z) \equiv (r_f, 0)$$

where (r_0, z_0) marks the beginning of radially outward flow of the particle along with the flow streamline and $(r_f, 0)$ is the final radial position where the particle is collected. We re-write the differential equation C.1 by separating $v_r(r,z)$ into two independent functions $(v_r(r,z) = \overline{v}_r(r) f_{vr}(z))$:

$$\frac{1}{\overline{v}_r(r)} dr = -\frac{f_{vr}(z)}{v_{elec}} dz$$

where $\overline{v}_r(r)$ is the average radial velocity at any given r and $f_{vr}(z)$ is the functional dependence of the velocity on z (height from the substrate). Integrating the above equation under the boundary conditions:

$$\int_{r_0}^{r_f} \frac{2\pi r H_{\text{flow}}}{Q} dr = -\int_{z_0}^{0} \frac{f_{vr}(z)}{v_{elec}} dz$$

where H_{flow} is the height till where the flow profile $v_r(r,z)$ extends. Rearranging the variables:

$$(r_f^2 - r_0^2) = \frac{Q}{\pi v_{elec} H_{\text{flow}}} \int_0^{z_0} f_{vr}(z) dz \tag{C.2}$$

The mathematical mean of $f_{vr}(z)$ till z_0 can be expressed as,

$$\overline{f}_{vr}(z_0) = \frac{\int_0^{z_0} f_{vr}(z)\,dz}{z_0}$$

The significance and solution for various flow inlet profiles of this term $\overline{f}_{vr}(z_0)$ (or $\overline{f}_{vr}(r_0)$) is explained in Appendix C.2.1.

With the assumption that streamlines stay parallel (for laminar flow) and that the vertical streamline at r_0 translates into the horizontal streamline z_0, through

$$\frac{r_0}{R} = \frac{z_0}{H_{\text{flow}}} \tag{C.3}$$

we obtain an equation for mapping the final position r_f of a particle from its initial position r_0,

$$\boxed{r_f^2 = r_0^2 + \frac{Q}{\pi v_{elec}}\left(\frac{r_0}{R}\right)\overline{f}_{vr}(z_0)} \tag{C.4}$$

The co-ordinates at any point during the particle trajectory (r,z) is found by changing the upper limits of integration from $t \to \infty$ to any arbitrary time t, giving:

$$\boxed{r^2 = r_0^2 + \frac{Q}{\pi v_{elec}}\left(\frac{r_0}{R}\right)\left(\overline{f}_{vr}(z_0) - \overline{f}_{vr}(z)\right)} \tag{C.5}$$

Dividing by $(RR_c)^2$ (the product of inlet tube radius R and the characteristic radius R_c), and rearranging the equation C.4,

$$\boxed{\left(\frac{r_f}{R_c}\right) = \left(\frac{r_0}{R}\right)\left(\frac{R}{R_c}\right)\sqrt{1 + \left(\frac{v_{in}}{v_{elec}}\right)\left(\frac{r_0}{R}\right)^{-1}\overline{f}_{vr}(r_0)}} \tag{C.6}$$

where $v_{in} = Q/(\pi R^2))$ is the tube inlet velocity, r_0/R is the dimensionless initial position in the tube, and r_f/R_c is the dimensionless final position on the collection surface.

C.2.1 Significance of $\overline{f}_{vr}(r_0)$ and $\overline{f}_{vr}(z_0)$ for radial system

$\overline{f}_{vr}(z_0)$ is related to the flow profile in z-direction for the radial fluid flow,

$$\overline{f}_{vr}(z_0) = \frac{\int_0^{z_0} f_{vr}(z)\,dz}{z_0}$$

where,

$$f_{vr}(z) = \frac{v_r(r,z)}{\overline{v}_r(r)}$$

For an incompressible flow, the mass conversation equation of the fluid reduces to a volumetric flow conservation equation, and under laminar flow the streamlines are parallel. Thus, the volumetric flow rate under the same streamline (for example that at r_0/R and $z_0/flowH$) is a constant.

$$Q(r < r_0) = Q(z < z_0)$$

$$\implies \int_0^{r_0} [v_{in}(r)(2\pi r)]\,dr = \int_0^{z_0} [v_r(r_0,z)(2\pi r_0)]\,dz$$

$$\implies \int_0^{r_0} [v_{in}(r)(2\pi r)]\,dr = \overline{v}_r(r_0)(2\pi r_0)\left(z_0\overline{f}_{vr}(z_0)\right)$$

$$\implies \overline{f}_{vr}(z_0) = \left(\frac{H}{z_0}\right)\frac{\int_0^{r_0} v_{in}(r)(2\pi r)\,dr}{Q}$$

$$\boxed{\overline{f}_{vr}(r_0) = \left(\frac{R}{r_0}\right)\frac{\int_0^{r_0} v_{in}(r)(2\pi r)\,dr}{Q}}$$

$$\overline{f}_{vr}(r_0) = \left(\frac{R}{r_0}\right)\frac{\int_0^{r_0} r v_{in}(r)\,dr}{\int_0^{R} r v_{in}(r)\,dr}$$

1. For a uniform inlet flow (near plugged flow): In this case,

$$v_{in}(r) = k = const$$

   Thus, the term $\overline{f}_{vr}(r_0)$ simplifies to,

$$\overline{f}_{vr}(r_0) = \frac{r_0}{R}$$

2. For a parabolic distribution of flow: In this case,

$$v_{in}(r) = v_{in,max}\left(1 - \left(\frac{r}{R}\right)^2\right)$$

   Thus, the term $\overline{f}_{vr}(r_0)$ simplifies to,

$$\overline{f}_{vr}(r_0) = \left(\frac{r_0}{R}\right)\left(2 - \left(\frac{r_0}{R}\right)^2\right)$$

C.3 Derivation: Linear system

For a linear system translationally symmetric in y-direction, $\mathbf{X} \equiv (\mathbf{x}, \mathbf{z})$. For the case where electrostatic field and the fluid velocity are perpendicular to each other, $\mathbf{E}_0(\mathbf{X}) = \mathbf{E}_0(\mathbf{z})$ and $\mathbf{u}(\mathbf{X}) = \mathbf{u}(\mathbf{x})$, a solution for $\mathbf{v}(\mathbf{X})$ exists.
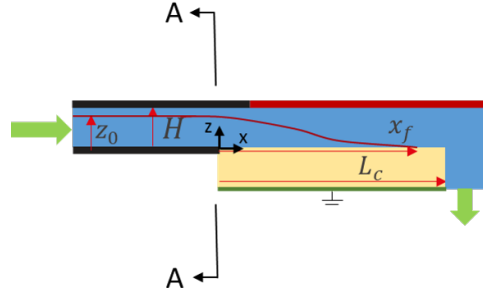
Figure C.1: Basic schematic with geometric variables for a Linear system.

The basic schematic of the linear system (Figure C.1) has a characteristic length L_c - mostly collection surface size, though it can represent a region of interest (for example beam size or intended spot size for some applications). The fluid inlet is parallel to the collection surface for the linear system (a channel of height H, to the left of the plane AA). Particle collection region is where the particle comes under the influence of the electric field (to the right of plane AA), and we assume that in this region, the fluid flow is perpendicular to the electric field. The electric field is generated by using electrodes (at a voltage difference of V_0), separated by a distance H from the collection surface (at a voltage V_g). For the linear system, the flow in the collection region is same as that in the inlet and the average fluid velocity remains a constant. The electric field is mostly in $-ve$ z-direction, which is further ensured by placing the collection surface at a distance $x = -H$ away from the edge of the electrode. This setup reduces the variation of $\mathbf{E}_0$ in x-direction in the inlet region (left of plane AA), by reducing the fringe effect at the edge of the electrode and the collection surface by having a larger base.

Using the solution of $\mathbf{v}(\mathbf{X})$, we solve for the particle trajectory in linear system, $(x(t), z(t))$ (Appendix C.3.1). This is done assuming that the motion in $x(t)$ and $z(t)$ are independent of each other, and that at the initial conditions (x_0, z_0), is $x_0 = z_0$. This results from placing the collection surface at a distance $x = -H$ away from the edge of the electrode. Furthermore, it allows a closer comparison to the radial system.

Finally, for particle deposition analysis, the final position of the particle at $t \to \infty$, such that $z(\infty) = 0$, is of interest. Furthermore, by including the characteristic lengths into the equations we formulate a basic dimensionless-analytical model for predicting the final position of deposition (x_f / L_c), given the initial position in the channel (z_0 / H), the ratio of the average fluid velocity in the inlet channel/ tube to the electrostatic migration velocity (v_{in} / v_{elec}), and the x direction fluid velocity flow profile $\overline{f}_{vx}(z_0)$, derived in appendix C.3.2. Equation C.1

shows the equation for linear system

$$\left(\frac{x_f}{L_c}\right) = \left(\frac{z_0}{H}\right)\left(\frac{H}{L_c}\right)\left(1 + \frac{v_{in}}{v_{elec}}\overline{f}_{vx}(z_0)\right) \tag{C.1}$$

$$\overline{f}_{vx}(z_0) = \begin{cases} 1 & \text{, for plug-flow inlet} \\ 2(z_0/H) - (4/3)(z_0/H)^2 & \text{, for parabolic-flow inlet} \end{cases}$$

C.3.1 Detailed derivation of linear ESP system

For the particle migration in Cartesian coordinates (x, z)

$$\mathbf{v} = v_x(z)\,\mathbf{x} - v_{elec}\,\mathbf{z}$$

where $v_x(x, z)$ is the fluid velocity in x direction and $v_{elec} = \frac{qE_0 C_c}{3\pi\mu D_p}$ is the electrical migration velocity. Using similar assumptions (Appendix C.2),

$$\frac{dx}{dz} = -\frac{v_x}{v_{elec}} \tag{C.2}$$

with a different set of boundary conditions,

$$\text{at } t = 0, (x, z) \equiv (x_0, z_0) \text{ ,and}$$

$$\text{at } t \to \infty, (x, z) \equiv (x_f, 0)$$

where (x_0, z_0) is the initial position of the particle (marked with the initial height in the tube), and $(x_f, 0)$ is the final position where the particle is collected. Using similar method of separation of variables (Appendix C.2), we obtain the equation

$$\int_{x_0}^{x_f} \frac{WH}{Q}\,dr = -\int_{z_0}^{0} \frac{f_{vx}(z)}{v_{elec}}\,dz$$

where W is the width (depth) of the channel and H is the height of the channel and the flow is confined between the two parallel plates at $z = 0$ and $z = H$. The electric field from the high voltage electrode placed above the collection surface will have influence till some length in the $-ve$ x-direction, where the particles at $z \to 0$ will start depositing. Hence, the electrode is placed at x_0, from the start of the collection surface. As this migration effect in the region from $x = 0$ to $x = x_0$ is highest for the particles closest to the height of the channel, we assume that the scale of x_0 is such that $z_0 \simeq x_0$. Rearranging the variables, we obtain an equation for

mapping the final position x_f of a particle from its initial position x_0.

$$x_f = x_0 + \frac{Q}{W v_{elec}} \left(\frac{z_0}{H}\right) \overline{f}_{vx}(z_0) \tag{C.3}$$

The co-ordinates at any point during the particle trajectory (x, z) is found by changing the upper limits of integration from $t \to \infty$ to any arbitrary time t, giving:

$$x = x_0 + \frac{Q}{W v_{elec}} \left(\frac{z_0}{H}\right) \left(\overline{f}_{vx}(z_0) - \overline{f}_{vx}(z)\right) \tag{C.4}$$

Dividing by HL_c (the product of inlet channel height H and the characteristic length L_c), and rearranging the equation C.3,

$$\left(\frac{x_f}{L_c}\right) = \left(\frac{z_0}{H}\right)\left(\frac{H}{L_c}\right)\left(1 + \frac{v_{in}}{v_{elec}} \overline{f}_{vx}(z_0)\right) \tag{C.5}$$

where $v_{in} = Q/(WH)$ is the channel inlet velocity, z_0/H is the dimensionless initial position in the tube, and x_f/L_c is the dimensionless final position on the collection surface.

C.3.2   Significance of $\overline{f}_{vx}(z_0)$ for linear system

For the linear system, $\overline{f}_{vx}(z_0)$ is related to the initial position as,

$$\overline{f}_{vx}(z_0) = \frac{\int_0^{z_0} f_{vx}(z)\,dz}{z_0}$$

where,

$$f_{vx}(z) = \frac{v_x(x,z)}{\overline{v}_x(x)}$$

1. For a uniform-flow inlet (near plugged flow):

$$v_x(x,z) = \overline{v}_x(x)$$

Which results in:

$$\overline{f}_{vx}(z_0) = 1$$

2. For a parabolic-flow inlet:

$$v_x(x,z) = 2\overline{v}_x(x)\left(1 - \left(\frac{2z}{H} - 1\right)^2\right)$$

Which results in:

$$\overline{f}_{vx}(z_0) = 2\left(\frac{z_0}{H}\right) - \frac{4}{3}\left(\frac{z_0}{H}\right)^2$$

C.4 Comparison of radial and linear systems

We qualitatively compare the general equation C.1 and 3.4 for the linear and radial system in terms of how v_{in}/v_{elec} affects the overall collection performance. Assuming the plug-flow inlet case for simplicity, the equations for the linear and radial system is approximately $\Gamma_{lin} \approx (1 + v_{in}/v_{elec})$ and $\Gamma_{rad} \approx \sqrt{1 + v_{in}/v_{elec}}$, where Γ is the ratio of the final-dimensionless position to the initial-dimensionless inlet position (Figure C.1b) for some reference values of v_{in}/v_{elec} (Figure C.1a). A higher value of this response function, Γ, is undesirable as it would mean that particles travel out further away for the same inlet positions, i.e. correspond to lower collection efficiency. Moreover, higher slope of Γ with respect to v_{in}/v_{elec} implies that the final particle deposition is more sensitive to any change in operating condition or particle property, which is undesirable as dependence on any of these variables becomes high. Hence, qualitatively, the radial system has a higher collection efficiency and is more robust to changes in flow rate or size, for example.

(a) (b)
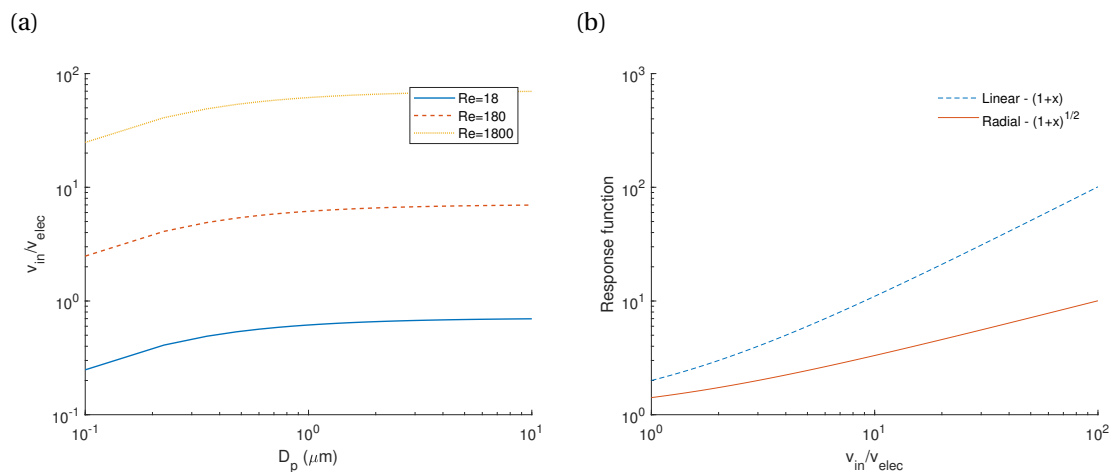
Figure C.1: (a) Example of range of values of the ratio v_{in}/v_{elec} for various particle sizes and flow Reynolds number (Re), and (b) Difference in the response function (ratio of dimensionless final position and initial position) for linear and radial systems.

C.5 $\overline{f}_{vx}(z_0)$ when using linear system to describe particle drift in the tube of a radial system

$$\overline{f}_{vx}(z_0) = \frac{\int_0^{z_0} f_{vx}(z)\,dz}{z_0}$$

where,

$$f_{vl}(z) = \frac{v_x(x,z)}{\overline{v}_x(x)}$$

The inlet tube of a radial system is equivalent to a linear system. Suppose the particle deposition in a linear system is imagined to happen in a different coordinate space $(x, z) \equiv (a, b)$, where:

1. $x = a$, and $b = m\frac{z}{z_0} + c$, i.e. b is a linear transformation of z.

2. The transformation is defined by, $(x_0, z_0) \equiv (a_0, b_0)$, and $(x_f, 0) \equiv (a_f, b_f)$

Using the transformation above, we find the factor $\overline{f}_{vx}(z_0)$ for the following flow profiles:

1. For a uniform-flow inlet (near plugged flow):

$$v_u(a, b) = \overline{v}_a(b)$$

   Thus, we obtain:

$$f_{vx}(z) = \frac{v_a(a, b)}{\overline{v}_a(a)} = 1$$

   , and

$$\overline{f}_{vx}(z_0) = 1$$

2. For a parabolic-flow inlet:

$$v_a(a, b) = 2\overline{v}_a\left(1 - b^2\right), 0 \le b \le 1$$

   , where

$$b = \frac{z}{z_0}\left(b_i - b_f\right) + b_f$$

   Thus, we obtain:

$$f_{vx}(z) = \frac{v_a(a, b)}{\overline{v}_a(a)} = 2\left(1 - \left(\frac{z}{z_0}\left(b_i - b_f\right) + b_f\right)^2\right)$$

   , and

$$\overline{f}_{vx}(z_0) = 2\left(1 - b_f^2\right) - 2b_f\left(b_i - b_f\right) - \frac{2}{3}\left(b_i - b_f\right)^2$$

121

$$\overline{f}_{vx}(z_0) = 2 - \frac{2}{3}\left(\frac{b_i^3 - b_f^3}{b_i - b_f}\right)$$

When applied to a tube, as the velocity is in $-ve$ z-direction, we use the notation $\overline{f}_{vz}(r_i)$. Furthermore, for the said system the co-ordinate system corresponds to $(a, b) \equiv (z, r)$, and the normalized quantity $b = r/R$, i.e.

$$\overline{f}_{vz}(r_i) = 2 - \frac{2}{3}\frac{(r_i/R)^3 - (r_0/R)^3}{(r_i/R) - (r_0/R)} = 2 - \frac{2}{3}\frac{r^{*}i^3 - r^{*}0^3}{r^{*}i - r^{*}0}$$

C.6 Uniformity

The deviation in prediction of $r^\dagger f$ for different simulations for all the outermost and inner points, is higher for lower H/R and higher $\log(\alpha\beta)$ values (Figure C.1 and C.2). There is also some relation of the deviation with r^*i values (Figure C.3). The deviation is mainly because of the electric field non-uniformity in the collection region and the overall non0uniformity in COMSOL is nearly reconstructed (Figure C.4)using the individually calculated non-uniformity in particle prediction by FIR and that in electric field calculated using the off-axis electric field equation.
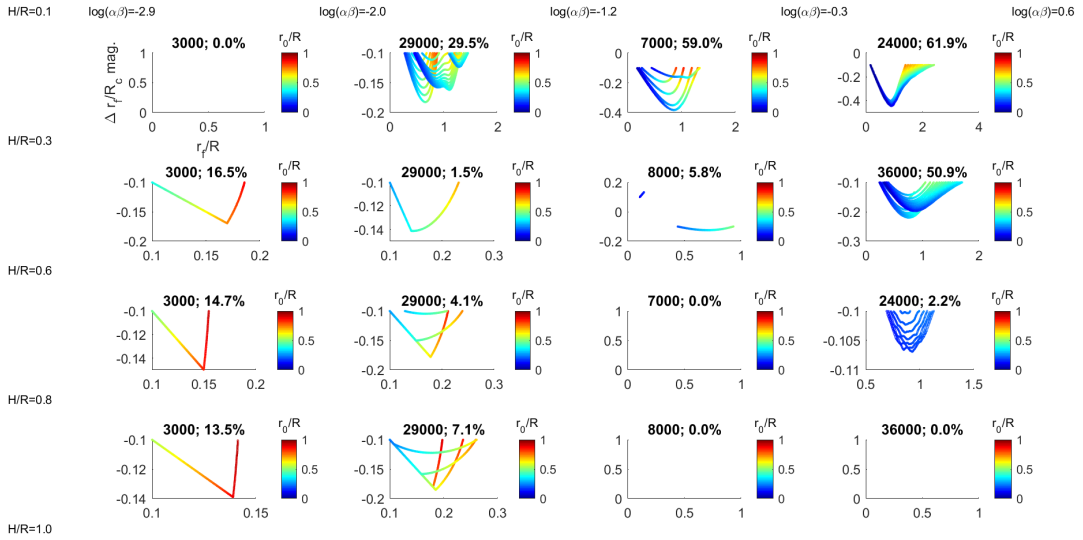
Figure C.1: Deviations between FIR-model calculation of r/R and that obtained from COMSOL simulations for $0.1 \le H/R \le 1$ (divided into four rows) and for $-2.9 \le \log(\alpha\beta) \le 0.6$ (divided into four columns). The points are colored by r^*_{lim} and the absolute deviation in $\Delta r_f/R_c = r^\dagger f, \text{COMSOL} - r^\dagger f, \text{FIR}$ is plotted against the r^*_f (as electric field non-uniformity is related to R). The title of each sub-plot shows the total number of points in that bin and the % shows the portion of those points which have an absolute deviation greater than 10%.

The scaling of the uniformity is done using $\Delta_{max} - \Delta_{r,r^*_{lim}} \Delta_{max} - \Delta_{r,E_0}$. Our estimates show that $\Delta_{max} = 1$, because Δ (MAD/median) of most distributions is generally lower than 1 (Arachchige, Prendergast, and Staudte, 2020). The maximum value of $\Delta_{r,r^*_{lim}}$ was 1 over a large range of shape parameters of a general Weibull distribution (with fixed scale parameter $\lambda = 1$): $\text{WEI}(x, \lambda = 1, k)$.

(a)

(b)
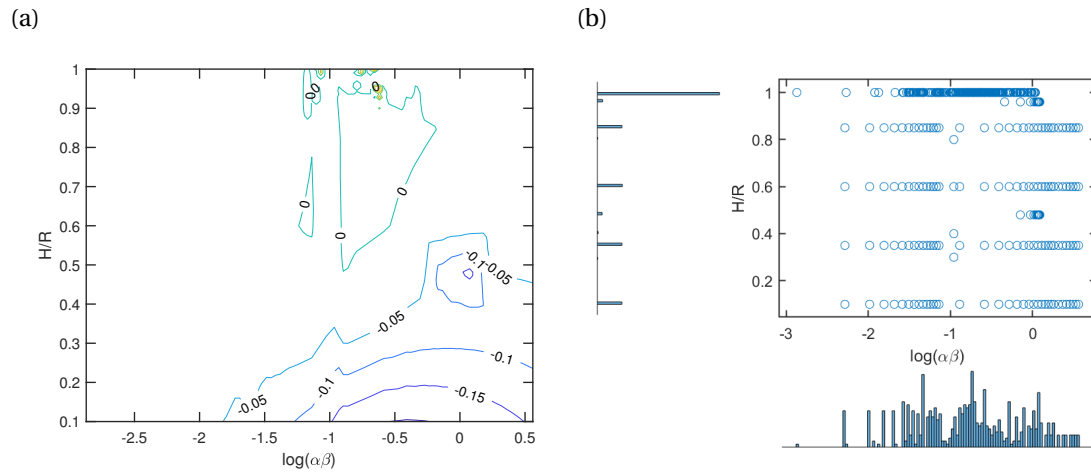
Figure C.2: (a) Contour plot of the deviation (measured as $\Delta r^{\dagger} f = r^{\dagger} f_{\text{FIR}} - r^{\dagger} f_{\text{COMSOL}}$) for different $H/R < 1$ and $\log(\alpha\beta)$ values, formed using (b) the COMSOL simulation pair of values for $H/R < 1$ and $\log(\alpha\beta)$, and the corresponding histogram of the variables.

(a)

(b)
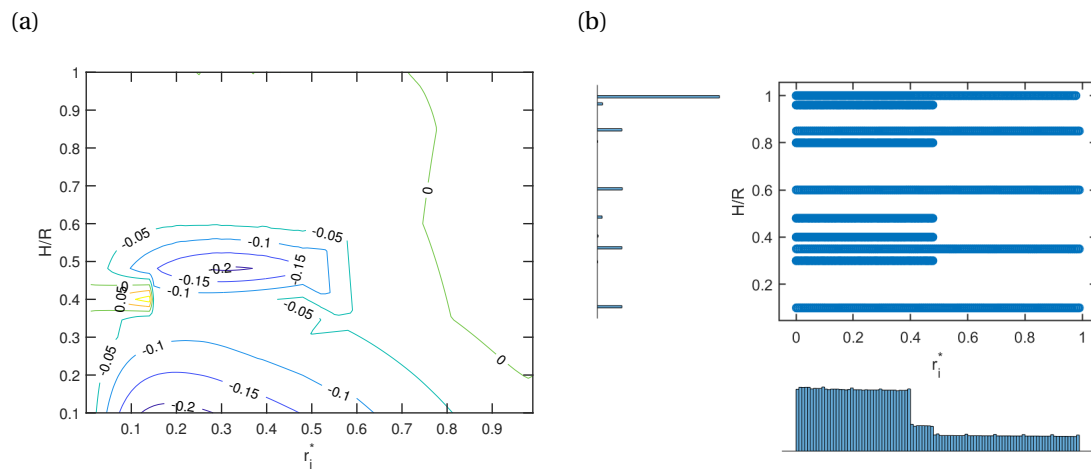
Figure C.3: (a) Contour plot of the deviation (measured as $\Delta r^{\dagger} f = r^{\dagger} f_{\text{FIR}} - r^{\dagger} f_{\text{COMSOL}}$) for different $H/R < 1$ and $r^{*} i$ values, formed using (b) the COMSOL simulation pair of values for $H/R < 1$ and $r^{*} i$, and the corresponding histogram of the variables.

C.7   COMSOL Simulations

The numerical flow simulation can vary by a large margin depending on the flow conditions (Figure C.1).

The particle's z-direction velocity is not same as the observed particle distribution using numerical simulations (Figure C.2).

The z-direction electric field variation in COMSOL provides a useful reference for comparing
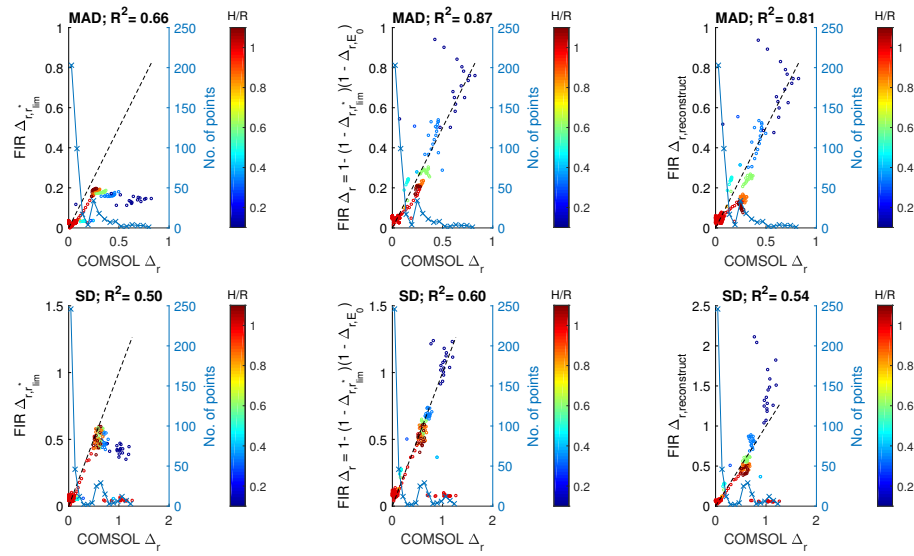
Figure C.4: The first row calculates non-uniformity using MAD/median and the second row uses SD/mean instead. The first column has predictions with only the non-uniformity as obtained from the FIR-model which assumes a constant E_0 for collection. The second column is the reconstructed non-uniformity using that from the FIR-model and that from the change in E_z/E_0 over the collection radius ($r \leq R_c r^\dagger f, \text{max}$). The third column is the non-uniformity of a reconstructed particle deposition profile. The reconstruction is done by multiplying the kernel density of the FIR-predictions with the E_z/E_0 plots.
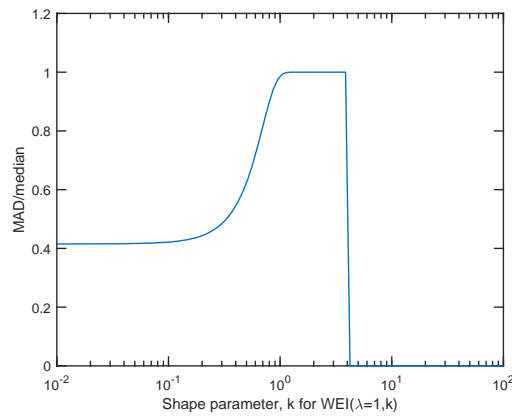
Figure C.5: MAD/median of $WEI(x, \lambda = 1, k)$ against different values of the shape parameter k, where $x$in$[0, 10]$.

the electric field from the off-axis electric field equations that are used for the evaluations (Figure C.3).

(a)

(b)

(c)

(d)
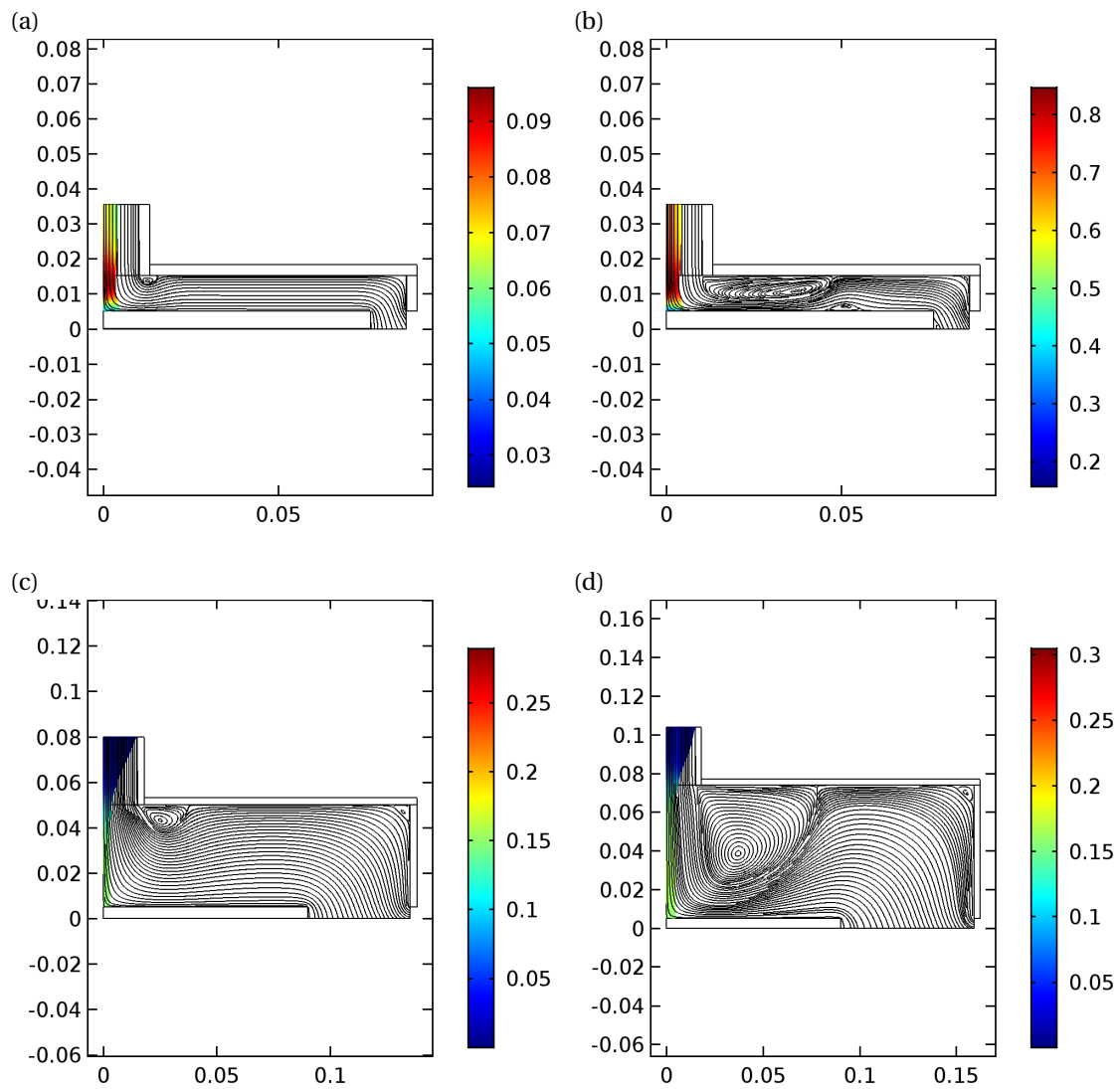
Figure C.1: Different geometries and operating conditions resulting in different flow stream-lines. The flow-field is solved using laminar physics in COMSOL even with the presence of large scale eddies.
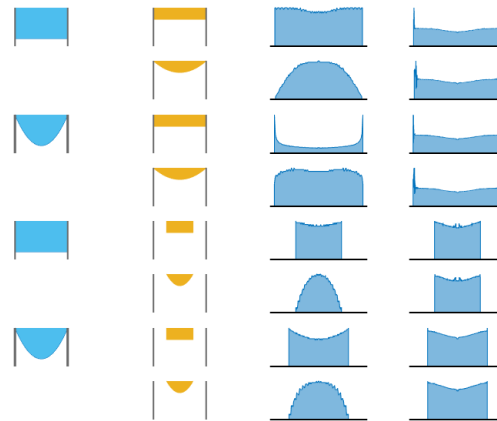
Figure C.2: Comparison of the final particle deposition profile using the particle's z-direction velocity upon collection (right most column) and comparing against the deposition profile from COMSOL simulations (3rd column) for plug-flow inlet or parabolic-flow inlet velocity flow profile (1st column) and for uniform or parabolic particle distribution in the inlet tube, with or without sheath flow (2nd column).
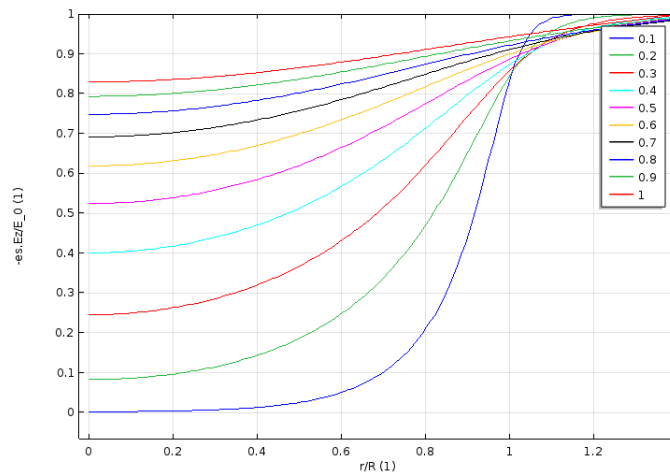
Figure C.3: Normalized z-direction electric field E_z/E_0 at $z/H = 0$ for different H/R values as obtained from COMSOL simulations.

D Appendix to chapter 4

D.1 $\Delta_{r,r^*_{lim}}$ for the local sheath non-uniformity
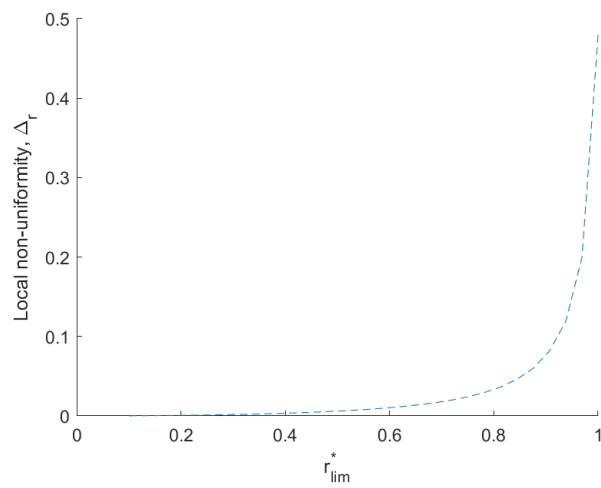
Figure D.1: Local $\Delta_{r,r^*_{lim}}$ over a moving 5% area.

D.2 Δ_{r,E_0} for the electric field non-uniformity

The average and deviation based on Coefficient of variation. Local variation in MAD/median for a moving 5% window through the collection. An estimate of the devaition MAD/median in the regions where that value is 0 (because of 50% of the points having the same value).

(a)

(b)
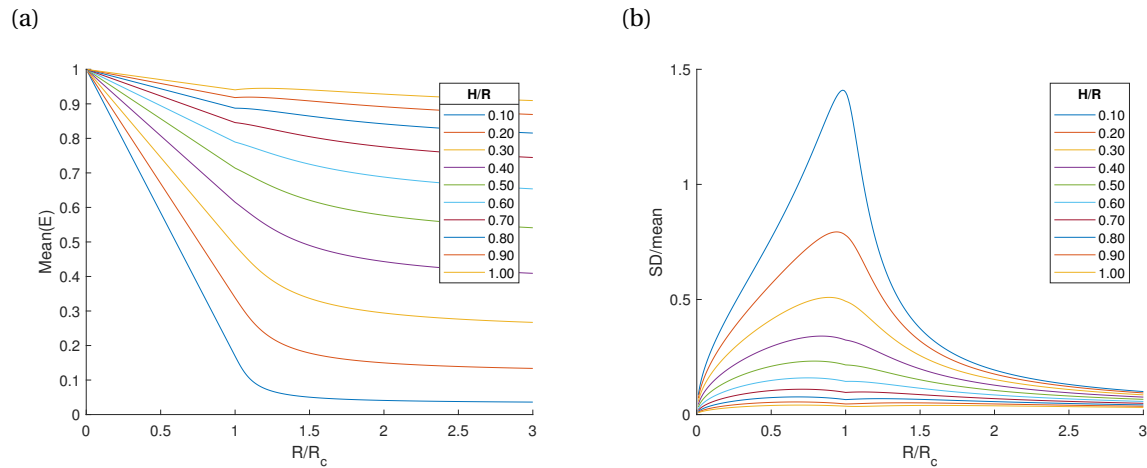
Figure D.1: Change in electric field (a) mean and (b) SD/mean over R_c for different H/R and R/R_c values.

(a)

(b)

(c)
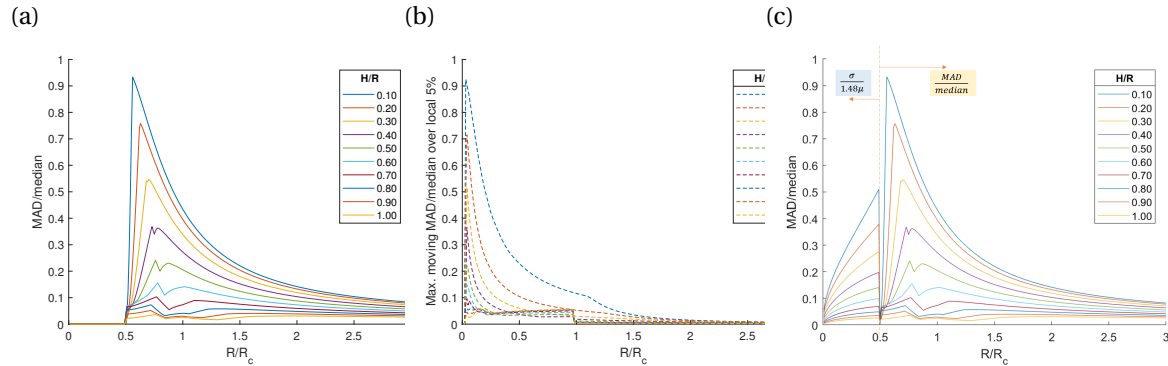
Figure D.2: Change in electric field (a) MAD/median, (b) Maximum MAD/median over a moving local 5% area, (c) over R_c for different H/R and R/R_c values.

D.3 Drift and collection region size-dependence
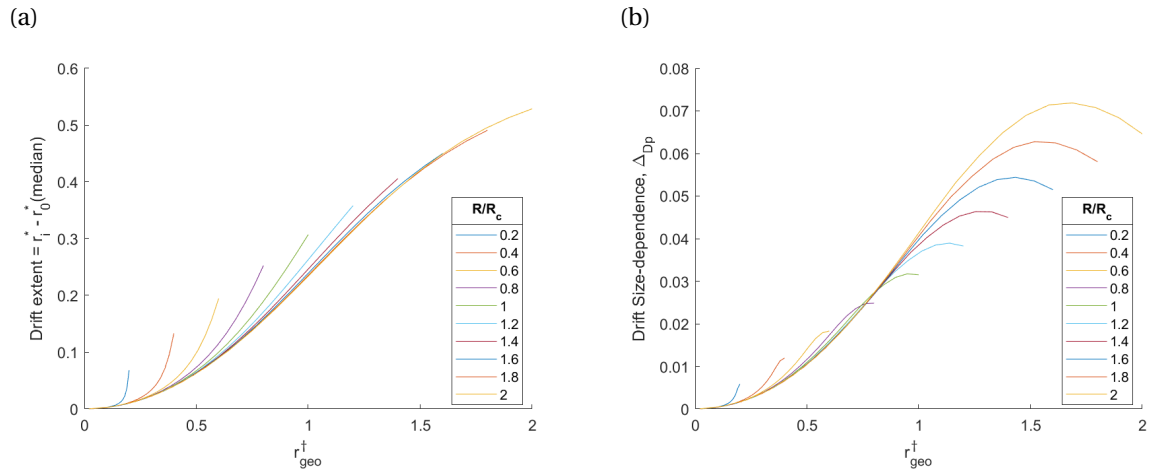
(a)

(b)

Figure D.1: Drift only.

(a)

(b)

Figure D.2: Collector only, for all particle sizes starting from $r_0/R = r_{lim}^*$.

(a)

(b)
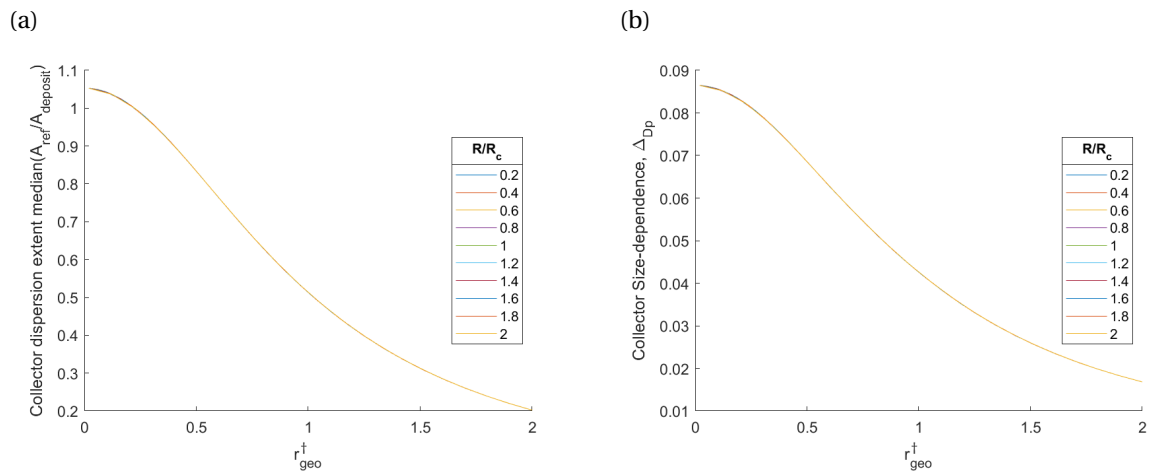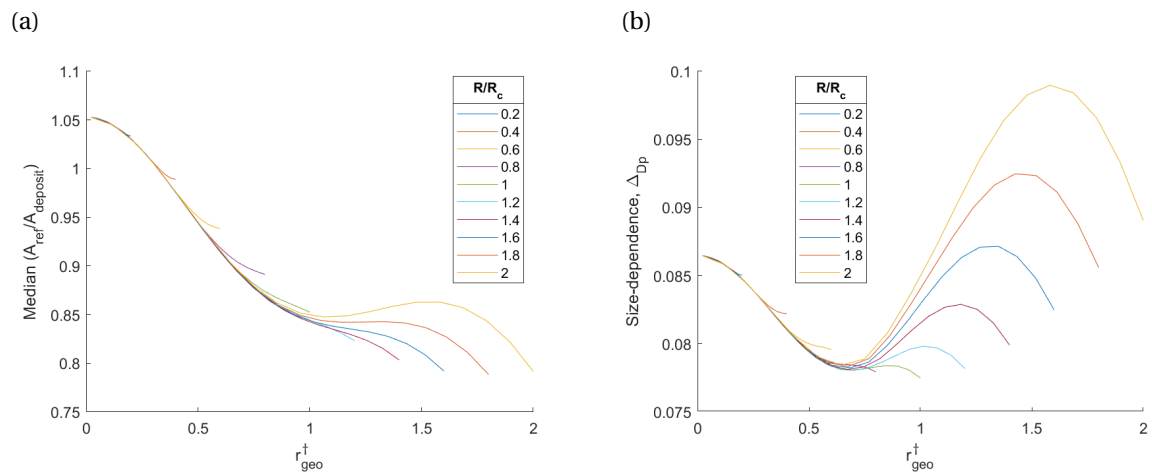
Figure D.3: Final.

D.4 H/R effect on

A lower value of H/R not only results in a more non-uniform electric field strength that changes the spatial uniformity as shown in figure 4.4 but also in a lower average electric field strength over R_c that lowers the collection efficiency. This is visually evident in figure 4.3b ($H/R = 0.25$) where the final particle deposition is more spread out than in figure 4.3a ($H/R = 1$). This is because the high non-uniformity of the electric field strength is coupled with lower values (especially closer to the center), which results in less particle deposition in the region under the tube. A higher H/R is advantageous (concurs with the set value of $H/R = 1$ in Section 4.4.1.2).

(a)

(b)

Figure D.1: Drift only.

(a)

(b)

Figure D.2: Collector only, for all particle sizes starting from $r_0/R = r_{lim}^*$.

(a)

(b)
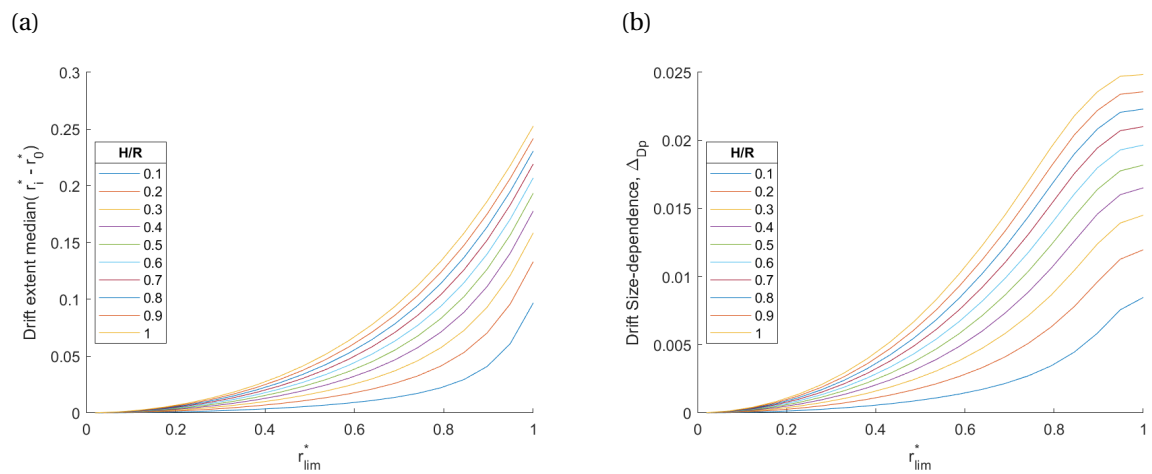
Figure D.3: Final.

D.5   Re and St limits for different r_{lim}^*

(a)

(b)

(c)

(d)
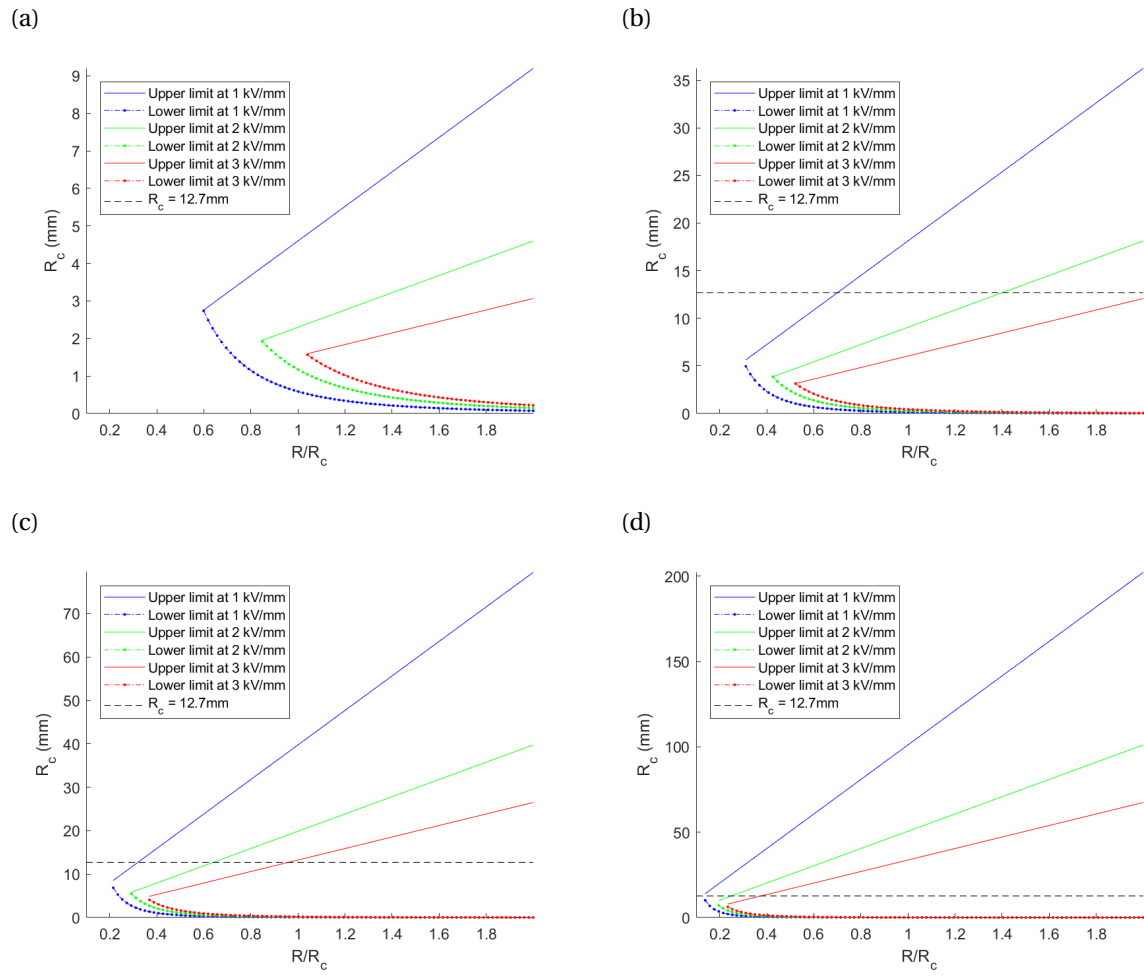
Figure D.1: Similar to Figure 4.11, for (a) $r^*_{lim} = 0.1$, (b) $r^*_{lim} = 0.2$, (c) $r^*_{lim} = 0.3$, (d) $r^*_{lim} = 0.5$.

D.6 φ_{const} and φ_{max} for different R_c and r^*_{lim} values

(a)

(b)

Figure D.1: $\varphi_{\max}$ against (a) R_c and (b) r_{lim}^*.

(a)

(b)
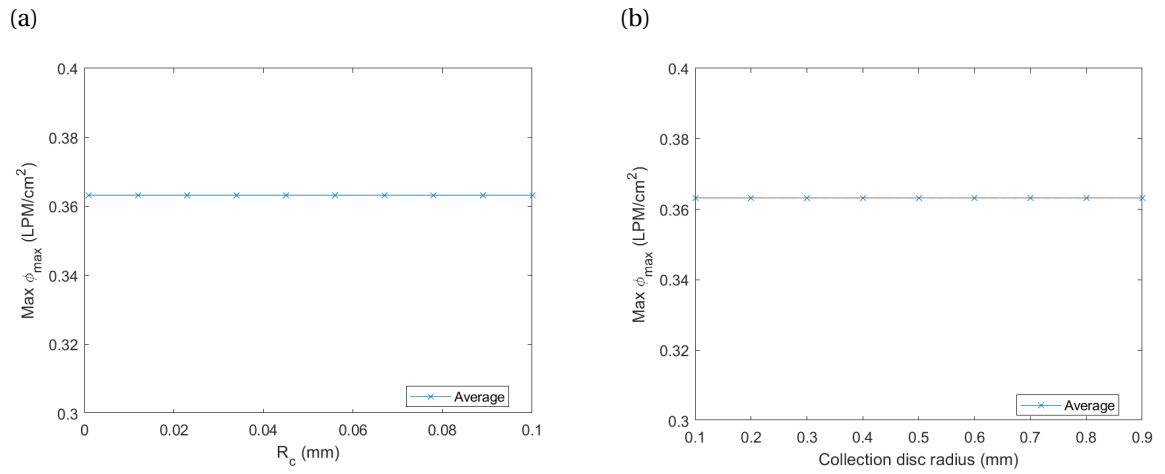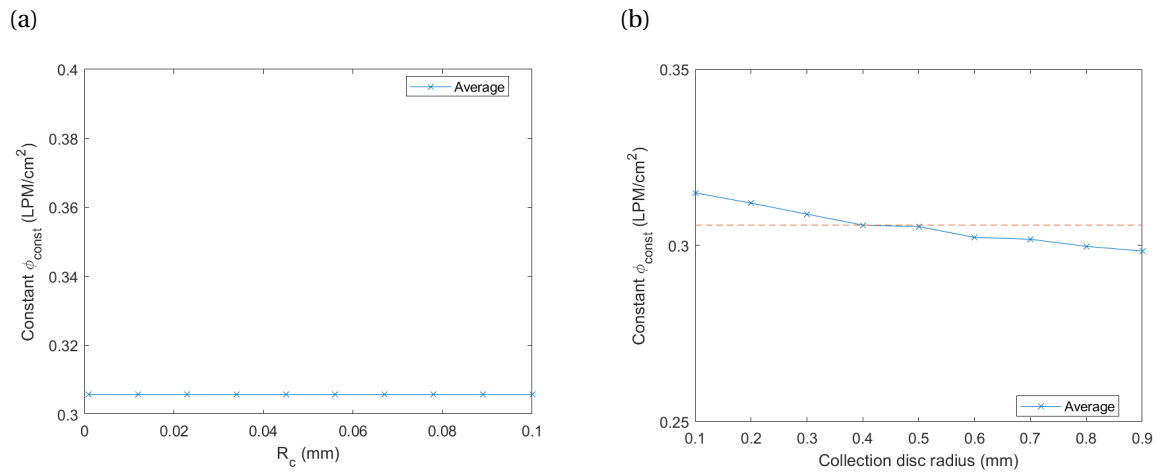
Figure D.2: φ_{const} against (a) R_c and (b) r_{lim}^*.

Bibliography

Adamcyzk, Z. (Jan. 1989). "Particle Deposition from Flowing Suspensions". In: *Colloids and Surfaces* 39.1, pp. 1–37. DOI: 10.1016/0166-6622(89)80176-3.

Adams, F. (1994). "Chemical characterization of atmospheric particles". In: *Topics in atmospheric*, pp. 36–54.

Adamson, A. (1979). *A Textbook of Physical Chemistry 2nd Edition*. Academic Press.

Agency, U. S. E. P. et al. (2011). "Methods for chemical analysis of atmospheric aerosols". In: *Environmental Protection*, pp. 153–177.

Allen, D. T. et al. (1994). "Fourier transform infrared spectroscopy of aerosol collected in a low pressure impactor (LPI/FTIR): Method development and field calibration". In: *Aerosol Science and Technology* 21.4, pp. 325–342. DOI: 10.1080/02786829408959719.

Allen, M. D. and O. G. Raabe (Jan. 1985). "Slip Correction Measurements of Spherical Solid Aerosol Particles in an Improved Millikan Apparatus". In: *Aerosol Science and Technology* 4.3, pp. 269–286. DOI: 10.1080/02786828508959055.

Alonso, M., M. Martin, and F. Alguacil (2006). "The measurement of charging efficiencies and losses of aerosol nanoparticles in a corona charger". In: *Journal of Electrostatics* 64.3, pp. 203–214. DOI: https://doi.org/10.1016/j.elstat.2005.05.008.

Anderson, R. R. et al. (Mar. 2002). "Sources and Composition of PM2.5at the National Energy Technology Laboratory in Pittsburgh during July and August 2000". In: *Energy & Fuels* 16.2, pp. 261–269. DOI: 10.1021/ef010169d.

Arachchige, C. N. P. G., L. A. Prendergast, and R. G. Staudte (Aug. 2020). "Robust analogs to the coefficient of variation". In: *Journal of Applied Statistics*, pp. 1–23. DOI: 10.1080/02664763.2020.1808599.

Arangio, A. et al. (Apr. 2019). "Electrospray Film Deposition for Solvent-Elimination Infrared Spectroscopy". In: *Applied Spectroscopy* 73.6, pp. 638–652. DOI: 10.1177/0003702818821330.

Arangio, A. M. et al. (Oct. 2016). "Quantification of environmentally persistent free radicals and reactive oxygen species in atmospheric aerosol particles". In: *Atmospheric Chemistry and Physics* 16.20, pp. 13105–13119. DOI: 10.5194/acp-16-13105-2016.

Armbruster, D. A. and T. Pry (Aug. 2008). "Limit of blank, limit of detection and limit of quantitation." In: *The Clinical biochemist. Reviews* 29 Suppl 1, S49–S52.

Arnold, S. T., A. A. Viggiano, and R. A. Morris (Dec. 1997). "Rate Constants and Branching Ratios for the Reactions of Selected Atmospheric Primary Cations withn-Octane and Isooctane

(2,2,4-Trimethylpentane)". In: *The Journal of Physical Chemistry A* 101.49, pp. 9351–9358. DOI: 10.1021/jp972106v.

Awad, M. B. and G. S. P. Castle (1975). "Ozone generation in an electrostatic precipitator with a heated corona wire". In: *Journal of the Air Pollution Control Association* 25.4, pp. 369–374. DOI: 10.1080/00022470.1975.10470092.

Bergthorson, J. M. et al. (Dec. 2005). "Impinging laminar jets at moderate Reynolds numbers and separation distances". In: *Physical Review E* 72.6. DOI: 10.1103/physreve.72.066307.

Biskos, G., K. Reavell, and N. Collings (2005). "Unipolar diffusion charging of aerosol particles in the transition regime". In: 36, pp. 247–265. DOI: 10.1016/j.jaerosci.2004.09.002.

Blando, J. D. et al. (1998). "Secondary formation and the Smoky Mountain organic aerosol: An examination of aerosol polarity and functional group composition during SEAVS". In: *Environmental Science and Technology* 32.5, pp. 604–613. DOI: 10.1021/es970405s.

Bohren, C. F. and D. R. Huffman (1983). *Absorption and Scattering of Light by Small Particles*. Wiley Science Series. Wiley.

Bühler, S., D. Obrist, and L. Kleiser (Aug. 2014). "Laminar and turbulent nozzle-jet flows and their acoustic near-field". In: *Physics of Fluids* 26.8, p. 086103. DOI: 10.1063/1.4890493.

Burtscher, H. et al. (1982). "Probing aerosols by photoelectric charging". In: 3787. DOI: 10.1063/1.331120.

Caroff, M., K. Choudhary, and J. Gentry (Mar. 1973). "Effect of pore and particle size distribution on efficiencies of membrane filters". In: *Journal of Aerosol Science* 4.2, pp. 93–102. DOI: 10.1016/0021-8502(73)90061-x.

Casuccio, G. S. et al. (June 2004). "Measurement of fine particulate matter using electron microscopy techniques". In: *Fuel Processing Technology* 85.6-7, pp. 763–779. DOI: 10.1016/j.fuproc.2003.11.026.

Centre., E. C. J. R. (2016). *Guidance document on the estimation of LOD and LOQ for measurements in the field of contaminants in feed and food.* Publications Office. DOI: 10.2787/8931.

Cheng, Y. and S.-M. Li (Apr. 2004). "Analytical method development of long-chain ketones in PM2.5aerosols using accelerated solvent extraction and Gc/FID/MSD". In: *International Journal of Environmental Analytical Chemistry* 84.5, pp. 367–378. DOI: 10.1080/03067310310001638320.

Chippett, S. and W. Gray (1978). "The size and optical properties of soot particles". In: *Combustion and Flame* 31, pp. 149–159. DOI: 10.1016/0010-2180(78)90125-6.

Chow, J. C. (May 1995). "Measurement Methods to Determine Compliance with Ambient Air Quality Standards for Suspended Particles". In: *Journal of the Air & Waste Management Association* 45.5, pp. 320–382. DOI: 10.1080/10473289.1995.10467369.

Christiansen, E. B. and H. E. Lemmon (Nov. 1965). "Entrance region flow". In: *AIChE Journal* 11.6, pp. 995–999. DOI: 10.1002/aic.690110610.

Cooper, D. W., M. H. Peters, and R. J. Miller (Jan. 1989). "Predicted Deposition of Submicrometer Particles Due to Diffusion and Electrostatics in Viscous Axisymmetric Stagnation-Point Flow". In: *Aerosol Science and Technology* 11.2, pp. 133–143. DOI: 10.1080/02786828908959306.

Cooperman, P. (July 1971). "A new theory of precipitator efficiency". In: *Atmospheric Environment (1967)* 5.7, pp. 541–551. DOI: 10.1016/0004-6981(71)90064-3.

Coury, C. and A. M. Dillner (2008). "A method to quantify organic functional groups and inorganic compounds in ambient aerosols using attenuated total reflectance FTIR spectroscopy and multivariate chemometric techniques". In: *Atmospheric Environment* 42.23, pp. 5923–5932. DOI: 10.1016/j.atmosenv.2008.03.026.

Cunningham, P. T. (n.d.). ":
NL-81-12 ANALYTICAL TECHNIQUES FOR AMBIENT SULFATE AEROSOLS by". In: ().

DeCarlo, P. F. et al. (Jan. 2004). "Particle Morphology and Density Characterization by Combined Mobility and Aerodynamic Diameter Measurements. Part 1: Theory". In: *Aerosol Science and Technology* 38.12, pp. 1185–1205. DOI: 10.1080/027868290903907.

Deutsch, W. (1922). "Bewegung und Ladung der Elektrizitätsträger im Zylinderkondensator". In: *Annalen der Physik* 373.12, pp. 335–344. DOI: 10.1002/andp.19223731203.

Dick, C. A. J. et al. (June 2003). "Murine Pulmonary Inflammatory Responses Following Instillation of Size-Fractionated Ambient Particulate Matter". In: *Journal of Toxicology and Environmental Health, Part A* 66.23, pp. 2193–2207. DOI: 10.1080/716100636.

Dillner, A. M. and S. Takahama (Mar. 2015a). "Predicting ambient aerosol thermal-optical reflectance (TOR) measurements from infrared spectra: organic carbon". In: *Atmospheric Measurement Techniques* 8.3, pp. 1097–1109. DOI: 10.5194/amt-8-1097-2015.

— (Oct. 2015b). "Predicting ambient aerosol thermal–optical reflectance measurements from infrared spectra: elemental carbon". In: *Atmospheric Measurement Techniques* 8.10, pp. 4013–4023. DOI: 10.5194/amt-8-4013-2015.

Dixkens, J. and H. Fissan (1991). "Electrostatic particle sampler for total-reflection X-ray fluorescence analysis". In: *Journal of Aerosol Science* 22, S375–S378. DOI: 10.1016/s0021-8502(05)80116-8.

— (May 1999). "Development of an Electrostatic Precipitator for Off-Line Particle Analysis". In: *Aerosol Science and Technology* 30.5, pp. 438–453. DOI: 10.1080/027868299304480.

Domat, M., F. E. Kruis, and J. M. Fernandez-Diaz (2014). "Investigations of the effect of electrode gap on the performance of a corona charger having separated corona and charging zones". In: *Journal of Aerosol Science* 68, pp. 1–13. DOI: 10.1016/j.jaerosci.2013.08.017.

Dron, J. et al. (2010). "Functional group composition of ambient and source organic aerosols determined by tandem mass spectrometry". In: *Atmospheric Chemistry and Physics* 10.15, pp. 7041–7055. DOI: 10.5194/acp-10-7041-2010.

Dudani, N. and S. Takahama (2021a). "Design of an electrostatic aerosol collector part 1: dimensionless analytical model for mapping inlet particle positions to collection surface". In: *Manuscript in preparation.* ENAC/IIE Swiss Federal Institute of Technology Lausanne (EPFL).

— (2021b). "Design of an electrostatic aerosol collector part 2: design for poly-dispersed aerosol collection for spectroscopy analysis". In: *Manuscript in preparation.* ENAC/IIE Swiss Federal Institute of Technology Lausanne (EPFL).

Durand, T. et al. (2014). "Quantification of Low Pressure Impactor Wall Deposits during Zinc Nanoparticle Sampling". In: *Aerosol and Air Quality Research* 14.7, pp. 1812–1821. DOI: 10.4209/aaqr.2013.10.0304.

Dzubay, T., L. Hines, and R. Stevens (Jan. 1976). "Particle bounce errors in cascade impactors". In: *Atmospheric Environment (1967)* 10.3, pp. 229–234. DOI: 10.1016/0004-6981(76)90095-0.

Earle, M. E. et al. (Dec. 2006). "Temperature-Dependent Complex Indices of Refraction for Crystalline (NH4)2SO4". In: *The Journal of Physical Chemistry A* 110.48, pp. 13022–13028. DOI: 10.1021/jp064704s.

Emery, A. F. and C. S. Chen (Mar. 1968). "An Experimental Investigation of Possible Methods to Reduce Laminar Entry Lengths". In: *Journal of Basic Engineering* 90.1, pp. 134–137. DOI: 10.1115/1.3605053.

Esmen, N. A. and T. C. Lee (June 1980). "Distortion of cascade impactor measured size distribution due to bounce and blow-off". In: *American Industrial Hygiene Association Journal* 41.6, pp. 410–419. DOI: 10.1080/15298668091424951.

Fargie, D. and B. W. Martin (1971). "Developing laminar flow in a pipe of circular cross-section". In: *Proc. Roy. Soc. A.* 301.1413, pp. 355–361.

Fichman, M., D. Pnueli, and C. Gutfinger (Jan. 1990). "Aerosol Deposition in the Vicinity of a Stagnation Point". In: *Aerosol Science and Technology* 13.3, pp. 281–296. DOI: 10.1080/02786829008959445.

Fierz, M. (May 2007). "Theoretical and Experimental Evaluation of a Portable Electrostatic TEM Sampler". In: *Aerosol Science and Technology* 41, pp. 520–528. DOI: 10.1080/02786820701253327.

Fletcher, R. A. et al. (2011). "Microscopy and Microanalysis of Individual Collected Particles". In: *Aerosol Measurement: Principles, Techniques, and Applications: Third Edition*, pp. 179–232. DOI: 10.1002/9781118001684.ch10.

Foat, T. et al. (May 2016). "A prototype personal aerosol sampler based on electrostatic precipitation and electrowetting-on-dielectric actuation of droplets". In: *Journal of Aerosol Science* 95, pp. 43–53. DOI: 10.1016/j.jaerosci.2016.01.007.

Furuuchi, M. et al. (2010). "Development and Performance Evaluation of Air Sampler with Inertial Filter for Nanoparticle Sampling". In: *Aerosol and Air Quality Research* 10.2, pp. 185–192. DOI: 10.4209/aaqr.2009.11.0070.

Ghauch, A. et al. (2006). "Use of FTIR spectroscopy coupled with ATR for the determination of atmospheric compounds". In: *Talanta* 68.4, pp. 1294–1302. DOI: 10.1016/j.talanta.2005.07.046.

Gomes, M. et al. (July 1993). "Convective and diffusive dispersion of particles in laminar tube flow: Effects on time-dependent concentration measurements". In: *Journal of Aerosol Science* 24.5, pp. 643–654. DOI: 10.1016/0021-8502(93)90021-z.

Greaves, R. C., R. M. Barkley, and R. E. Sievers (Dec. 1985). "Rapid sampling and analysis of volatile constituents of airborne particulate matter". In: *Analytical Chemistry* 57.14, pp. 2807–2815. DOI: 10.1021/ac00291a015.

Grob, B., H. Burtscher, and R. Niessner (2013). "Charging of ultra-fine aerosol particles by an ozone-free indirect uv photo-charger". In: *Aerosol Science and Technology* 47.12, pp. 1325–1333. DOI: 10.1080/02786826.2013.840357.

Grob, B., J. C. Wolf, et al. (2014). "Calibration system with an indirect photoelectric charger for legislated vehicle number emission measurement counters in the single counting mode". In: *Journal of Aerosol Science* 70, pp. 50–58. DOI: 10.1016/j.jaerosci.2014.01.001.

Gun, J., R. Iscovici, and J. Sagiv (Sept. 1984). "On the formation and structure of self-assembling monolayers : II. A comparative study of Langmuir—Blodgett and adsorbed films using ellipsometry and IR reflection—absorption spectroscopy". In: *Journal of Colloid and Interface Science* 101.1, pp. 201–213. DOI: 10.1016/0021-9797(84)90020-1.

Hallquist, M. et al. (2009). "The formation, properties and impact of secondary organic aerosol: current and emerging issues". In: *Atmos. Chem. Phys.* 9.14, pp. 5155–5236. DOI: 10.5194/acp-9-5155-2009.

Han, B. et al. (2008). "Unipolar Charging of Fine and Ultra-Fine Particles Using Carbon Fiber Ionizers Unipolar Charging of Fine and Ultra-Fine Particles Using Carbon Fiber Ionizers". In: 6826. DOI: 10.1080/02786820802339553.

Han, T., D. Fennell, and G. Mainelis (Feb. 2015). "Development and Optimization of the Electrostatic Precipitator with Superhydrophobic Surface (EPSS) Mark II for Collection of Bioaerosols". In: *Aerosol Science and Technology* 49.4, pp. 210–219. DOI: 10.1080/02786826.2015.1017040.

Han, T. T., N. M. Thomas, and G. Mainelis (2017). "Design and development of a self-contained personal electrostatic bioaerosol sampler (PEBS) with a wire-to-wire charger". In: *Aerosol Science and Technology* 51.8, pp. 903–915. DOI: 10.1080/02786826.2017.1329516.

Hapke, B. (Nov. 2012). "Bidirectional reflectance spectroscopy 7". In: *Icarus* 221.2, pp. 1079–1083. DOI: 10.1016/j.icarus.2012.10.022.

Harrick, N. J. and K. H. Beckmann (1974). "Internal Reflection Spectroscopy". In: *Characterization of Solid Surfaces*. Ed. by P. F. Kane and G. B. Larrabee. Boston, MA: Springer US, pp. 215–245. DOI: 10.1007/978-1-4613-4490-2_11.

Heiszler, M. (1971). "Analysis of streamer propagation in atmospheric air". In.

Hewitt, G. W. (1957). "The charging of small particles for electrostatic precipitation Part I: Communication and Electronics, Transactions of the". In: *American Institute of Electrical Engineers* 76.3, pp. 300–306. DOI: 10.1109/TCE.1957.6372672.

Hinds, W. C. (1999). *Aerosol Technology: Properties, Behavior, and Measurement of Airborne Particles*. Wiley-Interscience.

Hobbs, P. V. (1993). "Chapter 2 Aerosol-Cloud Interactions". In: *International Geophysics*. Elsevier, pp. 33–73. DOI: 10.1016/s0074-6142(08)60211-9.

Hontañón, E. and F. E. Kruis (2008). "Single Charging of Nanoparticles by UV Photoionization at High Flow Rates". In: *Aerosol Science and Technology* 42.4, pp. 310–323. DOI: 10.1080/02786820802054244.

Hulst, H. C. van de (1957). *Light Scattering by Small Particles*. Dover Publications Inc.

Hung, H.-M., Y.-Q. Chen, and S. T. Martin (Dec. 2012). "Reactive Aging of Films of Secondary Organic Material Studied by Infrared Spectroscopy". In: *The Journal of Physical Chemistry A* 117.1, pp. 108–116. DOI: 10.1021/jp309470z.

Bibliography

Iida, K. et al. (June 2017). "Aerosol-to-liquid collection: A method for making aqueous suspension of hydrophobic nanomaterial without adding dispersant". In: *Aerosol Science and Technology* 51.10, pp. 1144–1157. DOI: 10.1080/02786826.2017.1337868.

Intra, P. and N. Tippayawong (2011). "An overview of unipolar charger developments for nanoparticle charging". In: *Aerosol and Air Quality Research* 11.2, pp. 187–209. DOI: 10.4209/aaqr.2010.10.0082.

Jack, H. (2013). "Mechanical Design". In: *Engineering Design, Planning, and Management*. Elsevier, pp. 469–545. DOI: 10.1016/b978-0-12-397158-6.00012-7.

Jiménez, O. P., R. M. Pastor, and S. G. Alonso (2010). "Assessment uncertainty associated to the analysis of organic compounds linked to particulate matter of atmospheric aerosols". In: *Talanta* 80.3, pp. 1121–1128. DOI: 10.1016/j.talanta.2009.08.036.

Jodzis, S. and W. Patkowski (2016). "Kinetic and Energetic Analysis of the Ozone Synthesis Process in Oxygen-fed DBD Reactor. Effect of Power Density, Gap Volume and Residence Time". In: *Ozone: Science and Engineering* 38.2, pp. 86–99. DOI: 10.1080/01919512.2015.1128320.

Johnson, T. J. et al. (June 2020). "Infrared Optical Constants from Pressed Pellets of Powders: I. Improved n and k Values of (NH4)2SO4 from Single-Angle Reflectance". In: *Applied Spectroscopy* 74.8, pp. 851–867. DOI: 10.1177/0003702820930009.

Kala, S. et al. (2012). "Synthesis and Film Formation of Monodisperse Nanoparticles and Nanoparticle Pairs". In: *Nanoparticles from the Gasphase*. Springer Berlin Heidelberg, pp. 99–119. DOI: 10.1007/978-3-642-28546-2_4.

Kaminski, H. et al. (June 2012). "Mathematical Description of Experimentally Determined Charge Distributions of a Unipolar Diffusion Charger". In: *Aerosol Science and Technology* 46.6, pp. 708–716. DOI: 10.1080/02786826.2012.659360.

Kelley, A. M. (2012). *Condensed-Phase Molecular Spectroscopy and Photophysics*. Wiley.

Kim, S., H. Park, and K. Lee (Feb. 2001). "Theoretical model of electrostatic precipitator performance for collecting polydisperse particles". In: *Journal of Electrostatics* 50.3, pp. 177–190. DOI: 10.1016/s0304-3886(00)00035-8.

Kim, S., C. Sioutas, and M. Chang (Mar. 2000). "Electrostatic Enhancement of the Collection Efficiency of Stainless Steel Fiber Filters". In: *Aerosol Science and Technology* 32.3, pp. 197–213. DOI: 10.1080/027868200303731.

Kimoto, S. et al. (2010). "A small mixing-type unipolar charger (SMUC) for nanoparticles". In: *Aerosol Science and Technology* 44.10, pp. 872–880. DOI: 10.1080/02786826.2010.498796.

Kuzmiakova, A., A. M. Dillner, and S. Takahama (June 2016). "An automated baseline correction protocol for infrared spectra of atmospheric aerosols collected on polytetrafluoroethylene (Teflon) filters". In: *Atmospheric Measurement Techniques* 9.6, pp. 2615–2631. DOI: 10.5194/amt-9-2615-2016.

Kwon, S. B., H. Sakurai, and T. Seto (2007). "Unipolar charging of nanoparticles by the Surface-discharge Microplasma Aerosol Charger (SMAC)". In: *Journal of Nanoparticle Research* 9.4, pp. 621–630. DOI: 10.1007/s11051-006-9117-2.

Lai, C.-Y. et al. (Jan. 2002). "Overall Performance Evaluation of Aerosol Number Samplers". In: *Aerosol Science and Technology* 36.1, pp. 84–95. DOI: 10.1080/027868202753339104.

Lai, R. and G. R. Gavalas (Nov. 1998). "Surface Seeding in ZSM-5 Membrane Preparation". In: *Industrial & Engineering Chemistry Research* 37.11, pp. 4275–4283. DOI: 10.1021/ie980265a.

Laskina, O. et al. (Apr. 2014). "Infrared Optical Constants of Organic Aerosols: Organic Acids and Model Humic-Like Substances (HULIS)". In: *Aerosol Science and Technology* 48.6, pp. 630–637. DOI: 10.1080/02786826.2014.904499.

Le, T.-C., G.-Y. Lin, and C.-J. Tsai (2013). "The Predictive Method for the Submicron and Nano-Sized Particle Collection Efficiency of Multipoint-to-Plane Electrostatic Precipitators". In: *Aerosol and Air Quality Research* 13.5, pp. 1404–1410. DOI: 10.4209/aaqr.2013.05.0144.

Lee, D., M. F. Rubner, and R. E. Cohen (Oct. 2006). "All-Nanoparticle Thin-Film Coatings". In: *Nano Letters* 6.10, pp. 2305–2312. DOI: 10.1021/nl061776m.

Leonard, G., M. Mitchner, and S. Self (Jan. 1982). "Experimental study of the effect of turbulent diffusion on precipitator efficiency". In: *Journal of Aerosol Science* 13.4, pp. 271–284. DOI: 10.1016/0021-8502(82)90030-1.

Li, C. et al. (May 2006). "Cathode materials modified by surface coating for lithium ion batteries". In: *Electrochimica Acta* 51.19, pp. 3872–3883. DOI: 10.1016/j.electacta.2005.11.015.

Lidén, G. (1994). "Performance parameters for assessing the acceptability of aerosol sampling equipment". In: *The Analyst* 119.1, pp. 27–33. DOI: 10.1039/an9941900027.

Liland, K. H., T. AlmÃ¸y, and B. Mevik (Sept. 2010). "Optimal Choice of Baseline Correction for Multivariate Calibration of Spectra". EN. In: *Applied Spectroscopy* 64.9, pp. 1007–1016.

Liu, B. Y. H. and D. Y. H. Pui (1975). "LIU and DAVID". In: 6.

Liu, B. Y. H., K. T. Whitby, and H. H. S. Yu (Jan. 1967). "Electrostatic Aerosol Sampler for Light and Electron Microscopy". In: *Review of Scientific Instruments* 38.1, pp. 100–102. DOI: 10.1063/1.1720491.

Liu, C.-N. et al. (Mar. 2014). "Sampling and conditioning artifacts of PM2.5 in filter-based samplers". In: *Atmospheric Environment* 85, pp. 48–53. DOI: 10.1016/j.atmosenv.2013.11.075.

Liu, P. et al. (Jan. 1995). "Generating Particle Beams of Controlled Dimensions and Divergence: I. Theory of Particle Motion in Aerodynamic Lenses and Nozzle Expansions". In: *Aerosol Science and Technology* 22.3, pp. 293–313. DOI: 10.1080/02786829408959748.

Ma, Z. et al. (May 2016). "Development of an integrated microfluidic electrostatic sampler for bioaerosol". In: *Journal of Aerosol Science* 95, pp. 84–94. DOI: 10.1016/j.jaerosci.2016.01.003.

Mahamuni, G., B. Ockerman, and I. Novosselov (Apr. 2019). "Electrostatic capillary collector for in-situ spectroscopic analysis of aerosols". In: *Aerosol Science and Technology* 53.6, pp. 688–700. DOI: 10.1080/02786826.2019.1600653.

Maidment, L. et al. (July 2018). "Systematic spectral shifts in the mid-infrared spectroscopy of aerosols". In: *Optics Express* 26.15, p. 18975. DOI: 10.1364/oe.26.018975.

Maoz, R. and J. Sagiv (Aug. 1984). "On the formation and structure of self-assembling monolayers. I. A comparative atr-wettability study of Langmuir—Blodgett and adsorbed films on flat substrates and glass microbeads". In: *Journal of Colloid and Interface Science* 100.2, pp. 465–496. DOI: 10.1016/0021-9797(84)90452-1.

Bibliography

Maria, S. F. et al. (2002). "FTIR measurements of functional groups and organic mass in aerosol samples over the Caribbean". In: *Atmospheric Environment* 36.33, pp. 5185–5196. DOI: 10.1016/S1352-2310(02)00654-4.

Marple, V. A. (Mar. 2004). "History of Impactors—The First 110 Years". In: *Aerosol Science and Technology* 38.3, pp. 247–292. DOI: 10.1080/02786820490424347.

Marple, V. A., K. L. Rubow, and S. M. Behm (Jan. 1991). "A Microorifice Uniform Deposit Impactor (MOUDI): Description, Calibration, and Use". In: *Aerosol Science and Technology* 14.4, pp. 434–446. DOI: 10.1080/02786829108959504.

Marple, V. A., K. L. Rubow, and B. A. Olson (Jan. 1995). "Diesel Exhaust/Mine Dust Virtual Impactor Personal Aerosol Sampler: Design, Calibration and Field Evaluation". In: *Aerosol Science and Technology* 22.2, pp. 140–150. DOI: 10.1080/02786829408959735.

Marquard, A. (May 2007). "Unipolar Field and Diffusion Charging in the Transition Regime—Part I: A 2-D Limiting-Sphere Model". In: *Aerosol Science and Technology* 41.6, pp. 597–610. DOI: 10.1080/02786820701272053.

Marquard, A., J. Meyer, and G. Kasper (2006). "Characterization of unipolar electrical aerosol chargers-Part II:. Application of comparison criteria to various types of nanoaerosol charging devices". In: *Journal of Aerosol Science* 37.9, pp. 1069–1080. DOI: 10.1016/j.jaerosci.2005.09.002.

Mayo, D. W., F. A. Miller, and R. W. Hannah, eds. (May 2004). *Course Notes on the Interpretation of Infrared and Raman Spectra.* p.333. John Wiley & Sons, Inc. DOI: 10.1002/0471690082.

McDonald, R. and P. Biswas (Sept. 2004). "A Methodology to Establish the Morphology of Ambient Aerosols". In: *Journal of the Air & Waste Management Association* 54.9, pp. 1069–1078. DOI: 10.1080/10473289.2004.10470986.

McKeown, P. J., M. V. Johnston, and D. M. Murphy (Sept. 1991). "On-line single-particle analysis by laser desorption mass spectrometry". In: *Analytical Chemistry* 63.18, pp. 2069–2073. DOI: 10.1021/ac00018a033.

Medved, A. et al. (2000). "A new corona-based charger for aerosol particles". In: *Journal of Aerosol Science* 31.1994, pp. 616–617. DOI: 10.1016/S0021-8502(00)90625-6.

Mercer, T., M. Tillery, and G. Newton (Feb. 1970). "A multi-stage, low flow rate cascade impactor". In: *Journal of Aerosol Science* 1.1, pp. 9–15. DOI: 10.1016/0021-8502(70)90024-8.

Michaelis, H. (Dec. 1890). "Prüfung der Wirksamkeit von Staubrespiratoren". In: *Zeitschrift für Hygiene* 9.1, pp. 389–394. DOI: 10.1007/bf02187951.

Miloslav N., J. J. and B. K. (2014). *IUPAC Compendium of Chemical Terminology- the Gold Book,* ed. by M. Nič et al. DOI: https://doi.org/10.1351/goldbook.

Mishchenko, M. I. (1990). "Extinction of light by randomly-oriented non-spherical grains". In: *Astrophysics and Space Science* 164.1, pp. 1–13. DOI: 10.1007/bf00653546.

Modey, W. (Dec. 2001). "Fine particulate (PM2.5) composition in Atlanta, USA: assessment of the particle concentrator-Brigham Young University organic sampling system, PC-BOSS, during the EPA supersite study". In: *Atmospheric Environment* 35.36, pp. 6493–6502. DOI: 10.1016/s1352-2310(01)00402-2.

Monks, P. S. et al. (2009). "Atmospheric composition change - global and regional air quality". In: *Atmospheric Environment* 43.33, pp. 5268–5350. DOI: 10.1016/j.atmosenv.2009.08.021.

Monnett, O. ; (1920). "Determination of atmospheric impurities I , II ." In: *Chem . ' Met . Eng . , 23 , 1117-21 , 1173-6.*

Montassier, N., L. Dupin, and D. Boulaud (Sept. 1996). "Experimental study on the collection efficiency of membrane filters". In: *Journal of Aerosol Science* 27, S637–S638. DOI: 10.1016/0021-8502(96)00391-6.

Montgomery, J. et al. (Sept. 1992). "Novel materials for the semiconductor industry, deposited using a rapid thermal chemical vapour deposition system". In: *Journal of Materials Processing Technology* 33.4, pp. 481–492. DOI: 10.1016/0924-0136(92)90281-v.

Myers, T. L. et al. (June 2020). "Improved Infrared Optical Constants from Pressed Pellets: II. Ellipsometric n and k Values for Ammonium Sulfate with Variability Analysis". In: *Applied Spectroscopy* 74.8, pp. 868–882. DOI: 10.1177/0003702820928358.

Nishida, R. T., A. M. Boies, and S. Hochgreb (2018). "Measuring ultrafine aerosols by direct photoionization and charge capture in continuous flow". In: *Aerosol Science and Technology* 52.5, pp. 546–556. DOI: 10.1080/02786826.2018.1430350.

Novosselov, I. V. et al. (July 2014). "Design and Performance of a Low-Cost Micro-Channel Aerosol Collector". In: *Aerosol Science and Technology* 48.8, pp. 822–830. DOI: 10.1080/02786826.2014.932895.

Ofner, J., H.-U. Krüger, et al. (2009). "Direct Deposition of Aerosol Particles on an ATR Crystal for FTIR Spectroscopy Using an Electrostatic Precipitator". In: *Aerosol Science and Technology* 43.8, pp. 794–798. DOI: 10.1080/02786820902946612.

Ofner, J., H. U. Kruger, et al. (2011). "Physico-chemical characterization of SOA derived from catechol and guaiacol - A model substance for the aromatic fraction of atmospheric HULIS". In: *Atmospheric Chemistry and Physics* 11.1, pp. 1–15. DOI: 10.5194/acp-11-1-2011.

Öktem, B., M. P. Tolocka, and M. V. Johnston (Jan. 2004). "On-Line Analysis of Organic Components in Fine and Ultrafine Particles by Photoionization Aerosol Mass Spectrometry". In: *Analytical Chemistry* 76.2, pp. 253–261. DOI: 10.1021/ac0350559.

Organization, W. H. (2016). *Ambient air pollution: A global assessment of exposure and burden of disease.*

Pandis, S. N. et al. (2013). "Introductory lecture: Atmospheric organic aerosols: insights from the combination of measurements and chemical transport models". In: *Faraday Discussions* 165, p. 9. DOI: 10.1039/c3fd00108c.

Pardon, G. et al. (June 2015). "Aerosol sampling using an electrostatic precipitator integrated with a microfluidic interface". In: *Sensors and Actuators B: Chemical* 212, pp. 344–352. DOI: 10.1016/j.snb.2015.02.008.

Parshintsev, J. and T. Hyötyläinen (2015). "Methods for characterization of organic compounds in atmospheric aerosol particles". In: *Analytical and Bioanalytical Chemistry* 407.20, pp. 5877–5897. DOI: 10.1007/s00216-014-8394-3.

Pérez, N. et al. (June 2010). "Variability of Particle Number, Black Carbon, and PM10, PM2.5, and PM1Levels and Speciation: Influence of Road Traffic Emissions on Urban Air Quality". In: *Aerosol Science and Technology* 44.7, pp. 487–499. DOI: 10.1080/02786821003758286.

Bibliography

Peters, M. H., D. W. Cooper, and R. J. Miller (Jan. 1989). "The effects of electrostatic and inertial forces on the diffusive deposition of small particles onto large disks: Viscous axisymmetric stagnation point flow approximations". In: *Journal of Aerosol Science* 20.1, pp. 123–136. DOI: 10.1016/0021-8502(89)90036-0.

Podlinski, J. et al. (May 2008). "ESP performance for various dust densities". In: *Journal of Electrostatics* 66.5-6, pp. 246–253. DOI: 10.1016/j.elstat.2008.01.003.

Polidori, A. et al. (2008). "Organic pm2.5: Fractionation by polarity, ftir spectroscopy, and om/oc ratio for the pittsburgh aerosol". In: *Aerosol Science and Technology* 42.3, pp. 233–246. DOI: 10.1080/02786820801958767.

Poole, R. J. (June 2010). "Development-Length Requirements for Fully Developed Laminar Flow in Concentric Annuli". In: *Journal of Fluids Engineering* 132.6. DOI: 10.1115/1.4001694.

Preger, C. et al. (Jan. 2020). "Predicting the deposition spot radius and the nanoparticle concentration distribution in an electrostatic precipitator". In: *Aerosol Science and Technology*, pp. 1–11. DOI: 10.1080/02786826.2020.1716939.

Qi, C., D. R. Chen, and D. Y. H. Pui (2007). "Experimental study of a new corona-based unipolar aerosol charger". In: *Journal of Aerosol Science* 38.7, pp. 775–792. DOI: 10.1016/j.jaerosci.2007.05.005.

Quinten, M. (2011). *Optical Properties of Nanoparticle Systems: Mie and Beyond*. Weinheim: Wiley-VCH Verlag & Co. KGaA.

Rader, D. J. and V. a. Marple (1985). "Effect of Ultra-Stokesian Drag and Particle Interception on Impaction Characteristics". In: *Aerosol Science and Technology* 4.2, pp. 141–156. DOI: 10.1080/02786828508959044.

Ranney, A. P. and P. J. Ziemann (2016). "Microscale spectrophotometric methods for quantification of functional groups in oxidized organic aerosol". In: *Aerosol Science and Technology* 50.9, pp. 881–892. DOI: 10.1080/02786826.2016.1201197.

Rees, J. a. (1973). "Chapter 5 Electrical breakdown in gases". In: *High Voltage Engineering : Fundamentals* V, p. 294. DOI: 10.1016/B978-0-7506-3634-6.50006-X.

Reynolds, J. P, L. Theodore, and J. Marino (June 1975). "Calculating Collection Efficiencies for Electrostatic Precipitators". In: *Journal of the Air Pollution Control Association* 25.6, pp. 610–616. DOI: 10.1080/00022470.1975.10470116.

Riha, S. C. et al. (Feb. 2013). "Atomic Layer Deposition of a Submonolayer Catalyst for the Enhanced Photoelectrochemical Performance of Water Oxidation with Hematite". In: *ACS Nano* 7.3, pp. 2396–2405. DOI: 10.1021/nn305639z.

Rooi, J. J. de and P. H. Eilers (Aug. 2012). "Mixture models for baseline estimation". In: *Chemometrics and Intelligent Laboratory Systems* 117, pp. 56–60. DOI: 10.1016/j.chemolab.2011.11.001.

Russell, L. M. (July 2003). "Aerosol Organic-Mass-to-Organic-Carbon Ratio Measurements". In: *Environmental Science & Technology* 37.13, pp. 2982–2987. DOI: 10.1021/es026123w.

Russell, L. M., R. Bahadur, and P. J. Ziemann (Feb. 2011). "Identifying organic aerosol sources by comparing functional group composition in chamber and atmospheric particles". In: *Proceedings of the National Academy of Sciences* 108.9, pp. 3516–3521. DOI: 10.1073/pnas.1006461108.

Schmid, H.-J. (Oct. 2003). "On the modelling of the particle dynamics in electro-hydrodynamic flow fields". In: *Powder Technology* 135-136, pp. 136–149. DOI: 10.1016/j.powtec.2003.08.010.

Segal-Rosenheimer, M., Y. Dubowski, and R. Linker (Apr. 2009). "Extraction of optical constants from mid-IR spectra of small aerosol particles". In: *Journal of Quantitative Spectroscopy and Radiative Transfer* 110.6-7, pp. 415–426. DOI: 10.1016/j.jqsrt.2009.01.005.

Shaka', H. and N. A. Saliba (2004). "Concentration measurements and chemical composition of PM10-2.5 and PM2.5 at a coastal site in Beirut, Lebanon". In: *Atmospheric Environment* 38.4, pp. 523–531. DOI: 10.1016/j.atmosenv.2003.10.009.

Shimada, M. et al. (1999). "Removal of Airborne Particles By a Device Using Uv / Photoelectron Method Under Reduced Pressure Conditions". In: 30.3, pp. 341–353.

Sioutas, C. (Jan. 1999). "Experimental Investigation of Pressure Drop with Particle Loading in Nuclepore Filters". In: *Aerosol Science and Technology* 30.1, pp. 71–83. DOI: 10.1080/027868299304895.

Sisler, J. F. and W. C. Malm (Mar. 1994). "The relative importance of soluble aerosols to spatial and seasonal trends of impaired visibility in the United States". In: *Atmospheric Environment* 28.5, pp. 851–862. DOI: 10.1016/1352-2310(94)90244-5.

Somani, P. R., S. P. Somani, and M. Umeno (Oct. 2006). "Planer nano-graphenes from camphor by CVD". In: *Chemical Physics Letters* 430.1-3, pp. 56–59. DOI: 10.1016/j.cplett.2006.06.081.

Soo, J.-C. et al. (Dec. 2015). "Air sampling filtration media: Collection efficiency for respirable size-selective sampling". In: *Aerosol Science and Technology* 50.1, pp. 76–87. DOI: 10.1080/02786826.2015.1128525.

Stafford, R. G. and H. J. Ettinger (May 1972). "Filter efficiency as a function of particle size and velocity". In: *Atmospheric Environment (1967)* 6.5, pp. 353–362. DOI: 10.1016/0004-6981(72)90201-6.

Su, Y. et al. (Feb. 2004). "Development and Characterization of an Aerosol Time-of-Flight Mass Spectrometer with Increased Detection Efficiency". In: *Analytical Chemistry* 76.3, pp. 712–719. DOI: 10.1021/ac034797z.

Sukhorukov, G. B. et al. (June 1998). "Layer-by-layer self assembly of polyelectrolytes on colloidal particles". In: *Colloids and Surfaces A: Physicochemical and Engineering Aspects* 137.1-3, pp. 253–266. DOI: 10.1016/s0927-7757(98)00213-1.

Takahama, S., R. E. Schwartz, et al. (2011). "Organic functional groups in aerosol particles from burning and non-burning forest emissions at a high-elevation mountain site". In: *Atmospheric Chemistry and Physics* 11.13, pp. 6367–6386. DOI: 10.5194/acp-11-6367-2011.

Takahama, S. and A. M. Dillner (2015). "Model selection for partial least squares calibration and implications for analysis of atmospheric organic aerosol samples with mid-infrared spectroscopy". In: *Journal of Chemometrics* 29.12, pp. 659–668. DOI: 10.1002/cem.2761.

Takahama, S., A. Johnson, and L. M. Russell (2013). "Quantification of Carboxylic and Carbonyl Functional Groups in Organic Aerosol Infrared Absorbance Spectra". In: *Aerosol Science and Technology* 47.3, pp. 310–325. DOI: 10.1080/02786826.2012.752065.

Takahama, S., G. Ruggeri, and A. M. Dillner (2016). "Analysis of functional groups in atmospheric aerosols by infrared spectroscopy: Sparse methods for statistical selection of

relevant absorption bands". In: *Atmospheric Measurement Techniques* 9.7, pp. 3429–3454. DOI: 10.5194/amt-9-3429-2016.

Toon, O. B. et al. (Nov. 1976). "The optical constants of several atmospheric aerosol species: Ammonium sulfate, aluminum oxide, and sodium chloride". In: *Journal of Geophysical Research* 81.33, pp. 5733–5748. DOI: 10.1029/jc081i033p05733.

Torrie, B. et al. (Jan. 1972). "Raman and infrared studies of the ferroelectric transition in ammonium sulphate". In: *Journal of Physics and Chemistry of Solids* 33.3, pp. 697–709. DOI: 10.1016/0022-3697(72)90078-9.

Tsai, C.-j. et al. (2010). "Enhancement of Extrinsic Charging Efficiency of a Nanoparticle Charger with Multiple Discharging Wires Enhancement of Extrinsic Charging Efficiency of a Nanoparticle Charger with Multiple Discharging Wires". In: 6826. DOI: 10.1080/02786826. 2010.492533.

Turner, J. R., D. K. Liguras, and H. Fissan (Jan. 1989). "Clean room applications of particle deposition from stagnation flow: electrostatic effects". In: *Journal of Aerosol Science* 20.4, pp. 403–417. DOI: 10.1016/0021-8502(89)90074-8.

Vanderpool, R. W. et al. (Jan. 2001). "Evaluation of the Loading Characteristics of the EPA WINS PM2.5Separator". In: *Aerosol Science and Technology* 34.5, pp. 444–456. DOI: 10.1080/02786820117739.

Vecchi, R. et al. (Mar. 2009). "Organic and inorganic sampling artefacts assessment". In: *Atmospheric Environment* 43.10, pp. 1713–1720. DOI: 10.1016/j.atmosenv.2008.12.016.

Veltkamp, P. R. et al. (June 1996). "Chromatographic measurement of molecular markers of sources of atmospheric aerosol particles". In: *Environmental Geochemistry and Health* 18.2, pp. 77–80. DOI: 10.1007/bf01771135.

Volckens, J. and D. Leith (Nov. 2002). "Electrostatic Sampler for Semivolatile Aerosols: Chemical Artifacts". In: *Environmental Science & Technology* 36.21, pp. 4608–4612. DOI: 10.1021/es0207100.

W.J.O.-T. (Mar. 1969). "N.J. Harrick, internal reflection spectroscopy". In: *Journal of Molecular Structure* 3.3, p. 261. DOI: 10.1016/0022-2860(69)87014-6.

Weber, R. J. et al. (Jan. 2001). "A Particle-into-Liquid Collector for Rapid Measurement of Aerosol Bulk Chemical Composition". In: *Aerosol Science and Technology* 35.3, pp. 718–727. DOI: 10.1080/02786820152546761.

Weis, D. D. and G. E. Ewing (Aug. 1996). "Infrared spectroscopic signatures of (NH4)2SO4aerosols". In: *Journal of Geophysical Research: Atmospheres* 101.D13, pp. 18709–18720. DOI: 10.1029/96jd01543.

Weisbach, J. (1845). *Lehrbuch der Ingenieur- und Maschinenmechanik*. Vieweg und Sohn, Braunschweig.

Whitby, K. T. (1961). "Generator for Producing High Concentrations of Small Ions". In: *Review of Scientific Instruments* 32.12, pp. 1351–1355. DOI: 10.1063/1.1717250.

Winslow, C.-E. A. (July 1908). "A NEW METHOD OF ENUMERATING BACTERIA IN AIR". In: *Science* 28.705, pp. 28–31. DOI: 10.1126/science.28.705.28.

Yaffe, L. (1943). "Studies on aerosol filtration." In.

Yamamoto, N. et al. (June 2004). "Time course shift in particle penetration characteristics through capillary pore membrane filters". In: *Journal of Aerosol Science* 35.6, pp. 731–741. DOI: 10.1016/j.jaerosci.2003.12.001.

Zheng, L. et al. (Feb. 2017). "Characterization of an aerosol microconcentrator for analysis using microscale optical spectroscopies". In: *Journal of Aerosol Science* 104, pp. 66–78. DOI: 10.1016/j.jaerosci.2016.11.007.

Zheng, Y. and M. Yao (Apr. 2017). "Liquid impinger BioSampler's performance for size-resolved viable bioaerosol particles". In: *Journal of Aerosol Science* 106, pp. 34–42. DOI: 10.1016/j.jaerosci.2017.01.003.

Zhibin, Z. and Z. Guoquan (Jan. 1994). "Investigations of the Collection Efficiency of an Electrostatic Precipitator with Turbulent Effects". In: *Aerosol Science and Technology* 20.2, pp. 169–176. DOI: 10.1080/02786829408959674.

Zypman, F. R. (Apr. 2006). "Off-axis electric field of a ring of charge". In: *American Journal of Physics* 74.4, pp. 295–300. DOI: 10.1119/1.2149869.

Nikunj Dudani

nikunj.dudani@epfl.ch

65 Avenue de Cour	**Date of Birth:** 31st May 1991
1007 Lausanne, Vaud, Switzerland	**Mobile :** +41 765222588

EDUCATION

Ph. D. (Chemistry and Chemical Engineering), Laboratory of Atmospheric Processes   June 2017 onwards
and their Impacts, École polytechnique fédérale de Lausanne (EPFL), Switzerland

- Advisor: Dr. Satoshi Takahama
- Design and fabrication of an aerosol sampling device for spectroscopy analysis

Bachelor of Engineering (Hons.) in Chemical and in Mechanical (5 Year Dual Degree)   2009 - 2014
Birla Institute of Technology and Science, Pilani, India

- Cumulative Grade Point Average, C.G.P.A. - 9.80 on a scale of 10
- Among top 4 students in a batch of around 600

Higher Secondary, St. Xavier's Collegiate School, Kolkata, India   2009

EXPERIENCE

Head of formation/ branding strategy at **bonvoyageu.com, Kolkata, India**   July 2015 – June 2017

- Product planning, managing and operating a tour & travel brand, bonvoyageu.com, focused towards inbound tourism to Europe
- Partnership formation with hotel chains (Accor S.A., Marriot international Inc.), travel coach providers (Buchard Voyages S.A.) and activity providers (Tour Eiffel, Rail Europe, among others).

Head of Product development at **Sreeji Petro Products, Kolkata, India**   May 2014 – June 2016

- Research & develop a special "Calcium Grease" with high thermal stability and subsequently designing and scaling up the process from lab to pilot to industrial scale
- Brand development and marketing for the new grease

Industrial Thesis at **Deccan Fine Chemicals Pvt. Ltd., Hyderabad, India**   January 2014 – May 2014

- Development of Agro-chemicals and manufacturing techniques
- Worked on collaborative projects with Bayer, Syngenta and Du-Pont

Research Thesis at **Max Planck Institute for Biophysical Chemistry**   May 2013 – December 2013
Göttingen, Germany

- Microfluidic Research Lab, led by Dr. Thomas Burg. Worked with Dr. Yara Mejia
- Designing a Cryogenic stage for "Microfluidic cryofixation for correlative microscopy", a multidisciplinary project incorporating various Engineering aspects

Research Internship at **Max Planck Institute for Biophysical Chemistry**   May 2013 – July2013
Göttingen, Germany

- Worked with Dr. Thomas Burg and Dr. Rachel Lowe
- Design and fabrication of a micro-system for real-time transport characterization of biomolecules

Summer Internship at **Development Consultants Private Limited (DCPL)**   May 2011 – July 2011
Kolkata, West Bengal, India

- Design and hydraulic calculations of a raw water treatment plant and a demineralization plant

Additive Manufacturing (AM) of Micro Electronic Mechanical Systems   August 2012 – December 2012
(MEMS) Components
- With Dr. S.P. Regalla, Department of Mechanical Engineering, BITS-Pilani, Hyderabad Campus

Hybrid Polymer Composite and their Mechanical Properties Testing   August 2012 – December 2012
- With Dr. D. Purnima, Department of Chemical Engineering, BITS– Pilani, Hyderabad Campus
- Extensive literature study of hybrid composites & mechanically testing PET/Talc/EPDM sample

---

AWARDS AND ACHEIVEMENT

"Merit Scholarship for Excellence" in academics   January 2010 – July 2014
- For 9 consecutive semesters from 2nd semester onwards which is awarded to 10 best academic performers from each batch of students of around 600 students

DAAD-WISE scholarship for research internship in Germany   March 2012 – July 2012
- Awarded to selected few (200-250) from India, by "Deutscher Akademischer Austausch Dienst"

1st Prize for technical paper presentation competition on Institute level   September 2012
- Title "Appropriate Climate Responsive Technology for Inclusive Growth and Sustainable Development", organised by Department of Mechanical Engineering, BITS-Pilani, Hyderabad, India

Founder, 'International Programs and Collaboration Division (IPCD) Student Nucleus'   2012-13
- Working with Prof. Suman Kapur, Dean, IPCD, BITS-Pilani University towards formulating new University MOUs and encouraging students' international participation

---

PUBLICATIONS

Dudani, N., Takahama, S., (2020). ELECTROSTATIC PARTICLE COLLECTOR. **European patent** EP20213247.8. *Submitted

Yazdani, A., Dudani, N., Takahama, S., Bertrand, A., Prévôt, A., El Haddad, I., & Dillner, A. (2020). Characterization of primary and aged wood burning and coal combustion organic aerosols in environmental chamber and its implications for atmospheric aerosols. **Atmospheric Chemistry and Physics** Discussions, (September), 1–32. https://doi.org/10.5194/acp-2020-924

Arangio, A., Delval, C., Ruggeri, G., Dudani, N., Yazdani, A., & Takahama, S. (2019). Electrospray Film Deposition for Solvent-Elimination Infrared Spectroscopy, **Applied spectroscopy**, 73(6), 638–652. https://doi.org/10.1177/0003702818821330

Faoro, R., Bassu, M., Mejia, Y. X., Stephan, T., Dudani, N., Boeker, C., ... Burg, T. P. (2018). Aberration-corrected cryoimmersion light microscopy. **Proceedings of the National Academy of Sciences** of the United States of America, 115(6), 1204–1209. https://doi.org/10.1073/pnas.1717282115

Conferences:

Dudani N., Takahama S., Design and Fabrication of an Aerosol Sampling Device Prototype for Spectroscopy Analysis, **European Aerosol Conference** (2019). Gothenburg, Sweden. (poster P1-085)

Dudani N., Mejia Y., Burg T. P., Design, Implementation and Evaluation of a Cryogenic Stage for Combined Cryofixation and Optical Microscopy of Biological Samples, **Innovations in Chemical Engineering**. (2013). Hyderabad, India, Vol. 1, pp. 193-196. (ISBN No: 978-81-7800-329-0)

SKILLS

Languages	English (Fluent), French (A2), German (A2), Hindi (Fluent), Marwari (Fluent)
Design Tools	AutoCAD, Autodesk Inventor, Pro Engineer, Solid Works, COMSOL Multiphysics
Programming Tools	Python, MATLAB, LabView, C, C++ and Java
Laboratory	3D-printing, Scanning Electron Microscopy, Transmission Electron Microscopy, X-ray diffraction, Photolithography, Material machining and manufacturing.